LATTICE BOLTZMANN SIMULATIONS OF SOFT MATTER SYSTEMS

Burkhard Dünweg[1] and Anthony J. C. Ladd[2]

[1] Max Planck Institute for Polymer Research
Ackermannweg 10, 55128 Mainz, Germany
duenweg@mpip-mainz.mpg.de

[2] Chemical Engineering Department
University of Florida, Gainesville, FL 32611-6005, USA
tladd@che.ufl.edu

This article concerns numerical simulations of the dynamics of particles immersed in a continuum solvent. As prototypical systems, we consider colloidal dispersions of spherical particles and solutions of uncharged polymers. After a brief explanation of the concept of hydrodynamic interactions, we give a general overview of the various simulation methods that have been developed to cope with the resulting computational problems. We then focus on the approach we have developed, which couples a system of particles to a lattice-Boltzmann model representing the solvent degrees of freedom. The standard D3Q19 lattice-Boltzmann model is derived and explained in depth, followed by a detailed discussion of complementary methods for the coupling of solvent and solute. Colloidal dispersions are best described in terms of extended particles with appropriate boundary conditions at the surfaces, while particles with internal degrees of freedom are easier to simulate as an arrangement of mass points with frictional coupling to the solvent. In both cases, particular care has been taken to simulate thermal fluctuations in a consistent way. The usefulness of this methodology is illustrated by studies from our own research, where the dynamics of colloidal and polymeric systems has been investigated in both equilibrium and nonequilibrium situations.

1
Introduction

The term "soft condensed matter" generally refers to materials which possess additional "mesoscopic" length scales between the atomic and the macroscopic scales [1–8]. While simple fluids are characterized by the atomic size ($3 \times 10^{-10}m$), soft–matter systems contain one or more additional length scales, typically of order $10^{-9}m - 10^{-6}m$. There are many examples of matter with mesoscale structure, including suspensions, gels, foams, and emulsions; all of these are characterized by viscoelastic behavior, which means a response that is fluid–like on long time scales but solid–like on shorter time scales. The two prototype systems considered in this article are colloidal dispersions of hard particles, where the additional length scale is provided by the particle size, and polymer systems, where the length scale is the size of the macromolecule. The main difference between these two systems is the presence of internal degrees of freedom in the polymer, such that a statistical description is necessary even on the single–molecule level. Many additional soft–matter systems exist. For example, dispersions may not only contain spherical particles, but

rather rod–like or disk–like objects. For polymers, there are many possible molecular architectures; in addition to simple linear chains, there are rings, stars, combs, bottle–brush polymers and dendrimers. Polymers may also self–assemble into two–dimensional membranes, either free or tethered, which are of paramount biological importance in cell membranes, vesicles, and red blood cells.

Strongly non-linear rheology is characteristic of soft matter. In simple fluids, it is difficult to observe any deviations from Newtonian behavior, which is well described by the hydrodynamic equations of motion with linear transport coefficients that depend only on the thermodynamic state. Indeed, Molecular Dynamics simulations [9] have revealed that a hydrodynamic description is valid down to astonishingly small scales, of the order of a few collisions of an individual molecule. This means that one would have to probe the system with very short wave lengths and very high frequencies, which are typically not accessible to standard experiments (with the exception of neutron scattering [10]), and even less in everyday life. However, in soft–matter systems microstructural components (particles and polymers for example) induce responses that depend very much on frequency and length scale. These systems are often referred to as "complex fluids".

The nonlinear rheological properties of soft matter pose a substantial challenge for theory [11]. Therefore, the study of simple model systems is often the only way to make systematic progress. Numerical simulations allow us to follow the dynamics of model systems without invoking the uncontrolled approximations that are usually required by purely analytical methods. Simulations can be used to isolate and investigate the influence of microstructure, composition, external perturbation and geometry in ways that cannot always be duplicated in the laboratory. In particular, simulations can provide a well–defined test bed for theoretical ideas, allowing them to be evaluated in a simpler and more rigorous environment than is possible experimentally. Finally they can provide more detailed and direct information on the particle dynamics and structure than is typically possible with experimental measurements.

In this article we will focus on systems which comprise particles, with or without internal degrees of freedom, suspended in a simple fluid. We will first outline the necessary ingredients for a theoretical description of the dynamics, and in particular explain the concept of hydrodynamic interactions (HI). Starting from this background, we will provide a brief overview of the various simulation approaches that have been developed to treat such systems. All of these methods are based upon a description of the solute in terms of particles, while the solvent is taken into account by a simple (but sufficient) model, making use of the fact that it can be described as a Newtonian fluid. Such methods are often referred to as "mesoscopic". We will then describe and derive in some detail the algorithms that have been developed by us to couple a particulate system to a lattice–Boltzmann fluid. The usefulness of these methods will then be demonstrated by applications to colloidal dispersions and polymer solutions. Some of the material presented here is a summary of previously published work.

2
Particle-fluid systems

2.1
Coarse–grained models

The first step towards understanding systems of particles suspended in a solvent is the notion of *scale separation*. Colloidal particles are much larger (up to $10^{-6}m$) than solvent molecules, and their relaxation time (up to $10s$), given by the time the particle needs to diffuse its own size, is several orders of magnitude larger than the corresponding solvent time scale ($10^{-12}s$) as well. A similar separation of scales holds for solute with internal degrees of freedom, like polymer chains, membranes, or vesicles, as far as their diffusive motion or their global conformational reorganization is concerned. However, these systems contain a hierarchy of length and time scales, which can be viewed as a spectrum of internal modes with a given wavelength and relaxation time. For the long–wavelength part of this spectrum, the same scale separation holds, but when the wavelength is comparable with the solvent size molecular interactions become important. However, on scales of interest, these details can usually be lumped into a few parameters. The solute is then modeled as a system of "beads" interacting with each other via an effective potential. The beads should be viewed as collections of atomic–scale constituents, either individual atoms or functional groups, which have been combined into a single effective unit in a process known as "coarse–graining". On the scale of the beads, the solvent may be viewed as a hydrodynamic continuum, characterized by its shear viscosity and temperature. The flow of soft matter is usually isothermal, incompressible, and inertia–free (zero Reynolds number). Then, the most natural parameter to describe solute–solvent coupling in polymeric systems is the Stokes friction coefficient of the individual beads, or (in the case of anisotropic subunits) the corresponding tensorial generalization. The effective friction coefficient is the lumped result of a more detailed, or "fine–grained", description at the molecular scale, as is the bead–bead potential, which should be viewed as a potential of mean force. In order to make contact with experimental systems, these parameters must be calculated from more microscopic theories or simulations, or deduced from experimental data.

Further simplification may arise from the type of scientific question being addressed by the coarse–grained model. If the interest is not in specific material properties of a given chemical species, but rather in generic behavior and mechanisms, as is the case for the examples we will discuss in this article, then the details of the parameterization are less important than a model that is both conceptually simple and computationally efficient. The standard model for particulate suspensions is a system of hard spheres, while for polymer chains the Kremer–Grest model [12] has proved to be a valuable and versatile tool. Here, the beads interact via a purely repulsive Lennard–Jones (or WCA [13]) potential,

$$V_{LJ}(r) = \begin{cases} 4\varepsilon \left[\left(\frac{\sigma}{r}\right)^{12} - \left(\frac{\sigma}{r}\right)^{6} + \frac{1}{4} \right] & r \leq 2^{1/6}\sigma, \\ 0 & r \geq 2^{1/6}\sigma, \end{cases} \tag{1}$$

while consecutive beads along the chain are connected via a FENE ("finitely extensible nonlinear elastic") potential,

$$V_{ch}(r) = -\frac{k}{2}R_0^2 \ln\left(1 - \frac{r^2}{R_0^2}\right),\tag{2}$$

with typical parameters $R_0/\sigma = 1.5$, $k\sigma^2/\varepsilon = 30$. Chain stiffness can be incorporated by an additional bond–bending potential, while more complicated architectures (like stars and tethered membranes) require additional connectivity. Poor solvent quality is modeled by adding an attractive part to the non–bonded interaction, while Coulomb interactions (however without local solvent polarization) can be included by using charged beads.

There are two further ingredients which any good soft–matter model should take into account: On the one hand, *thermal fluctuations* are needed in order to drive Brownian motion and internal reorganization of the conformational degrees of freedom. There are however special situations where thermal noise can be disregarded, and ideally the simulation method should be flexible enough to be able to turn the noise both on and off. On the other hand, *hydrodynamic interactions*, which will be the subject of the next subsection, need to be taken into account in most circumstances.

2.2
Hydrodynamic interactions

The term "hydrodynamic interactions" describes the *dynamic* correlations between the particles, induced by diffusive momentum transport through the solvent. The physical picture is the same, whether the particle motion is Brownian (*i.e.* driven by thermal noise) or the result of an external force (*e.g.* sedimentation or electrophoresis). The motion of particle i perturbs the surrounding solvent, and generates a flow. This signal spreads out diffusively, at a rate governed by the kinematic viscosity of the fluid $\eta_{kin} = \eta/\rho$ (η is the solvent shear viscosity and ρ is its mass density). On interesting (long) time scales, only the transverse hydrodynamic modes [14] remain, and the fluid may be considered as incompressible. The viscous momentum field around a particle diffuses much faster than the particle itself, so that the Schmidt number

$$Sc = \frac{\eta_{kin}}{D}\tag{3}$$

is large. In a molecular fluid, D is the diffusion coefficient of the solvent molecules and $Sc \sim 10^2 - 10^3$, while for soft matter, where D is the diffusion coefficient of the polymer or colloid, Sc is much larger, up to 10^6 for micron size colloids. The condition $Sc \gg 1$ is an important restriction on the dynamics, which good mesoscopic models should satisfy. Consider two beads i and j, separated by a distance r_{ij}. The momentum generated by the motion of i with respect to the surrounding fluid reaches bead j after a "retardation time" $\tau \sim r_{ij}^2/\eta_{kin}$. After this time the motion of j becomes *correlated* with that of bead i. However, during the retardation time the beads

have traveled a small distance $\sim \sqrt{D\tau} \sim r_{ij}/\sqrt{Sc}$, which is negligible in comparison with r_{ij}. Therefore, it is quite reasonable to describe the Brownian motion of the beads neglecting retardation effects, and consider their random displacements to be *instantaneously* correlated.

These general considerations suggest a Langevin description (stochastic differential equation) for the the time evolution of the bead positions $\mathbf{r}_i$:

$$\frac{d}{dt}r_{i\alpha} = \sum_j \mu_{i\alpha,j\beta}F_{j\beta}^c + \Delta_{i\alpha}, \tag{4}$$

where α, β are Cartesian indexes and the Einstein summation convention has been assumed. $\mathbf{F}_j^c$ is the conservative force acting on the jth bead, while the mobility tensor μ_{ij} describes the velocity response of particle i to $\mathbf{F}_j^c$; both $\mathbf{F}_j^c$ and μ_{ij} depend on the configuration of the N particles, $\mathbf{r}^N$. The random displacements (per unit time) $\Delta_{i\alpha}$ are Gaussian white noise variables [15, 16] satisfying the fluctuation–dissipation relation

$$\langle \Delta_{i\alpha} \rangle = 0, \tag{5}$$
$$\langle \Delta_{i\alpha}(t)\Delta_{j\beta}(t') \rangle = 2k_BT\mu_{i\alpha,j\beta}\delta(t-t'); \tag{6}$$

here T is the temperature and k_B denotes the Boltzmann constant. In general, the mobility tensor, $\mu_{i\alpha,j\beta}$ depends on particle position, in which case the stochastic integral should be evaluated according to the Stratonovich calculus. This is because during a finite time step a particle samples different mobilities as its position changes. Numerically simpler is the Ito calculus [15, 16], which uses the mobility at the beginning of the time step. In this case an additional term needs to be added to Eq. 4,

$$\frac{d}{dt}r_{i\alpha} = \sum_j \mu_{i\alpha,j\beta}F_{j\beta}^c + k_BT\sum_j \frac{\partial \mu_{i\alpha,j\beta}}{\partial r_{j\beta}} + \Delta_{i\alpha}. \tag{7}$$

In cases where the divergence of the mobility vanishes, $\partial\mu_{i\alpha,j\beta}/\partial r_{j\beta} = 0$, the Ito and Stratonovich interpretations coincide.

Processes generated by Eq. 4 (Stratonovich) or Eq. 7 (Ito) sample trajectories from a probability distribution in the configuration space of the beads, $P\left(\mathbf{r}^N, t\right)$, which evolves according to a Fokker-Planck equation (Kirkwood diffusion equation):

$$\frac{\partial}{\partial t}P\left(\mathbf{r}^N, t\right) = \mathcal{L}P\left(\mathbf{r}^N, t\right), \tag{8}$$

with the Fokker–Planck operator

$$\mathcal{L} = \sum_{ij} \frac{\partial}{\partial r_{i\alpha}}\mu_{i\alpha,j\beta}\left(k_BT\frac{\partial}{\partial r_{j\beta}} - F_{j\beta}^c\right). \tag{9}$$

Writing the forces as the derivative of a potential,

$$F_{i\alpha}^c = -\frac{\partial}{\partial r_{i\alpha}}V\left(\mathbf{r}^N\right), \tag{10}$$

it follows that the Boltzmann distribution, $P \propto \exp\left(-V/k_B T\right)$, is the stationary solution of the Kirkwood diffusion equation; in other words the model satisfies the fluctuation-dissipation relation.

The mobility tensor can be derived from Stokes–flow hydrodynamics. Consider a set of spherical particles, located at positions $\mathbf{r}_i$ with radius a, surrounded by a fluid with shear viscosity η. Each of the particles has a velocity $\mathbf{v}_i$, which, as a result of stick boundary conditions, is identical to the local fluid velocity on the particle surface. The resulting fluid motions generate hydrodynamic drag forces $\mathbf{F}_i^d$, which at steady state are balanced by the conservative forces, $\mathbf{F}_i^d + \mathbf{F}_i^c = 0$. The commonly used approximation scheme is a systematic multipole expansion, similar to the analogous expansion in electrostatics [17–21]. For details, we refer the reader to the original literature [17], where the contributions from rotational motion of the beads are also considered. As a result of the linearity of Stokes flow, the particle velocities and drag forces are linearly related,

$$v_{i\alpha} = -\sum_j \mu_{i\alpha,j\beta} F_{j\beta}^d = \sum_j \mu_{i\alpha,j\beta} F_{j\beta}^c. \tag{11}$$

Since μ_{ij} describes the velocity response of particle i to the force acting on particle j, it must be identical to the mobility tensor appearing in the Langevin equation.

In general the mobility matrix is a function of all the particle coordinates, but to leading order, it is pairwise additive:

$$\mu_{ij} = \frac{\delta_{ij} 1}{6\pi\eta a} + \frac{(1-\delta_{ij})}{8\pi\eta r_{ij}} \left(1 + \frac{\mathbf{r}_{ij}\mathbf{r}_{ij}}{r_{ij}^2}\right) + \frac{(1-\delta_{ij})\,a^2}{12\pi\eta r_{ij}^3} \left(1 - 3\frac{\mathbf{r}_{ij}\mathbf{r}_{ij}}{r_{ij}^2}\right), \quad (12)$$

where $\mathbf{r}_{ij} = \mathbf{r}_i - \mathbf{r}_j$, and 1 denotes the unit tensor. The hydrodynamic interaction is long–ranged and therefore has a strong influence on the collective dynamics of suspensions and polymer solutions. This approximate form for the mobility matrix follows from the assumption that the force density on the sphere surface is constant. A point multipole expansion, by contrast, generates the Oseen ($1/r_{ij}$) interaction at lowest order [22], and can lead to non-positive-definite mobility matrices [23]. Thus the simplest practical form for the hydrodynamic interaction is the Rotne-Prager tensor [23] given in Eq. 12. Both the Oseen and Rotne-Prager mobilities are divergence free, and therefore there is no distinction between Ito and Stratonovich interpretations. However, at higher orders in the multipole expansion, the divergence is nonzero [24].

2.3
Computer simulation methods and models

In this section we briefly summarize the Brownian dynamics algorithm and its close cousin Stokesian Dynamics. We then outline the motivation and development of several mesoscale methods, some of which are reviewed elsewhere in this series.

2.3.1
Brownian Dynamics

Brownian dynamics is conceptually the most straightforward approach [25, 26]. Starting from the Langevin equation for the particle coordinates, Eq. 4, and discretizing the time into finite length steps h, gives a first-order (Euler) update for the particle positions,

$$r_{i\alpha}(t + h) = r_{i\alpha}(t) + \sum_j \mu_{i\alpha,j\beta} F_{j\beta}^c h + \sqrt{2k_B T h} \sum_j \sigma_{i\alpha,j\beta} q_{j\beta}. \tag{13}$$

Here $q_{i\alpha}$ are random variables with

$$\langle q_{i\alpha} \rangle = 0 \tag{14}$$

$$\langle q_{i\alpha} q_{j\beta} \rangle = \delta_{ij}\delta_{\alpha\beta}, \tag{15}$$

while the matrix $\sigma_{i\alpha,j\beta}$ satisfies the relation

$$\sum_k \sigma_{i\alpha,k\gamma}\sigma_{j\beta,k\gamma} = \mu_{i\alpha,j\beta}. \tag{16}$$

Note that in Eq. 13 we have assumed a divergence–free mobility tensor

Although the number of degrees of freedom has been minimized, this approach is computationally intensive, and imposes severe limitations on the size of the system that can be studied. Since every particle interacts with every other particle, the calculation of the mobility matrix scales as $O(N^2)$, where N is the number of Brownian particles. In addition, the covariance matrix for the random displacements requires a Cholesky decomposition of the mobility matrix, which scales as $O(N^3)$ [27]. The computational costs of Brownian dynamics are so large that even today one cannot treat more than a few hundred Brownian particles [28].

"Stokesian Dynamics" [29] is an improved version of Brownian dynamics, in which the mobility tensor takes into account short–range (lubrication) contributions to the hydrodynamic forces. It also improves the far-field interactions by including contributions from torques and stresslets, although still higher moments are needed for accurate results in concentrated suspensions [19]. Stokesian Dynamics is even more computationally intensive than Brownian dynamics; the determination of the mobility tensor is already an $O(N^3)$ process.

However, there have been two important improvements in efficiency. First, Fixman [25, 26, 30, 31] has proposed an approximation to $\sigma_{i\alpha,j\beta}$ by a truncated expansion in Chebyshev polynomials, which has a more favorable scaling than Cholesky decomposition. Second, the long-range hydrodynamic interactions can be calculated by Fast Fourier Transforms [32–37], or hierarchical multipole expansions [20]. Accelerated Brownian Dynamics and Stokesian Dynamics algorithms scale close to linearly in the number of particles, and their full potential is not yet explored. However, it should be noted that all these methods are based upon an efficient evaluation of the Green's function for the Stokes flow, which depends on the global boundary conditions. For planar boundaries, solutions are available [21, 38–40], but a more general shape requires a numerical calculation of the Green's function between a tabulated set of source and receiver positions [41].

2.3.2
Mesoscale methods

In view of the computational difficulties associated with Brownian Dynamics, several "mesoscale" methods have been developed recently. The central idea is to *keep* the solvent degrees of freedom, but to describe them in a simplified fashion, such that only the most salient features survive. As we have already seen, it is in principle sufficient to describe the solvent as a Navier–Stokes continuum, *or* by some suitable model which behaves like a Navier–Stokes continuum on sufficiently large length and time scales. At least asymptotically, the solvent dynamics must be described by the equations

$$\partial_t \rho + \partial_\alpha \left(\rho u_\alpha \right) = 0,$$
$$\partial_t \left(\rho u_\alpha \right) + \partial_\beta \left(\rho u_\alpha u_\beta \right) + \partial_\alpha p = \partial_\beta \sigma_{\alpha\beta} + \partial_\beta \sigma^f_{\alpha\beta} + f_\alpha, \tag{17}$$

where ρ is the mass density, $\rho\mathbf{u}$ the momentum density, p the thermodynamic pressure, $\mathbf{f}$ an external force density applied to the fluid, σ the viscous stress tensor, and σ^f the fluctuating (Langevin) stress [42], whose statistical properties will be discussed in later chapters of this article. The viscous stresses are characterized by the shear and bulk viscosities, η and η_v, which we will assume to be constants, independent of thermodynamic state and flow conditions:

$$\sigma_{\alpha\beta} = \eta \left(\partial_\alpha u_\beta + \partial_\beta u_\alpha - \frac{2}{3} \partial_\gamma u_\gamma \delta_{\alpha\beta} \right) + \eta_v \partial_\gamma u_\gamma \delta_{\alpha\beta}. \tag{18}$$

The advantage of such approaches is their spatial locality, resulting in favorable $O(N)$ scaling, combined with ease of implementation and parallelization. The disadvantage is the introduction of additional degrees of freedom, and of additional (short) time scales which are not of direct interest. The coupling between solvent and solute varies from method to method. However, in all cases one takes the masses and the momenta of the solute particles explicitly into account, and makes sure that the total momentum is conserved.

Lattice models (Navier–Stokes, lattice Boltzmann) simulate a discretized field theory in which thermal fluctuations can be added, but also avoided if desired. Particle methods (Molecular Dynamics, Dissipative Particle Dynamics, Multi–Particle Collision Dynamics) simulate a system of interacting mass points, and therefore thermal fluctuations are always present. The particles may have size and structure or they may be just point particles. In the former case, the finite solvent size results in an additional potential of mean force between the beads. The solvent structure extends over unphysically large length scales, because the proper separation of scale between solute and solvent is not computationally realizable. In dynamic simulations of systems in thermal equilibrium [43], solvent structure requires that the system be equilibrated with the solvent in place, whereas for a structureless solvent the solute system can be equilibrated by itself, with substantial computational savings [43]. Finally, lattice models have a (rigorously) known solvent viscosity, whereas for particle methods the existing analytical expressions are only approximations (which however usually work quite well).

These considerations suggest that lattice methods are somewhat more flexible and versatile for soft–matter simulations. On the other hand, the coupling between solvent and immersed particles is less straightforward than for a pure particle system. The coupling between solid particles and a lattice–based fluid model will be discussed in detail in Sec. 4.

2.3.3
Molecular Dynamics (MD)

Molecular Dynamics is the most fundamental approach to soft–matter simulations. Here the solute particles are immersed in a bath of solvent molecules and Newton's equations of motion are solved numerically. In this case, it is impossible to make the solvent structureless – a structureless solvent would be an ideal gas of point particles, which never reaches thermal equilibrium. Furthermore, the model interaction potentials are stiff and considerable simulation time is spent following the motion of the solvent particles in their local "cages". These disadvantages are so severe that nowadays MD is rarely applied to soft–matter systems of the type we are discussing in this article.

2.3.4
Dissipative Particle Dynamics (DPD)

Dissipative Particle Dynamics, which has become quite popular in the soft–matter community [44–56], was developed to address the computational limitations of MD. A very soft interparticle potential, representing coarse–grained aggregates of molecules, enables a large time step to be used. Furthermore, a momentum–conserving Galilean–invariant thermostat is included, representing the degrees of freedom that have been lost in the coarse–graining process. Practically, these two parts are unrelated, such that it is legitimate to apply the DPD thermostat to a standard MD system. The DPD thermostat is consistent with macroscopic isothermal thermodynamics. Since this already introduces interparticle collisions, it is possible to run DPD using an ideal gas solvent and still achieve thermal equilibrium..

The key innovation in DPD is to apply the thermostat to particle *pairs*. A frictional damping is applied to the *relative* velocities between each neighboring pair, and a corresponding random force is added in a pairwise fashion also, such that Newton's third law holds exactly. The implementation is as follows. We define two functions $\zeta(r) \geq 0$, the relative friction coefficient for particle pairs with interparticle distance r, and $\sigma(r) \geq 0$, characterizing the strength of the stochastic force applied to the same particle pair. The fluctuation–dissipation theorem requires that

$$\sigma^2(r) = k_B T \zeta(r). \tag{19}$$

The functions have compact support, so that only near neighbors need be taken into account.

The frictional force on particle i is determined by projecting the relative velocities onto the interparticle separation ($\hat{r}_{ij} = \mathbf{r}_{ij} / |\mathbf{r}_{ij}|$):

$$\mathbf{F}_i^d = -\sum_j \zeta(r_{ij})\left[(\mathbf{v}_i - \mathbf{v}_j)\cdot\hat{r}_{ij}\right]\hat{r}_{ij}, \tag{20}$$

which conserves momentum exactly, $\sum_i \mathbf{F}_i^d = 0$. Similarly, the stochastic forces are directed along the interparticle separation, again so that momentum is conserved pair–by–pair,

$$\mathbf{F}_i^f = \sum_j \sigma(r_{ij})\,\eta_{ij}(t)\,\hat{r}_{ij}. \tag{21}$$

The noise η_{ij} satisfies the relations $\eta_{ij} = \eta_{ji}$, $\langle\eta_{ij}\rangle = 0$, and

$$\langle\eta_{ij}(t)\eta_{kl}(t')\rangle = 2(\delta_{ik}\delta_{jl} + \delta_{il}\delta_{jk})\delta(t - t'), \tag{22}$$

such that different pairs are statistically independent and $\sum_i \mathbf{F}_i^f = 0$. The equations of motion for a particle of mass m_i and momentum $\mathbf{p}_i$ are:

$$\frac{d}{dt}\mathbf{r}_i = \frac{1}{m_i}\mathbf{p}_i, \tag{23}$$

$$\frac{d}{dt}\mathbf{p}_i = \mathbf{F}_i^c + \mathbf{F}_i^d + \mathbf{F}_i^f. \tag{24}$$

Exploiting the relation between this stochastic differential equation and its Fokker–Planck equation, it can be shown that the fluctuation–dissipation theorem holds [46], and that the method therefore simulates a canonical ensemble. DPD can be extended to thermalize the perpendicular component of the interparticle velocity as well, thereby allowing more control over the transport properties of the model [49, 57].

2.3.5
Multi–Particle Collision Dynamics (MPCD)

This method [58–62] works with a system of ideal–gas particles and therefore has no artificial depletion forces. Free streaming of the particles,

$$\mathbf{r}_i(t + h) = \mathbf{r}_i(t) + h\mathbf{v}_i(t), \tag{25}$$

alternates with momentum and energy conserving collisions, which are implemented via a Monte Carlo procedure:

- Sub–divide the simulation volume into a regular array of cells.
- For each cell, determine the set of particles residing in it. For one particular cell, let these particles be numbered $i = 1,\ldots,n$. Then in each box:
- Determine the local center–of–mass velocity:

$$\mathbf{v}_{CM} = \frac{1}{n}\sum_{i=1}^n \mathbf{v}_i. \tag{26}$$

- For each particle in the cell, perform a Galilean transformation into the local center–of–mass system:

$$\tilde{\mathbf{v}}_i = \mathbf{v}_i - \mathbf{v}_{CM}. \tag{27}$$

- Within the local center–of–mass system, rotate all velocities within the cell by a random rotation matrix R:

$$\tilde{\mathbf{v}}_i' = \mathsf{R}\tilde{\mathbf{v}}_i. \tag{28}$$

- Transform back into the laboratory system:

$$\mathbf{v}_i' = \tilde{\mathbf{v}}_i' + \mathbf{v}_{CM}. \tag{29}$$

By suitable random shifts of the cells relative to the fluid, it is possible to recover strict Galilean invariance [59, 60]. MPCD results in hydrodynamic behavior on large length and time scales, and is probably the simplest and most efficient particle method to achieve this.

2.3.6
Lattice Boltzmann (LB)

Here one solves the Boltzmann equation, known from the kinetic theory of gases, in a fully discretized fashion. Space is discretized into a regular array of lattice sites, time is discretized, and velocities are chosen such that one time step will connect only nearby lattice sites. Free streaming along the lattice links alternates with local on–site collisions. Care must be taken to restore isotropy and Galilean invariance in the hydrodynamic limit, and asymptotic analysis is an indispensable tool in this process. Further details will be provided in the following chapters.

2.3.7
Navier-Stokes

It is possible to start from a discrete representation of Eqs. 17 but this has not been particularly popular in soft–matter simulations, due to the difficulty of including thermal fluctuations (but see Ref. [63]). Finite-difference methods share many technical similarities with LB and are roughly comparable in terms of computational resources. However, to our knowledge, no detailed benchmark comparisons are available as yet. In order to be competitive with LB, we believe that the solver must (i) make sure that mass and momentum are conserved within machine accuracy, as is the case for LB, and (ii) *not* work in the incompressible limit, in order to avoid the costly non–local constraints imposed by the typical Poisson solver for the pressure. The incompressible limit is an approximation, which eliminates the short time scales associated with wave–like motion. However, in soft matter the solute particles must be simulated on short inertial time scales, which requires that the solvent is simulated on rather short time scales as well. For this reason, we believe that enforcing an incompressibility constraint does not pose a real advantage, and it is instead preferable to allow for finite compressibility, such that one obtains an explicit and local algorithm. This idea is analogous to the Car–Parrinello method [64], where the Born–Oppenheimer constraint is also discarded, in favor of an approximate but adequate separation of time scales. For simulations of soft–matter systems coupled to a Navier–Stokes background, see Refs. [65–74].

3
The fluctuating lattice-Boltzmann equation

The motivation for the development of lattice gas cellular automata (LGCA) [75, 76] was to apply a highly simplified Molecular Dynamics (MD) to simulations of hydrodynamic flows. In LGCA, particles move along the links of a regular lattice, typically cubic or triangular. Each lattice direction is encoded with a label i and a vector $h\mathbf{c}_i$ connects neighboring pairs of sites. During each time step h, all particles with a direction i are displaced $h\mathbf{c}_i$ to an adjacent lattice site; thus $\mathbf{c}_i$ is the (constant) velocity of particles of type i. Interparticle interactions are reduced to collisions between particles on the same lattice site, such that the conservation laws for mass and momentum are satisfied; in single speed LGCA models [75, 76], mass conservation implies energy conservation as well. The lattice-Boltzmann (LB) method [77–80] was developed to reduce the thermal noise in LGCA, which requires extensive averaging to obtain statistically significant results.

The LB model preserves the structural simplicity of LGCA, but substitutes an ensemble-averaged collision operator for the detailed microscopic dynamics of the LGCA. The hydrodynamic flow fields develop without thermal noise, but the underlying connection with statistical mechanics is lost (Sec. 3.1). The LB model turns out to be more flexible than LGCA, and there is now a rich literature that includes thermal [81–86] and multiphase flows, involving both liquid–gas coexistence and multicomponent mixtures [87–96]. In the present article, we will consider only single–phase flows of a single solvent species, such that we can describe the dynamics in terms of a single particle type. The algorithm can be summarized by the equation

$$\nu_i(\mathbf{r} + \mathbf{c}_i h, t + h) = \nu_i^\star(\mathbf{r}, t) = \nu_i(\mathbf{r}, t) + \Delta_i\left(\boldsymbol{\nu}(\mathbf{r}, t)\right), \tag{30}$$

where $\nu_i(\mathbf{r}, t)$ is the number of particles that, at the discrete time t just prior to collision, reside at the lattice site $\mathbf{r}$, and have velocity $\mathbf{c}_i$; $\nu_i^\star(\mathbf{r}, t)$ indicates the velocity distribution immediately after collision. The difference Δ_i between the pre- and postcollision states is called the "collision operator" and depends on the complete set of populations at the site $\boldsymbol{\nu}(\mathbf{r}, t)$. The left hand side of Eq. 30 describes the advection of the populations along the links connecting neighboring lattice sites. The velocity set $\mathbf{c}_i$ is chosen such that each new position $\mathbf{r} + \mathbf{c}_i h$ is again at a lattice site; $\mathbf{c}_i = 0$ is possible.

For simplicity and computational efficiency, the number of velocities should be small. Therefore the set of velocities, $\mathbf{c}_i$, is typically limited to two or three neighbor shells, chosen to be compatible with the symmetry of the lattice. In two dimensions a single shell of 6 neighbors is sufficient for hydrodynamic flows, but a single set of cubic lattice vectors leads to anisotropic momentum diffusion, even at large spatial scales. Thus LB models employ a judicious mixture of neighboring shells, suitably weighted so that isotropy is recovered. We use the classification scheme introduced by Qian *et al.* [97]: for instance D2Q9 refers to an LB model on a square lattice in two dimensions, using nine velocities (zero, four nearest neighbors, four next–nearest neighbors), while D3Q19 indicates a three–dimensional model on a sim-

ple cubic lattice with nineteen velocities (zero, six nearest neighbors, twelve next–nearest neighbors).

3.1
Fluctuations

The difference between lattice gas and lattice Boltzmann lies in the nature of the ν_i. In a lattice gas ν_i is a Boolean variable (*i.e.* only the values zero and one are allowed), while in the lattice-Boltzmann equation it is a positive real–valued variable. In Sec. 3.6 we will consider the case where ν_i is a large positive integer, a conceptual model we call a "Generalized Lattice Gas" (GLG). Thinking of these models as a simplified Molecular Dynamics, and considering fluctuations in ν_i, it becomes clear what the key difference between LGCA and the LB equation is. We define a dimensionless "Boltzmann number", Bo, by the fluctuations in ν_i at a single site,

$$Bo = \frac{\left(\langle \nu_i^2 \rangle - \langle \nu_i \rangle^2 \right)^{1/2}}{\langle \nu_i \rangle}, \tag{31}$$

where $\langle \ldots \rangle$ denotes the ensemble average. One could define Boltzmann numbers for other observables, but they would all produce similar values. The important point is that Bo tells us how coarse–grained the model is, compared to microscopic MD: $Bo \sim 1$ (the maximum value) corresponds to a fully microscopic model where fluctuations are of the same order as the mean. This is exactly the case for lattice gas cellular automata, which should therefore be viewed as a simplified, but not coarse–grained MD. Conversely, deterministic LB algorithms, at sufficiently small Reynolds numbers, and with time–independent driving forces, bring the system to a stationary state with well–defined values for the ν_i. In other words, they are characterized by $Bo = 0$, which is the minimal value, corresponding to entirely deterministic physics.

Originally, LGCA and LB algorithms were developed to simulate macroscopic hydrodynamics. Here, a large Boltzmann number (order 1) is undesirable, since the hydrodynamic behavior is only revealed after extensive sampling. For many macroscopic applications a deterministic LB simulation at $Bo = 0$ is hence entirely appropriate. In reality, however, the Boltzmann number is finite, since the spatial domain in the physical system corresponding to a single lattice site is also finite. In soft–matter applications the spatial scales are so small that these fluctuations do need to be taken into account, although in many cases Bo is fairly small. This suggests it would be advantageous to introduce small thermal fluctuations into the LB algorithm, in a controlled fashion, by means of a *stochastic* collision operator [98–100]. The fluctuation–dissipation relation can be satisfied by enforcing consistency with fluctuating hydrodynamics [42] on large length and time scales. An important refinement is to thermalize the additional degrees of freedom that are not directly related to hydrodynamics [101], which leads to equipartition of fluctuation energy on all length scales. A comprehensive understanding of these approaches in terms of the statistical mechanics of LB systems has been achieved only recently [102].

The number variables, ν_i, can be connected to the hydrodynamic fields, mass density $\rho(\mathbf{r}, t)$, momentum density $\mathbf{j}(\mathbf{r}, t)$, and fluid velocity $\mathbf{u}(\mathbf{r}, t)$ ($\mathbf{j} = \rho \mathbf{u}$), by introducing the mass of an LB particle, m_p, and the mass density parameter

$$\mu = \frac{m_p}{b^3}; \tag{32}$$

here b is the lattice spacing and a three–dimensional lattice has been assumed. We then use the mass densities of the individual populations,

$$n_i(\mathbf{r}, t) = \mu \nu_i(\mathbf{r}, t), \tag{33}$$

to re–write the LB equation as

$$n_i(\mathbf{r} + \mathbf{c}_i h, t + h) = n_i^\star(\mathbf{r}, t) = n_i(\mathbf{r}, t) + \Delta_i\left(\mathbf{n}(\mathbf{r}, t)\right). \tag{34}$$

The mass and momentum densities, ρ and $\mathbf{j}$, are moments of the n_i's with respect to the velocity vectors,

$$\rho(\mathbf{r}, t) = \sum_i n_i(\mathbf{r}, t), \tag{35}$$

$$\mathbf{j}(\mathbf{r}, t) = \sum_i n_i(\mathbf{r}, t) \mathbf{c}_i, \tag{36}$$

and therefore, the collision operator must satisfy the constraints of mass and momentum conservation,

$$\sum_i \Delta_i = \sum_i \Delta_i \mathbf{c}_i = 0. \tag{37}$$

The LB algorithm has both locality and conservation laws built in, but two important symmetries have been lost. The system will in general exhibit cubic anisotropy, due to the underlying lattice symmetries, and violate Galilean invariance, due to the finite number of velocities. Isotropy can be restored in the large–scale limit by a careful choice of velocities and collision operator; however, the broken Galilean invariance restricts the method to flows with $u \ll c_i$. Since the speed of sound c_s, the maximum velocity with which any signal can travel through the system, is of the order of the c_i, the condition actually means low Mach number (Ma) flow,

$$Ma = u/c_s \ll 1. \tag{38}$$

In soft–matter applications, variations in fluid density are small and there is a universal equation of state characterized by the pressure at the mean fluid density and temperature, $p_0 = p(\rho_0, T)$, and the speed of sound $c_s = (\partial p/\partial \rho)^{1/2}$ [42],

$$p = p_0 + (\rho - \rho_0) c_s^2. \tag{39}$$

Within an unimportant constant ($p_0 - \rho_0 c_s^2$), Eq. 39 can be replaced by the relation

$$p = \rho c_s^2, \tag{40}$$

which fits well to the linear structure of Eq. 34. The value of c_s is immaterial except that it establishes a time-scale separation between sound propagation and viscous diffusion of momentum. For this reason, a model where c_s is unphysically small

may be used, so long as the dimensionless number $C_\eta = \rho c_s l / \eta$ is sufficiently large; here l is a characteristic length in the system and η is the shear viscosity of the fluid. For polymers and colloids, $C_\eta \sim 10 - 1000$, but values of C_η in excess of 10 lead to quantitatively similar results.

The simplest equation of state of the form of Eq. 40 is an ideal gas,

$$p = \frac{\rho}{m_p} k_B T, \tag{41}$$

where T is the absolute temperature and k_B Boltzmann's constant. Comparison with Eq. 40 yields

$$k_B T = m_p c_s^2. \tag{42}$$

The temperature is then determined by choosing values for the discretization parameters b and h ($c_s \sim b/h$), and the LB particle mass m_p. The parameter m_p controls the noise level in stochastic LB simulations [102]: the smaller m_p (at fixed c_s), the smaller the temperature (or the noise level). This makes physical sense, since small m_p means that a fixed amount of mass ρb^3 is distributed onto many particles, and therefore the fluctuations are small.

In this section we will study the connection between the LB equation, Eq. 34, and the equations of fluctuating hydrodynamics [42],

$$\partial_t \rho + \partial_\alpha j_\alpha = 0, \tag{43}$$
$$\partial_t j_\alpha + \partial_\beta \left(\rho c_s^2 \delta_{\alpha\beta} + \rho u_\alpha u_\beta \right) = \partial_\beta \sigma_{\alpha\beta} + \partial_\beta \sigma_{\alpha\beta}^f. \tag{44}$$

The Greek indexes denote Cartesian components, $\delta_{\alpha\beta}$ is the Kronecker delta, and the Einstein summation convention is implied. The viscous stress has a Newtonian constitutive law,

$$\sigma_{\alpha\beta} = \eta_{\alpha\beta\gamma\delta} \partial_\gamma u_\delta, \tag{45}$$

and for an isotropic fluid

$$\eta_{\alpha\beta\gamma\delta} = \eta \left(\delta_{\alpha\gamma}\delta_{\beta\delta} + \delta_{\alpha\delta}\delta_{\beta\gamma} - \frac{2}{3}\delta_{\alpha\beta}\delta_{\gamma\delta} \right) + \eta_v \delta_{\alpha\beta}\delta_{\gamma\delta}, \tag{46}$$

with shear and bulk viscosities η and η_v. The fluctuating stress tensor, $\sigma_{\alpha\beta}^f$, is a Gaussian random variable characterized by zero mean, $\left\langle \sigma_{\alpha\beta}^f \right\rangle = 0$, and a covariance matrix

$$\left\langle \sigma_{\alpha\beta}^f \left(\mathbf{r}, t \right) \sigma_{\gamma\delta}^f \left(\mathbf{r}', t' \right) \right\rangle = 2 k_B T \eta_{\alpha\beta\gamma\delta} \delta \left(\mathbf{r} - \mathbf{r}' \right) \delta \left(t - t' \right). \tag{47}$$

In the limit that $T \to 0$, $\sigma_{\alpha\beta}^f$ vanishes, and the Navier-Stokes equations are recovered.

We begin our analysis with a general description of the dynamics of the lattice-Boltzmann equation, based on a Chapman-Enskog expansion (Sec. 3.2). Then we consider the equilibrium distribution for the D3Q19 model (Sec. 3.3), followed by deterministic (Sec. 3.4) and stochastic (Sec. 3.5) collision operators. Finally we consider the connection of the fluctuating LB model to statistical mechanics (Sec. 3.6) and the effects of external forces (Sec. 3.7).

3.2
Chapman–Enskog expansion

The Navier–Stokes description of a fluid is more coarse–grained than the original LB equation, and to connect the microscopic scales with the hydrodynamic scales we follow a standard asymptotic analysis [103]. We first introduce a dimensionless scaling parameter $\varepsilon \ll 1$ and write

$$\mathbf{r}_1 = \varepsilon \mathbf{r}. \tag{48}$$

The idea is to measure spatial positions with a ruler that has such a coarse scale that details at the lattice level are not resolved. The position $\mathbf{r}_1$ then corresponds to the number read off from this coarse–grained ruler; for example instead of talking about 1000 nanometers, we talk about one micrometer. For two points to be distant on the hydrodynamic scale, it is not sufficient that $|\Delta \mathbf{r}|$ is large, but rather that $|\Delta \mathbf{r}_1|$ is large. However, from the perspective of practical computation, the degree of coarse graining is never as extensive as implied by our analysis; the calculations would take far too long. Instead there is usually only a few grid points separating the lattice scale from the smallest hydrodynamic scale. Surprisingly the LB method can be quite accurate, even in these circumstances [99, 104].

In a similar way, we can also introduce a coarse–grained clock for the time variable, and write

$$t_1 = \varepsilon t. \tag{49}$$

The fact that we choose the same factor ε for both space and time is related to the typical scaling of wave–like phenomena, where the time scale of a process is *linearly* proportional to the corresponding length scale. However, hydrodynamics also includes diffusion of momentum, where the time scale is proportional to the *square* of the length scale. These processes occur on a much longer time scale, and to capture the slow dynamics we introduce a second clock that is even more coarse–grained,

$$t_2 = \varepsilon^2 t. \tag{50}$$

We can therefore distinguish between "short times" on the hydrodynamic scale, characterized by $t_s = t_1/\varepsilon$, and "long times", where $t_l = t_2/\varepsilon^2$. Both t_s and t_l are implicitly large on the lattice scale, with the hydrodynamic limit being reached as $\varepsilon \to 0$. But once again, practical computation limits the separation between the time scales h, t_s, and t_l to one or two orders of magnitude each.

In the "multi–time scale" analysis, the LB population densities may be considered to be functions of the coarse–grained position and times, $\mathbf{r}_1$, t_1, and t_2; $n_i \equiv n_i(\mathbf{r}_1, t_1, t_2)$. When the algorithm proceeds by one time step, $t \to t + h$, $t_1 \to t_1 + \varepsilon h$, and $t_2 \to t_2 + \varepsilon^2 h$. The LB equation in terms of the coarse-grained variables is then,

$$n_i(\mathbf{r}_1 + \varepsilon \mathbf{c}_i h, t_1 + \varepsilon h, t_2 + \varepsilon^2 h) - n_i(\mathbf{r}_1, t_1, t_2) = \Delta_i(\mathbf{n}(\mathbf{r}_1, t_1, t_2)). \tag{51}$$

The population densities are slowly varying functions of coarse-grained variables, and we may obtain hydrodynamic behavior by a Taylor expansion of n_i (Eq. 51) to second order in powers of ε:

$$n_i\left(\mathbf{x}+\delta\mathbf{x}\right)=n_i\left(\mathbf{x}\right)+\sum_k\frac{\partial n_i}{\partial x_k}\delta x_k+\frac{1}{2}\sum_{kl}\frac{\partial^2 n_i}{\partial x_k\partial x_l}\delta x_k\delta x_l+\dots,\qquad(52)$$

where we use $\mathbf{x}$ to indicate the coarse-grained variables, $[\mathbf{r}_1, t_1, t_2]$. Since the distribution function itself depends on the degree of coarse–graining, we must take the ε dependence of the n_i and Δ_i into account as well:

$$n_i = n_i^{(0)} + \varepsilon n_i^{(1)} + O(\varepsilon^2), \qquad(53)$$
$$\Delta_i = \Delta_i^{(0)} + \varepsilon\Delta_i^{(1)} + \varepsilon^2\Delta_i^{(2)} + O(\varepsilon^3). \qquad(54)$$

The conservation laws for mass and momentum must hold independently of the value of ε, and thus at every order k:

$$\sum_i \Delta_i^{(k)} = \sum_i \Delta_i^{(k)}\mathbf{c}_i = 0. \qquad(55)$$

Inserting these expansions into Eq. 51, and collecting terms at different orders of ε, we obtain:

- at order ε^0,
$$\Delta_i^{(0)} = 0; \qquad(56)$$

- at order ε^1,
$$(\partial_{t_1} + \mathbf{c}_i\cdot\partial_{\mathbf{r}_1})\,n_i^{(0)} = h^{-1}\Delta_i^{(1)}; \qquad(57)$$

- at order ε^2,
$$\partial_{t_2}n_i^{(0)} + \frac{h}{2}\left(\partial_{t_1}+\mathbf{c}_i\cdot\partial_{\mathbf{r}_1}\right)^2 n_i^{(0)} + \left(\partial_{t_1}+\mathbf{c}_i\cdot\partial_{\mathbf{r}_1}\right)n_i^{(1)} = h^{-1}\Delta_i^{(2)}. \quad(58)$$

Subsequently, it will prove useful to eliminate the second occurrence of $n_i^{(0)}$ from Eq. 58, by using Eq. 57:

$$\partial_{t_2}n_i^{(0)} + \frac{1}{2}\left(\partial_{t_1}+\mathbf{c}_i\cdot\partial_{\mathbf{r}_1}\right)\left(n_i^{\star(1)} + n_i^{(1)}\right) = h^{-1}\Delta_i^{(2)}, \qquad(59)$$

where $n_i^\star = n_i + \Delta_i$ is the post-collision population in direction i.

The multi–time–scale expansion of Eq. 51 is based on the physical time-scale separation between collisions ($t \sim h$), sound propagation ($t \sim h/\varepsilon$), and momentum diffusion ($t \sim h/\varepsilon^2$). Eqs. 56–58 make the implicit assumption that these three relaxations can be considered separately, which allows the collision operator at order $k+1$ to be calculated from the distribution functions at order k. In essence, the collision dynamics at order $k + 1$ is slaved to the lower-order distributions. The zeroth–order collision operator must be a function of $\mathbf{n}^{(0)}$ only,

$$\Delta_i^{(0)} = \Delta_i(\mathbf{n}^{(0)}), \qquad(60)$$

which, in conjunction with Eq. 56, shows that $\mathbf{n}^{(0)}$ is a collisional invariant; thus we can associate $\mathbf{n}^{(0)}$ with the equilibrium distribution $\mathbf{n}^{eq}$ [105]. In order to avoid spurious conserved quantities, the equilibrium distribution should be a function of local values of the conserved variables, ρ and $\mathbf{j}$, only. In a homogeneous system, with

fixed mass and momentum densities, $\mathbf{n}^{eq}(\rho, \mathbf{j}) = \mathbf{n}^{(0)}(\rho, \mathbf{j})$ is stationary in time. A stochastic collision operator (see Sec. 3.5) cannot satisfy Eq. 56 and therefore must enter the Chapman-Enskog expansion at order ε.

From Eq. 53 we can derive analogous ε expansions for ρ and $\mathbf{j}$,

$$\rho = \rho^{(0)} + \varepsilon\rho^{(1)} + \varepsilon^2\rho^{(2)} + O(\varepsilon^3), \tag{61}$$

$$\mathbf{j} = \mathbf{j}^{(0)} + \varepsilon\mathbf{j}^{(1)} + \varepsilon^2\mathbf{j}^{(2)} + O(\varepsilon^3). \tag{62}$$

However, inserting these expansions into $n_i^{(0)}(\rho, \mathbf{j})$, shows that

$$0 = \rho^{(1)} = \rho^{(2)} = \ldots, \tag{63}$$

$$0 = \mathbf{j}^{(1)} = \mathbf{j}^{(2)} = \ldots; \tag{64}$$

otherwise $n_i^{(0)}$ would have contributions of order ε and above, in contradiction to Eq. 56. The mass and momentum densities can therefore be defined as moments of the equilibrium distribution as well,

$$\sum_i n_i^{eq} = \rho, \tag{65}$$

$$\sum_i n_i^{eq} \mathbf{c}_i = \mathbf{j}. \tag{66}$$

We can analyze the dynamics of the LB model on large length and time scales by taking moments of Eqs. 57 and 59 with respect to the LB velocity set $\mathbf{c}_i$. From the zeroth moment, $\sum_i \cdots$, we obtain the continuity equation on the t_1 time scale (Eq. 55),

$$\partial_{t_1}\rho + \partial_{1\alpha}j_\alpha = 0, \tag{67}$$

and incompressibility on the t_2 time scale (Eqs. 55, 63, and 64)

$$\partial_{t_2}\rho = 0. \tag{68}$$

In Eq. 67 we have used the shorthand notation $\partial_{1\alpha}$ for the α component of the spatial derivative $\partial_{\mathbf{r}_1}$.

The first moment, $\sum_i \cdots c_{i\alpha}$, leads to momentum conservation equations on both time scales (Eqs. 55, 63, and 64):

$$\partial_{t_1}j_\alpha + \partial_{1\beta}\pi_{\alpha\beta}^{(0)} = 0, \tag{69}$$

$$\partial_{t_2}j_\alpha + \frac{1}{2}\partial_{1\beta}\left(\pi_{\alpha\beta}^{\star(1)} + \pi_{\alpha\beta}^{(1)}\right) = 0, \tag{70}$$

where $\pi_{\alpha\beta}$ is the momentum flux or second moment, [1]

$$\pi_{\alpha\beta} = \sum_i n_i c_{i\alpha}c_{i\beta}. \tag{71}$$

Momentum is conserved on both the t_1 and t_2 time scales, because, in the hydrodynamic limit, the coupling between acoustic and diffusive modes is very weak.

---

[1] There is a notational inconsistency in Ref. [102]. In Eqs. 71 and 73 of that paper the superscript neq should be replaced by a superscript 1, and in Eq. 79 $Q_{\alpha\beta}$ should be $Q_{\alpha\beta}^1$.

First, sound waves propagate with negligible viscous damping; then the residual pressure field in a nearly incompressible fluid relaxes by momentum diffusion. We can write the conservation laws on each time scale separately, as in Eqs. 69 and 70, or combine them into a single equation in the lattice–scale variables $\mathbf{r} = \mathbf{r}_1/\varepsilon$ and $t = t_1/\varepsilon = t_2/\varepsilon^2$. The hydrodynamic fields depend on $\mathbf{r}$ and t parametrically, through their dependence on the coarse-grained variables $\mathbf{r}_1$, t_1, t_2. Using ∂_α for a component of $\partial_{\mathbf{r}}$, we have

$$\partial_\alpha = \varepsilon \partial_{1\alpha}, \tag{72}$$

$$\partial_t = \varepsilon \partial_{t_1} + \varepsilon^2 \partial_{t_2}. \tag{73}$$

The combined equations for the mass and momentum densities on the lattice space and time scales are then:

$$\partial_t \rho + \partial_\alpha j_\alpha = 0, \tag{74}$$

$$\partial_t j_\alpha + \partial_\beta \pi_{\alpha\beta}^{eq} + \frac{1}{2} \partial_\beta \left(\pi_{\alpha\beta}^{\star neq} + \pi_{\alpha\beta}^{neq} \right) = 0, \tag{75}$$

where from Eq. 53, $\pi_{\alpha\beta}^{eq} = \pi_{\alpha\beta}^{(0)}$ and $\pi_{\alpha\beta}^{neq} = \varepsilon \pi_{\alpha\beta}^{(1)}$.

Finally, we can derive a relation between the pre-collision and post-collision momentum fluxes, $\pi_{\alpha\beta}$ and $\pi_{\alpha\beta}^\star$, by taking the second moment of Eq. 57:

$$\partial_{t_1} \pi_{\alpha\beta}^{(0)} + \partial_{1\gamma} \Phi_{\alpha\beta\gamma}^{(0)} = h^{-1} \left(\pi_{\alpha\beta}^{\star(1)} - \pi_{\alpha\beta}^{(1)} \right), \tag{76}$$

where $\Phi_{\alpha\beta\gamma}$ is the third moment of the distribution,

$$\Phi_{\alpha\beta\gamma} = \sum_i n_i c_{i\alpha} c_{i\beta} c_{i\gamma}. \tag{77}$$

We note that $\pi_{\alpha\beta}^{eq}$ is a collisional invariant and therefore remains unchanged by the collision process. In terms of the lattice variables,

$$\pi_{\alpha\beta}^{\star neq} = \pi_{\alpha\beta}^{neq} + h \left(\partial_t \pi_{\alpha\beta}^{eq} + \partial_\gamma \Phi_{\alpha\beta\gamma}^{eq} \right). \tag{78}$$

Equation 74 shows that continuity (Eq. 43) is automatically satisfied by any LB model. The Navier–Stokes equation (Eq. 44) will be satisfied, *if* we succeed in ensuring that the Euler stress $\rho c_s^2 \delta_{\alpha\beta} + \rho u_\alpha u_\beta$, the Newtonian viscous stress, $\sigma_{\alpha\beta}$ (Eq. 45), and the fluctuating stress $\sigma_{\alpha\beta}^f$ (Eq. 47) are given correctly by the sum of the momentum fluxes in Eq. 75. Since $\pi_{\alpha\beta}^{eq}$ depends *only* on ρ and $\mathbf{j}$, it must be identified with the Euler stress:

$$\pi_{\alpha\beta}^{eq} = \rho c_s^2 \delta_{\alpha\beta} + \rho u_\alpha u_\beta. \tag{79}$$

The viscous stress and fluctuating stresses must then be contained in $(\pi_{\alpha\beta}^{\star neq} + \pi_{\alpha\beta}^{neq})/2$.

This is about as far as we can go in complete generality. In order to proceed further we need to consider specific equilibrium distributions and collision operators. The results of this subsection suggest the following approach towards constructing an LB method which (asymptotically) simulates the fluctuating Navier–Stokes equations:

- Find a set of equilibrium populations n_i^{eq} such that

  – $$\sum_i n_i^{eq} = \rho; \tag{80}$$

  – $$\sum_i n_i^{eq} \mathbf{c}_i = \mathbf{j}; \tag{81}$$

  – $$\sum_i n_i^{eq} c_{i\alpha} c_{i\beta} = \rho c_s^2 \delta_{\alpha\beta} + \rho u_\alpha u_\beta. \tag{82}$$

- Find a collision operator Δ_i with the properties:

  – $$\sum_i \Delta_i = 0; \tag{83}$$

  – $$\sum_i \Delta_i \mathbf{c}_i = 0; \tag{84}$$

  – The nonequilibrium momentum flux $(\pi_{\alpha\beta}^{\star neq} + \pi_{\alpha\beta}^{neq})/2$ must be connected with the sum of viscous and fluctuating stresses.

In the following subsections, we will follow this procedure for the three-dimensional D3Q19 model.

3.3
D3Q19 model I: Equilibrium populations

Early LB models [78–80] inherited their equilibrium distributions from LGCA, along with macroscopic manifestations of the broken Galilean invariance: an incorrect advection velocity and a velocity dependent pressure. Subsequently a new equilibrium distribution was proposed that restored Galilean invariance at the macroscopic level [97, 106], but with the loss of the connection to statistical mechanics. The idea was to ensure that the first few moments of n_i^{eq} matched those derived from the Maxwell–Boltzmann distribution for a dilute gas [105],

$$n(\mathbf{c}|\rho, \mathbf{u}, T) = \rho \left(\frac{m_p}{2\pi k_B T} \right)^{3/2} \exp\left(-\frac{m_p}{2k_B T} (\mathbf{c} - \mathbf{u})^2 \right): \tag{85}$$

specifically;

$$\int d^3\mathbf{c}\, n(\mathbf{c}) = \rho, \tag{86}$$

$$\int d^3\mathbf{c}\, n(\mathbf{c}) c_\alpha = \rho u_\alpha, \tag{87}$$

$$\int d^3\mathbf{c}\, n(\mathbf{c}) c_\alpha c_\beta = \frac{\rho k_B T}{m_p} \delta_{\alpha\beta} + \rho u_\alpha u_\beta = \rho c_s^2 \delta_{\alpha\beta} + \rho u_\alpha u_\beta. \tag{88}$$

With these moments the Euler hydrodynamic equations (*c.f.* Eqs. 43 and 44),

$$\partial_t \rho + \partial_\alpha j_\alpha = 0, \tag{89}$$
$$\partial_t j_\alpha + \partial_\beta \left(\rho c_s^2 \delta_{\alpha\beta} + \rho u_\alpha u_\beta \right) = 0, \tag{90}$$

may be derived from the continuum version of the Chapman-Enskog expansion [105]. The viscous stress arises from the non-equilibrium distribution (*c.f.* Sec. 3.2).

An expansion of the Maxwell–Boltzmann equilibrium distribution (Eq. 85) at low velocities suggests the following ansatz [97, 106] for the discrete velocity equilibrium,

$$n_i^{eq}(\rho, \mathbf{u}) = a^{c_i}\rho\left(1 + A\mathbf{u}\cdot\mathbf{c}_i + B(\mathbf{u}\cdot\mathbf{c}_i)^2 + Cu^2\right) \tag{91}$$

with suitably adjusted coefficients a^{c_i}, A, B, and C. The rationale for Eq. 91 is that the equilibrium momentum flux is quadratic in the flow velocity $\mathbf{u}$ (Eq. 88); it therefore makes sense to construct a similar form for n_i^{eq}. A drawback of Eq. 91 is that n_i^{eq} may be negative if u becomes sufficiently large. This can be avoided by more general equilibrium distributions, which are equivalent to Eq. 91 up to order u^2 [107–109].

The prefactors $a^{c_i} > 0$ are normalized such that

$$\sum_i a^{c_i} = 1, \tag{92}$$

which ensures that Eq. 65 is satisfied in the special case $\mathbf{u} = 0$. The notation in Eq. 91 was chosen in order to indicate explicitly that the weights depend only on the absolute value of the speed c_i, but not its direction; this follows from the rotational symmetries of the LB model. The coefficients A, B, C are here independent of c_i. There are other LB models, like D3Q18 [106], where this condition is not imposed, and A, B, and C depend on c_i as well; however, such models are only hydrodynamically correct in the incompressible limit [98], and cannot be straightforwardly interpreted in terms of statistical mechanics (see Sec. 3.6). We will not consider such models.

In a cubic lattice, symmetry dictates the following relations for the low–order velocity moments of the weights,

$$\sum_i a^{c_i} c_{i\alpha} = 0, \tag{93}$$

$$\sum_i a^{c_i} c_{i\alpha} c_{i\beta} = C_2\,\delta_{\alpha\beta}, \tag{94}$$

$$\sum_i a^{c_i} c_{i\alpha} c_{i\beta} c_{i\gamma} = 0, \tag{95}$$

$$\sum_i a^{c_i} c_{i\alpha} c_{i\beta} c_{i\gamma} c_{i\delta} = C_4'\,\delta_{\alpha\beta\gamma\delta} + C_4\left(\delta_{\alpha\beta}\delta_{\gamma\delta} + \delta_{\alpha\gamma}\delta_{\beta\delta} + \delta_{\alpha\delta}\delta_{\beta\gamma}\right), \tag{96}$$

where the values of the parameters C_2, C_4 and C_4' depend on the details of the choice of the coefficients a^{c_i}. The tensor $\delta_{\alpha\beta\gamma\delta}$ is unity when $\alpha = \beta = \gamma = \delta$ and zero otherwise. Rotational invariance of the stress tensor requires that $C_4' = 0$.

The results in Eqs. 92–96 allow us to calculate the moments of Eq. 91 up to second order. Consistency with the mass density, momentum density and Euler stress for a given ρ and $\mathbf{u}$, uniquely determines the equilibrium distribution,

$$n_i^{eq}(\rho, \mathbf{u}) = a^{c_i}\rho\left(1 + \frac{\mathbf{u}\cdot\mathbf{c}_i}{c_s^2} + \frac{(\mathbf{u}\cdot\mathbf{c}_i)^2}{2c_s^4} - \frac{u^2}{2c_s^2}\right), \tag{97}$$

with the speed of sound $c_s^2 = C_2$, and the weights adjusted such that $C_4' = 0$ and $C_4 = C_2^2$. These two latter conditions, together with the normalization condition Eq. 92, form a set of three equations for the coefficients a^{c_i}. Therefore at least three speeds, or three shells of neighbors, are needed to satisfy the constraints. We consider the D3Q19 model, which incorporates the three smallest speeds on a simple–cubic lattice. Here one obtains $a^0 = 1/3$ for the stationary particles, $a^1 = 1/18$ for the six nearest–neighbor directions, and $a^{\sqrt{2}} = 1/36$ for the twelve next–nearest neighbors. The speed of sound is then $c_s^2 = (1/3)(b/h)^2$.

We now turn back to the results of the previous subsection, since the explicit form of n_i^{eq} allows us to pursue the analysis further. We first calculate the equilibrium third–order moment (Eq. 77) using Eq. 97:

$$\Phi_{\alpha\beta\gamma}^{eq} = \rho c_s^2 \left(u_\alpha \delta_{\beta\gamma} + u_\beta \delta_{\alpha\gamma} + u_\gamma \delta_{\alpha\beta} \right). \tag{98}$$

In fact Eq. 98 is model independent to order u^2, since only the linear term in $\mathbf{u} \cdot \mathbf{c}_i$ contributes. To close the hydrodynamic equations for the mass and momentum densities (Eqs. 74 and 75) we need expressions for the pre–collision and post–collision momentum fluxes, $\pi_{\alpha\beta}^{\star neq}$ and $\pi_{\alpha\beta}^{neq}$. From Eq. 76 we can obtain an expression for $\pi_{\alpha\beta}^{\star neq} - \pi_{\alpha\beta}^{neq}$ in terms of the velocity gradient,

$$\rho c_s^2 \left(\partial_{1\alpha} u_\beta + \partial_{1\beta} u_\alpha \right) = h^{-1} \left(\pi_{\alpha\beta}^{\star(1)} - \pi_{\alpha\beta}^{(1)} \right), \tag{99}$$

where we have used Eqs. 67 and 69 to rewrite the time derivative of $\pi_{\alpha\beta}^{(0)}$ in terms of spatial derivatives of ρ and $\mathbf{u}$. In arriving at Eq. 99, we have neglected terms of order u^3, consistent with the low Mach number limit we are considering. Finally, Eq. 99 can be rewritten in terms of the unscaled variables,

$$\pi_{\alpha\beta}^{\star neq} - \pi_{\alpha\beta}^{neq} = h\rho c_s^2 \left(\partial_\alpha u_\beta + \partial_\beta u_\alpha \right). \tag{100}$$

To obtain a further relation for the non-equilibrium momentum fluxes, we must consider the collision operator in more detail.

3.4
D3Q19 model II: Deterministic collision operator

In a deterministic model, the collision operator Δ_i is a unique function of the distribution $\mathbf{n}$. Therefore, we can obtain the Chapman–Enskog ordering of Δ_i via a Taylor expansion with respect to $\mathbf{n}$:

$$\begin{aligned} \Delta_i \left(\mathbf{n} \right) &= \Delta_i \left(\mathbf{n}^{(0)} + \varepsilon \mathbf{n}^{(1)} + \varepsilon^2 \mathbf{n}^{(2)} + \dots \right) \\ &= \Delta_i \left(\mathbf{n}^{(0)} \right) + \varepsilon \sum_j \left(\frac{\partial \Delta_i}{\partial n_j} \right) \Bigg|_{\mathbf{n}^{(0)}} n_j^{(1)} + O \left(\varepsilon^2 \right). \end{aligned} \tag{101}$$

The analysis of Sec. 3.2 has shown that $\Delta_i(\mathbf{n}^{(0)}) = 0$ (Eq. 60), and that hydrodynamic behavior is determined by the order ε^1 collision operator,

$$\Delta_i^{(1)} = \sum_j \left(\frac{\partial \Delta_i}{\partial n_j} \right) \bigg|_{\mathbf{n}^{(0)}} n_j^{(1)}. \tag{102}$$

Although $\Delta_i^{(2)}$ appears at second order in the Chapman-Enskog expansion (Eq. 58), it makes no contribution to the change in mass and momentum densities (Eq. 55). However, $\Delta_i^{(1)}$ contributes to a first–order change in the viscous stress (Eq. 78), which enters into the momentum equation at second order (Eq. 70). It is therefore reasonable to construct the collision operator with the form of $\Delta_i^{(1)}$:

$$\Delta_i = \sum_j \mathcal{L}_{ij} n_j^{neq}, \tag{103}$$

where $\mathcal{L}_{ij}$ is a matrix of constant coefficients. Thus to lowest order in ε, the collision process is a linear transformation between the non-equilibrium distributions for each velocity:

$$n_i^{\star neq} = \sum_j \left(\delta_{ij} + \mathcal{L}_{ij} \right) n_j^{neq}. \tag{104}$$

The simplest such collision operator is the lattice BGK (Bhatnagar–Gross–Krook) model [77], $\mathcal{L}_{ij} = -\delta_{ij}/\tau$, where the collisional relaxation time τ is related to the viscosity. Here we will work within the more general framework of the multi–relaxation time (MRT) model [110], for which the lattice BGK model is a special case.

Polynomials in the dimensionless velocity vectors, $\hat{\mathbf{c}}_i = \mathbf{c}_i/c$ ($c = b/h$), form a basis for a diagonal representation of $\mathcal{L}_{ij}$ [110], which allows for a more general and stable LB model with the same level of computational complexity as the BGK version [111]. Orthogonal basis vectors, $\mathbf{e}_k$, are constructed from outer products of the vectors $\hat{\mathbf{c}}_i$. For example:

$$e_{0i} = 1, \tag{105}$$
$$e_{1i} = \hat{c}_{ix}, \tag{106}$$
$$e_{2i} = \hat{c}_{iy}, \tag{107}$$
$$e_{3i} = \hat{c}_{iz}. \tag{108}$$

There are six quadratic polynomials, which are given in Table 1 as basis vectors $\mathbf{e}_4 - \mathbf{e}_9$. A Gram–Schmidt procedure ensures that all the basis vectors are mutually orthogonal with respect to a set of positive weights, $q^{c_i} > 0$,

$$\sum_i q^{c_i} e_{ki} e_{li} = w_k \delta_{kl}. \tag{109}$$

The weights are restricted by the same symmetries as the coefficients in the equilibrium distribution a^{c_i}, but are not necessarily the same; in the D3Q19 model there are then three independent values of q^{c_i}. The normalization factors, $w_k > 0$, are related to the choice of basis vectors

$$w_k = \sum_i q^{c_i} e_{ki}^2. \tag{110}$$

Table 1. Basis vectors of the D3Q19 model. Each row corresponds to a different basis vector, with the actual polynomial in $\hat{c}_{i\alpha} = c_{i\alpha}/c$ shown in the second column. The normalizing factor for each basis vector is in the third column. The polynomials form an orthogonal set when $q^{ci} = a^{ci}$ (Eq. 109).

k	e_{ki}	w_k
0	1	1
1	$\hat{c}_{ix}$	$1/3$
2	$\hat{c}_{iy}$	$1/3$
3	$\hat{c}_{iz}$	$1/3$
4	$\hat{c}_i^2 - 1$	$2/3$
5	$3\hat{c}_{ix}^2 - \hat{c}_i^2$	$4/3$
6	$\hat{c}_{iy}^2 - \hat{c}_{iz}^2$	$4/9$
7	$\hat{c}_{ix}\hat{c}_{iy}$	$1/9$
8	$\hat{c}_{iy}\hat{c}_{iz}$	$1/9$
9	$\hat{c}_{iz}\hat{c}_{ix}$	$1/9$
10	$(3\hat{c}_i^2 - 5)\hat{c}_{ix}$	$2/3$
11	$(3\hat{c}_i^2 - 5)\hat{c}_{iy}$	$2/3$
12	$(3\hat{c}_i^2 - 5)\hat{c}_{iz}$	$2/3$
13	$(\hat{c}_{iy}^2 - \hat{c}_{iz}^2)\hat{c}_{ix}$	$2/9$
14	$(\hat{c}_{iz}^2 - \hat{c}_{ix}^2)\hat{c}_{iy}$	$2/9$
15	$(\hat{c}_{ix}^2 - \hat{c}_{iy}^2)\hat{c}_{iz}$	$2/9$
16	$3\hat{c}_i^4 - 6\hat{c}_i^2 + 1$	2
17	$(2\hat{c}_i^2 - 3)(3\hat{c}_{ix}^2 - \hat{c}_i^2)$	$4/3$
18	$(2\hat{c}_i^2 - 3)(\hat{c}_{iy}^2 - \hat{c}_{iz}^2)$	$4/9$

Within the D3Q19 model, polynomials up to second order are complete, but at third–order there is some deflation; for example, $\hat{c}_{ix}^3$ is equivalent to $\hat{c}_{ix}$. In fact, there are only six independent third–order and three independent fourth–order polynomials in the D3Q19 model. Beyond fourth order, all polynomials deflate to lower orders, so the basis vectors in Table 1 form a complete set for the D3Q19 model.

The basis vectors can be used to construct a complete set of moments of the LB distribution,

$$m_k = \sum_i e_{ki} n_i, \tag{111}$$

which allows for a diagonal representation of the collision operator [110, 112], as will be made clear later. Hydrodynamic variables are related to the moments up to quadratic order in $\hat{c}_i$ (*c.f.* Table 1):

$$\rho = m_0, \tag{112}$$

$$j_x = m_1 c, \tag{113}$$

$$j_y = m_2 c, \tag{114}$$

$$j_z = m_3 c, \tag{115}$$

$$\pi_{xx} = (m_0 + m_4 + m_5)c^2/3, \tag{116}$$

$$\pi_{yy} = (2m_0 + 2m_4 - m_5 + 3m_6)c^2/6, \tag{117}$$

$$\pi_{zz} = (2m_0 + 2m_4 - m_5 - 3m_6)c^2/6, \tag{118}$$

$$\pi_{xy} = m_7 c^2, \tag{119}$$

$$\pi_{yz} = m_8 c^2, \tag{120}$$

$$\pi_{zx} = m_9 c^2. \tag{121}$$

There are additional degrees of freedom in the D3Q19 model beyond those required for the conserved variables and stresses (Eqs. 112–121). These "kinetic" or "ghost" [101] moments do not play a role in the large-scale dynamics [102], but they are important for proper thermalization [101] and near boundaries [113].

The basis vectors in Table 1 are complete but not unique. Besides trivial variations in the Gram–Schmidt orthogonalization, there is a substantive difference that depends on the choice of the weighting factors q^{c_i}: these factors determine both the result of the orthogonalization procedure, as well as the back transformation from moments m_k to populations n_i. This is most easily seen from the observation that Eq. 109 can be rewritten as the standard orthonormality relation [102]

$$\sum_i \hat{e}_{ki} \hat{e}_{li} = \delta_{kl}, \tag{122}$$

where we have introduced the orthonormal basis vectors

$$\hat{e}_{ki} = \sqrt{\frac{q^{c_i}}{w_k}} e_{ki}. \tag{123}$$

Equation 122 implies the backward relation

$$\sum_k \hat{e}_{ki} \hat{e}_{kj} = \delta_{ij}, \tag{124}$$

or, in terms of unnormalized basis vectors,

$$\sum_k w_k^{-1} e_{ki} e_{kj} = \frac{1}{q^{c_i}} \delta_{ij}. \tag{125}$$

In the normalized basis the transformations between distribution and moments are

$$\hat{m}_k = \frac{m_k}{\sqrt{w_k}} = \sum_i \hat{e}_{ki} \frac{n_i}{\sqrt{q^{c_i}}} = \sum_i \hat{e}_{ki} \hat{n}_i, \tag{126}$$

$$\hat{n}_i = \frac{n_i}{\sqrt{q^{c_i}}} = \sum_k \hat{e}_{ki} \frac{m_k}{\sqrt{w_k}} = \sum_k \hat{e}_{ki} \hat{m}_k; \tag{127}$$

we will make use of these relations in Sec. 3.5. The analog of Eq. 104 for the normalized basis is

$$\hat{n}_i^{\star neq} = \sum_j \left(\delta_{ij} + \hat{\mathcal{L}}_{ij} \right) \hat{n}_j^{neq}, \tag{128}$$

with

$$\hat{\mathcal{L}}_{ij} = \sqrt{\frac{q^{c_j}}{q^{c_i}}} \mathcal{L}_{ij}. \tag{129}$$

In terms of unnormalized basis vectors the back transformation is given by

$$n_i = q^{c_i} \sum_k w_k^{-1} e_{ki} m_k. \tag{130}$$

The most obvious choice is to set $q^{c_i} = 1$ [110, 112], but then the basis vectors of the kinetic modes, $\mathbf{e}_{10} - \mathbf{e}_{18}$, are not orthogonal to the equilibrium distribution, and the moments $m_{10} - m_{18}$ have both equilibrium and non-equilibrium contributions [110, 112]. The statistical mechanical connection is more straightforward if the weights q^{c_i} are matched to the weights in the equilibrium distribution, setting $q^{c_i} = a^{c_i}$; this eliminates the projection of n_i^{eq} on the kinetic moments. The weighted orthogonality relation defines a different but equivalent set of basis vectors to those given in Refs. [110, 112], and these are the ones given in Table 1. A comparison of the two sets of basis vectors can be found in Ref. [114].

The basis vectors can be used to construct a collision operator that automatically satisfies all the lattice symmetries,

$$\hat{\mathcal{L}}_{ij} = \sum_k \lambda_k \hat{e}_{ki} \hat{e}_{kj}, \tag{131}$$

which is a symmetric matrix, while $\mathcal{L}_{ij}$, in general, is not symmetric. The orthogonality of the basis vectors ensures that each moment relaxes independently under the action of the linearized collision operator,

$$\hat{m}_k^{\star neq} = \gamma_k \hat{m}_k^{neq}, \tag{132}$$

where $\gamma_k = 1 + \lambda_k$. For the conserved modes $k = 0, \ldots, 3$ the value γ_k is immaterial, since $m_k^{\star neq} = m_k^{neq} = 0$. For the other modes, $k > 3$, linear stability requires that

$$|\gamma_k| \leq 1; \tag{133}$$

i.e. the effect of collisions must be to cause the nonequilibrium distribution to decrease rather than increase. The eigenvalues, γ_k, may be positive or negative, with $\gamma_k < 0$ corresponding to "over–relaxation".

The number of independent eigenvalues is limited by symmetry. There are at most six independent γ_k's in the D3Q19 model, corresponding to a bulk viscous mode with eigenvalue γ_v, five symmetry–related shear modes, which must have the same eigenvalue, γ_s, and nine kinetic modes, broken down into symmetry–related groups: $e_{10} - e_{12}$, $e_{13} - e_{15}$, e_{16}, $e_{17} - e_{18}$. The eigenvalues γ_s and γ_v can be related to the shear and bulk viscosities by decomposing the stress tensor into traceless–symmetric (shear) and trace (bulk) components,

$$\pi_{\alpha\beta} = \overline{\pi}_{\alpha\beta} + \frac{1}{3}\pi_{\gamma\gamma}\delta_{\alpha\beta}; \tag{134}$$

the overbar is used to denote a traceless tensor. Equation 132 implies the following relations between pre– and post–collisional stresses:

$$\overline{\pi}_{\alpha\beta}^{\star neq} = \gamma_s \overline{\pi}_{\alpha\beta}^{neq}, \tag{135}$$
$$\pi_{\alpha\alpha}^{\star neq} = \gamma_v \pi_{\alpha\alpha}^{neq}. \tag{136}$$

Additional relations between the pre– and post–collision stresses have already been provided (Eq. 100):

$$\overline{\pi}_{\alpha\beta}^{\star neq} - \overline{\pi}_{\alpha\beta}^{neq} = h\rho c_s^2 \left(\overline{\partial_\alpha u_\beta} + \overline{\partial_\beta u_\alpha} \right), \tag{137}$$

$$\pi_{\alpha\alpha}^{\star neq} - \pi_{\alpha\alpha}^{neq} = 2h\rho c_s^2 \partial_\alpha u_\alpha. \tag{138}$$

Equations 135–138 can be solved to relate the pre– and post–collision stresses to the velocity gradient:

$$\overline{\pi}_{\alpha\beta}^{neq} = -\frac{h\rho c_s^2}{1 - \gamma_s} \left(\overline{\partial_\alpha u_\beta} + \overline{\partial_\beta u_\alpha} \right), \tag{139}$$

$$\overline{\pi}_{\alpha\beta}^{\star neq} = -\frac{h\rho c_s^2 \gamma_s}{1 - \gamma_s} \left(\overline{\partial_\alpha u_\beta} + \overline{\partial_\beta u_\alpha} \right), \tag{140}$$

$$\pi_{\alpha\alpha}^{neq} = -\frac{2h\rho c_s^2}{1 - \gamma_v} \partial_\alpha u_\alpha, \tag{141}$$

$$\pi_{\alpha\alpha}^{\star neq} = -\frac{2h\rho c_s^2 \gamma_v}{1 - \gamma_v} \partial_\alpha u_\alpha. \tag{142}$$

From Eq. 75 we then find the usual Newtonian form for the viscous stress, and can identify the shear and bulk viscosities:

$$\eta = \frac{h\rho c_s^2}{2} \frac{1 + \gamma_s}{1 - \gamma_s}, \tag{143}$$

$$\eta_v = \frac{h\rho c_s^2}{3} \frac{1 + \gamma_v}{1 - \gamma_v}. \tag{144}$$

Lattice symmetry dictates that there are at most four independent eigenvalues of the kinetic modes: (see Table 1): γ_{3a} (modes $10-12$), γ_{3b} (modes $13-15$), γ_{4a} (mode 16), and γ_{4b} (modes $17-18$). In a number of implementations of the MRT model [99, 100, 106, 115] the kinetic eigenvalues are set to zero, so that these modes are projected out by the collision operator, although they reoccur at the next time step. Recently, it has been shown that the kinetic eigenvalues can be tuned to improve the accuracy of the boundary conditions at solid surfaces [113]. A useful simplification is to use only two independent relaxation rates, with $\gamma_v = \gamma_s = \gamma_{4a} = \gamma_{4b} = \gamma_e$ and $\gamma_{3a} = \gamma_{3b} = \gamma_o$. The optimal boundary conditions are obtained with specific relations between γ_e and γ_o [113, 114].

3.5
D3Q19 model III: Thermal noise

In the fluctuating LB model [98, 100], thermal noise is included by adding a stochastic contribution, Δ_i', to the collision operator:

$$\Delta_i = \sum_j \mathcal{L}_{ij} n_j^{neq} + \Delta_i'. \tag{145}$$

The collision operator must still conserve mass and momentum exactly,

$$\sum_i \Delta'_i = \sum_i \Delta'_i \mathbf{c}_i = 0, \tag{146}$$

while the statistical properties of Δ'_i include a vanishing mean, $\langle \Delta'_i \rangle = 0$, and a nontrivial covariance matrix, $\langle \Delta'_i \Delta'_j \rangle$, that gives the correct fluctuations at the hydrodynamic level (see Eqs. 44 and 47):

$$\left\langle \sigma^f_{\alpha\beta} \sigma^f_{\gamma\delta} \right\rangle = \frac{2k_B T}{b^3 h} \eta_{\alpha\beta\gamma\delta}. \tag{147}$$

The stochastic collision operator is assumed to be local in space and time, so that there are no correlations between the noise at different lattice sites or at different times. The delta functions in space and time have been replaced by b^{-3} and h^{-1}, respectively, so that the double integral of Eq. 47 with respect to $\mathbf{r}'$ and t', over a small space–time region of size $b^3 h$, matches the corresponding integral of Eq. 147.

Splitting the tensor into the trace, $\sigma^f_{\alpha\alpha}$, and traceless, $\bar{\sigma}^f_{\alpha\beta}$, parts gives the equivalent relations

$$\left\langle \bar{\sigma}^f_{\alpha\beta} \bar{\sigma}^f_{\gamma\delta} \right\rangle = \frac{2k_B T \eta}{b^3 h} \left[\delta_{\alpha\gamma} \delta_{\beta\delta} + \delta_{\alpha\delta} \delta_{\beta\gamma} - \frac{2}{3} \delta_{\alpha\beta} \delta_{\gamma\delta} \right], \tag{148}$$

$$\left\langle \sigma^f_{\alpha\alpha} \sigma^f_{\beta\beta} \right\rangle = \frac{18 k_B T \eta_v}{b^3 h}, \tag{149}$$

$$\left\langle \bar{\sigma}^f_{\alpha\beta} \sigma^f_{\gamma\gamma} \right\rangle = 0. \tag{150}$$

Although temperature does not appear directly in the D3Q19 LB model, we can determine the appropriate fluctuation level through the equation of state for an isothermal ideal gas of particles of mass m_p, $k_B T = m_p c_s^2 = \mu b^3 c_s^2$ [102]. Taking into account the results for η and η_v (Eqs. 143 and 144), we can write the desired correlations in terms of the LB variables:

$$\frac{\left\langle \bar{\sigma}^f_{\alpha\beta} \bar{\sigma}^f_{\gamma\delta} \right\rangle}{\mu\rho c_s^4} = \frac{1 + \gamma_s}{1 - \gamma_s} \left[\delta_{\alpha\gamma} \delta_{\beta\delta} + \delta_{\alpha\delta} \delta_{\beta\gamma} - \frac{2}{3} \delta_{\alpha\beta} \delta_{\gamma\delta} \right], \tag{151}$$

$$\frac{\left\langle \sigma^f_{\alpha\alpha} \sigma^f_{\beta\beta} \right\rangle}{\mu\rho c_s^4} = 6 \frac{1 + \gamma_v}{1 - \gamma_v}, \tag{152}$$

$$\left\langle \bar{\sigma}^f_{\alpha\beta} \sigma^f_{\gamma\gamma} \right\rangle = 0. \tag{153}$$

The stress fluctuations $\sigma^f_{\alpha\beta}$ are *different* from the random stresses $\sigma^r_{\alpha\beta}$ that arise in the LB algorithm itself,

$$\sigma^r_{\alpha\beta} = \sum_i \Delta'_i c_{i\alpha} c_{i\beta}. \tag{154}$$

The reason is that $\sigma^f_{\alpha\beta}$ pertains to fluctuations on the t_1 time scale, which interact with the hydrodynamic flow field, while $\sigma^r_{\alpha\beta}$ represents added noise on the lattice time scale, h. We use the Chapman–Enskog procedure to work backwards from the known fluctuations in $\sigma^f_{\alpha\beta}$ to determine the covariance matrix for $\sigma^r_{\alpha\beta}$ [102]. The stress update rule including random noise $\sigma^r_{\alpha\beta}$ is (*c.f.* Eqs. 135 and 136):

$$\bar{\pi}^{\star neq}_{\alpha\beta} = \gamma_s \bar{\pi}^{neq}_{\alpha\beta} + \bar{\sigma}^r_{\alpha\beta}, \tag{155}$$

$$\pi^{\star neq}_{\alpha\alpha} = \gamma_v \pi^{neq}_{\alpha\alpha} + \sigma^r_{\alpha\alpha}. \tag{156}$$

Eqs. 137 and 138 remain valid and, together with Eqs. 155 and 156, can be solved for the pre– and post–collisional stresses, $\pi^{neq}_{\alpha\beta}$ and $\pi^{\star neq}_{\alpha\beta}$, as before:

$$\bar{\pi}^{neq}_{\alpha\beta} = -\frac{h\rho c_s^2}{1 - \gamma_s} \left(\overline{\partial_\alpha u_\beta} + \overline{\partial_\beta u_\alpha} \right) + \frac{1}{1 - \gamma_s} \bar{\sigma}^r_{\alpha\beta}, \tag{157}$$

$$\bar{\pi}^{\star neq}_{\alpha\beta} = -\frac{h\rho c_s^2 \gamma_s}{1 - \gamma_s} \left(\overline{\partial_\alpha u_\beta} + \overline{\partial_\beta u_\alpha} \right) + \frac{1}{1 - \gamma_s} \bar{\sigma}^r_{\alpha\beta}, \tag{158}$$

$$\pi^{neq}_{\alpha\alpha} = -\frac{2h\rho c_s^2}{1 - \gamma_v} \partial_\alpha u_\alpha + \frac{1}{1 - \gamma_v} \sigma^r_{\alpha\alpha}, \tag{159}$$

$$\pi^{\star neq}_{\alpha\alpha} = -\frac{2h\rho c_s^2 \gamma_v}{1 - \gamma_v} \partial_\alpha u_\alpha + \frac{1}{1 - \gamma_v} \sigma^r_{\alpha\alpha}. \tag{160}$$

Comparing Eq. 75 with Eq. 44 we can read off the relations between the hydrodynamic fluctuations and the random noise,

$$\bar{\sigma}^f_{\alpha\beta} = -\frac{1}{1 - \gamma_s} \bar{\sigma}^r_{\alpha\beta}, \tag{161}$$

$$\sigma^f_{\alpha\alpha} = -\frac{1}{1 - \gamma_v} \sigma^r_{\alpha\alpha}. \tag{162}$$

Therefore, the random noise inserted at the microscopic (LB) level must have the following covariances:

$$\frac{\left\langle \bar{\sigma}^r_{\alpha\beta} \bar{\sigma}^r_{\gamma\delta} \right\rangle}{\mu\rho c_s^4} = \left(1 - \gamma_s^2\right) \left[\delta_{\alpha\gamma}\delta_{\beta\delta} + \delta_{\alpha\delta}\delta_{\beta\gamma} - \frac{2}{3}\delta_{\alpha\beta}\delta_{\gamma\delta} \right], \tag{163}$$

$$\frac{\left\langle \sigma^r_{\alpha\alpha} \sigma^r_{\beta\beta} \right\rangle}{\mu\rho c_s^4} = 6 \left(1 - \gamma_v^2\right), \tag{164}$$

$$\left\langle \bar{\sigma}^r_{\alpha\beta} \sigma^r_{\gamma\gamma} \right\rangle = 0. \tag{165}$$

The random stress has a typical amplitude of $\sqrt{\mu\rho} c_s^2$ and is obtained from the second–order moment of the fluctuations in n^{neq}_i. Therefore a typical fluctuation in the population density is of order $\sqrt{\mu\rho}$. Combining this scaling with Eqs. 126 and 127, suggests dimensionless variables

$$\hat{n}_i = \frac{n_i}{\sqrt{a^{c_i}\mu\rho}}, \tag{166}$$

$$\hat{m}_k = \frac{m_k}{\sqrt{w_k\mu\rho}}, \tag{167}$$

which transform using the symmetric basis vectors defined in Eq. 123,

$$\hat{m}_k = \sum_i \hat{e}_{ki}\hat{n}_i, \tag{168}$$

$$\hat{n}_i = \sum_k \hat{e}_{ki}\hat{m}_k. \tag{169}$$

The stochastic collision operator can then be implemented independently for each mode m_k,

$$\hat{m}_k^{\star neq} = \gamma_k \hat{m}_k^{neq} + \varphi_k r_k, \tag{170}$$

where r_k are independent Gaussian random variables with zero mean and unit variance. The dimensionless constants φ_k are determined by expressing the random stresses $\sigma_{\alpha\beta}^r$ in terms of the r_k and φ_k and then calculating the covariance matrix [102]. For example, $\sigma_{xy}^r = \sqrt{\mu\rho}c_s^2\varphi_7 r_7$, while $\sigma_{\alpha\alpha}^r = \sqrt{6\mu\rho}c_s^2\varphi_4 r_4$. Comparison with Eqs. 163 – 165 shows that the correct stress correlations are obtained for

$$\varphi_k = \left(1 - \gamma_k^2\right)^{1/2}. \tag{171}$$

At the hydrodynamic scale, only fluctuations in stress contribute to the time evolution of the momentum density (Eq. 44) so in principle it is sufficient to add random fluctuations to the modes $m_4, \ldots, m_9$ only: In the original derivation of the fluctuating LB equation [98, 100], the kinetic modes were projected out entirely, $i.e.$ $\gamma_k = \varphi_k = 0$ for $k = 10, 11, \ldots, 18$. More recently, Adhikari et $al.$ [101] have argued that the kinetic modes should be thermalized as well. They extended Eq. 170 to the kinetic modes ($k = 10, \ldots, 18$), with $\gamma_k = 0$ (as in Refs. [98, 100]) but with $\varphi_k = 1$, which then satisfies Eq. 171. It was demonstrated numerically that this leads to more accurate fluctuations at short length scales, but the theoretical justification remained somewhat obscure. From the discussion so far, we can see that both procedures give the same random stresses $\sigma_{\alpha\beta}^r$, and hence are not different from the point of view of fluctuating hydrodynamics. This has been clarified recently [102], by analyzing the LB model in terms of statistical mechanics. A purely microscopic approach was taken, in which the stochastic collisions were viewed as a Monte Carlo [116] process. Knowledge of the probability distribution of the LB variables $\mathbf{n}$ then makes it possible to check whether or not a given collision rule satisfies the condition of detailed balance. It can be shown [102] that the kinetic modes must be thermalized in order to satisfy detailed balance, in agreement with the procedure proposed in Ref. [101]. The theory will be outlined in Sec. 3.6.

3.6
Statistical mechanics of lattice-Boltzmann models

The starting point of the statistical mechanical development in Ref. [102] is the notion of a generalized lattice gas. We define $\nu_i(\mathbf{r}, t)$ in Eq. 30 as the *number* of particles with velocity $\mathbf{c}_i$ at site $\mathbf{r}$ at time t. In contrast with the standard LB model, ν_i is a (positive) integer; in contrast with lattice-gas models, $\nu_i \gg 1$. The state at a particular lattice site, $\boldsymbol{\nu}(\mathbf{r}, t)$, is modified by the collision process, subject to the constraints of mass and momentum conservation; the post–collision state, $\boldsymbol{\nu}^\star(\mathbf{r}, t)$, is then propagated to the neighboring sites (Eq. 30).

Although a deterministic GLG collision operator would be difficult to construct, we can nevertheless determine the distribution in a homogeneous equilibrium state from the conservation laws alone. First we note that there is an entropy associated with each ν_i,

$$S_i = - \left(\nu_i \ln \nu_i - \nu_i - \nu_i \ln \bar{\nu}_i + \bar{\nu}_i \right), \tag{172}$$

where $\bar{\nu}_i$ is the mean value of ν_i in the homogeneous state. Each velocity direction i at each lattice point has a degeneracy $\exp(S_i)$, which can be derived from a Bernoulli process. Particles are selected for the velocity direction i with probability p_0, with p_0 chosen so that on average a total of $\bar{\nu} = N_r p_0$ particles will be selected from a reservoir of N_r particles. Then the probability to select exactly ν particles is given by the binomial distribution,

$$p(\nu) = \frac{N_r!}{\nu! \left(N_r - \nu \right)!} \left(\frac{\bar{\nu}}{N_r} \right)^{\nu} \left(1 - \frac{\bar{\nu}}{N_r} \right)^{N_r - \nu}. \tag{173}$$

Equation 172 results from calculating $\ln p(\nu)$ in the limit of $N_r \to \infty$, at fixed $\bar{\nu}$. Under the usual assumption that in the equilibrium state the populations corresponding to different lattice sites and different directions are uncorrelated, the entropy per lattice site is $S(\boldsymbol{\nu}) = \sum_i S_i$.

The populations at a given lattice site are sampled from a probability distribution proportional to $\exp \left[S(\boldsymbol{\nu}) \right]$, but subject to the constraints of fixed mass and momentum density, which characterize the homogeneous state:

$$P(\boldsymbol{\nu}) \propto \exp \left[S(\boldsymbol{\nu}) \right] \delta \left(\mu \sum_i \nu_i - \rho \right) \delta \left(\mu \sum_i \nu_i \mathbf{c}_i - \mathbf{j} \right). \tag{174}$$

Consistency with the formalism developed in the previous sections requires

$$\mu \bar{\nu}_i = \rho a^{c_i}. \tag{175}$$

The equilibrium or mean populations for a given ρ and $\mathbf{j}$ are found by maximizing P or, more conveniently, by maximizing S and taking into account the conservation laws by Lagrange multipliers:

$$\frac{\partial S}{\partial \nu_i} + \lambda_\rho + \boldsymbol{\lambda}_{\mathbf{j}} \cdot \mathbf{c}_i = 0, \tag{176}$$

$$\mu \sum_i \nu_i - \rho = 0, \tag{177}$$

$$\mu \sum_i \nu_i \mathbf{c}_i - \mathbf{j} = 0. \tag{178}$$

The exact solution is

$$\nu_i^{eq} = \bar{\nu}_i \exp \left(\lambda_\rho + \boldsymbol{\lambda}_{\mathbf{j}} \cdot \mathbf{c}_i \right), \tag{179}$$

where the Lagrange multipliers, λ_ρ and $\boldsymbol{\lambda}_{\mathbf{j}}$, are found from the constraint equations 177 and 178. Solving these equations in terms of a power series in u, and disregarding terms of order $O(u^3)$, one finds the standard equilibrium distribution given in Eq. 97. This approach has been previously proposed within the framework of the "entropic lattice-Boltzmann" method [108, 109], which however, focuses exclusively on the deterministic LB model.

Within the statistical–mechanical framework we have developed for the LB model, the population densities n_i fluctuate around mean values determined by the

hydrodynamic flow fields. Thus the non-equilibrium distribution is sampled from $P(\mathbf{n}^{neq})$ which is Gaussian distributed about the equilibrium [102],

$$P\left(\mathbf{n}^{neq}\right) \propto \exp\left(-\sum_i \frac{(n_i^{neq})^2}{2\mu n_i^{eq}}\right) \delta\left(\sum_i n_i^{neq}\right) \delta\left(\sum_i \mathbf{c}_i\, n_i^{neq}\right). \qquad (180)$$

The variance of the fluctuations is controlled by the mass density μ, associated with an LB particle. A small number of particles gives rise to large fluctuations and *vice versa*. For simplicity we will ignore the effects of flow on the variance of the distribution, replacing n_i^{eq} by its $u = 0$ value. This can be justified at the macroscopic level by the Chapman-Enskog expansion [102]. Rewriting Eq. 180 in terms of normalized variables $\hat{n}_i$ (see Eq. 166), and transforming to the normalized modes (see Eqs. 167 and 169) eliminates the explicit constraints,

$$P\left(\hat{\mathbf{m}}^{neq}\right) \propto \exp\left(-\frac{1}{2}\sum_{k>3} \hat{m}_k^{neq\,2}\right). \qquad (181)$$

Fluctuations only arise in the non–conserved modes, while the conserved modes have no non-equilibrium contribution, *i.e.* $m_k^{neq} = 0$ for $k \leq 3$.

We now reinterpret the update rule Eq. 170,

$$\hat{m}_k^{\star neq} = \gamma_k \hat{m}_k^{neq} + \varphi_k r_k, \qquad (182)$$

as a Monte Carlo move. The transition probability is then identical to the probability of generating the random variable r_k,

$$\omega\left(\hat{m}_k^{neq} \rightarrow \hat{m}_k^{\star neq}\right) = \left(2\pi\varphi_k^2\right)^{-1/2} \exp\left[-\frac{\left(\hat{m}_k^{\star neq} - \gamma_k \hat{m}_k^{neq}\right)^2}{2\varphi_k^2}\right], \qquad (183)$$

and for the reverse transition the same formula holds, with the pre– and post–collisional populations exchanged. The condition of detailed balance [116],

$$\frac{\omega\left(\hat{m}_k^{neq} \rightarrow \hat{m}_k^{\star neq}\right)}{\omega\left(\hat{m}_k^{\star neq} \rightarrow \hat{m}_k^{neq}\right)} = \frac{\exp\left(-(\hat{m}_k^{\star neq})^2/2\right)}{\exp\left(-(\hat{m}^{neq})^2/2\right)}, \qquad (184)$$

then holds if and only if

$$\varphi_k = \left(1 - \gamma_k^2\right)^{1/2}, \qquad (185)$$

as before (Eq. 171). The important point is that this relation, which in the previous subsection was only proved for the stress modes, can now be shown to hold for *all* non–conserved modes. It is a necessary condition for consistent sampling of the thermal fluctuations, not just on the macroscopic hydrodynamic level (for which the stress modes alone are sufficient), but also on the microscopic LB level itself. Although assigning $\gamma_k = 0$ (and $\varphi_k = 1$) to all kinetic modes is obvious and straightforward [101], the present analysis shows that this is not necessary. Other values of γ_k and φ_k are possible as well, so long as they satisfy Eq. 185, and specific values may be desirable for a more accurate treatment of boundary conditions [113, 114].

3.7
External forces

An external force density $\mathbf{f}(\mathbf{r}, t)$ can be introduced into the LB algorithm by an additional collision operator Δ_i'',

$$\Delta_i = \sum_j \mathcal{L}_{ij} \left(n_j - n_j^{eq} \right) + \Delta_i''. \tag{186}$$

For simplicity, we only consider the deterministic case; the analysis of the fluctuating part (Δ_i') remains the same. Application of the new collision operator should leave the mass density unchanged, but increase the momentum density by $h\mathbf{f}$. This implies the following conditions on the moments of Δ_i'':

$$\sum_i \Delta_i'' = 0, \tag{187}$$

$$\sum_i \Delta_i'' \mathbf{c}_i = h\mathbf{f}. \tag{188}$$

Consequently the definition of the fluid velocity is no longer unique: one can legitimately choose any value for $\mathbf{u}$ between $\rho^{-1} \left(\sum_i n_i \mathbf{c}_i \right)$ and $\rho^{-1} \left(\sum_i n_i \mathbf{c}_i + h\mathbf{f} \right)$ (*i.e.* between the pre–collisional and post–collisional states). However, numerical [98] and theoretical [100, 117, 118] analysis shows that the optimum value is just the arithmetic mean of the pre– and post–collisional velocities. We *define* the momentum density as

$$\mathbf{j} = \sum_i n_i \mathbf{c}_i + \frac{h}{2} \mathbf{f}, \tag{189}$$

and the corresponding flow velocity as $\mathbf{u} = \mathbf{j}/\rho$. Consistency with Eq. 66 requires that we use this value for $\mathbf{u}$ to calculate n_i^{eq} (Eq. 97):

$$\sum_i n_i^{eq} \mathbf{c}_i = \mathbf{j}, \tag{190}$$

$$\sum_i n_i^{neq} \mathbf{c}_i = -\frac{h}{2} \mathbf{f}. \tag{191}$$

In Ref. [100] the usual moment condition $\sum_i n_i^{neq} \mathbf{c}_i = 0$ was maintained. In comparison with the present approach this makes a small error of order f^2 to the distribution, which leads to spurious terms in the Chapman-Enskog analysis. In contrast the present approach leads to a clean result, entirely equivalent to the force-free case. This may be of consequence when there are strongly inhomogeneous forces, such as are considered in Sec. 4. However, it should also be noted that these differences vanish in the low Reynolds number limit.

Since $\Delta_i''(\mathbf{n}^{eq}) \neq 0$, the Chapman–Enskog expansion of Δ_i'' starts at order ε^1 (*c.f.* Eq. 56):

$$\Delta_i'' = \varepsilon \Delta_i''^{(1)} + \varepsilon^2 \Delta_i''^{(2)} + \dots. \tag{192}$$

Following the procedure of Sec. 3.2, we take moments of Eqs. 57 and 59 and obtain similar equations for the mass and momentum density (*c.f.* Eqs. 74 and 75):

$$\partial_t \rho + \partial_\alpha j_\alpha = 0, \tag{193}$$

$$\partial_t j_\alpha + \partial_\beta \pi_{\alpha\beta}^{eq} + \frac{1}{2}\partial_\beta \left(\pi_{\alpha\beta}^{\star neq} + \pi_{\alpha\beta}^{neq} \right) = f_\alpha. \tag{194}$$

However, the second moment leads to a force-dependent contribution to the non-equilibrium momentum flux, which can be derived as before, beginning with Eq. 76 and substituting the equilibrium expressions for $\pi_{\alpha\beta}^{eq}$ (Eq. 79) and $\Phi_{\alpha\beta\gamma}^{eq}$ (Eq. 98). The time derivative of the momentum flux now generates terms involving $\mathbf{uf} + \mathbf{fu}$ from the momentum conservation equation on the t_1 time scale (*c.f.* Eq. 99):

$$\pi_{\alpha\beta}^{\star neq} - \pi_{\alpha\beta}^{neq} = h\rho c_s^2 \left(\partial_\alpha u_\beta + \partial_\beta u_\alpha \right) + h \left(u_\alpha f_\beta + u_\beta f_\alpha \right). \tag{195}$$

Spurious terms proportional to $\mathbf{uf}$ can be eliminated from Eq. 194, by including the second moment of Δ_i'',

$$\Sigma_{\alpha\beta} = \frac{1}{h} \sum_i \Delta_i'' c_{i\alpha} c_{i\beta}, \tag{196}$$

so that the stress update is now (*c.f.* Eq. 135 and 136)

$$\pi_{\alpha\beta}^{\star neq} = \gamma_s \bar{\pi}_{\alpha\beta}^{neq} + \frac{1}{3}\gamma_v \pi_{\gamma\gamma}^{neq} \delta_{\alpha\beta} + h\Sigma_{\alpha\beta}. \tag{197}$$

Equations 195 and 197 form a linear system for $\pi_{\alpha\beta}^{neq}$ and $\pi_{\alpha\beta}^{\star neq}$. Solving these equations as before (Eqs. 139 – 142), and inserting the result into Eq. 194, we obtain a Newtonian stress with unchanged values for the viscosities by choosing $\Sigma_{\alpha\beta}$ such that

$$\Sigma_{\alpha\beta} = \frac{1}{2}\left(1 + \gamma_s\right) \left[u_\alpha f_\beta + u_\beta f_\alpha - \frac{2}{3}u_\gamma f_\gamma \delta_{\alpha\beta} \right] + \frac{1}{3}\left(1 + \gamma_v\right) u_\gamma f_\gamma \delta_{\alpha\beta}. \tag{198}$$

The moment conditions expressed by Eqs. 187, 188 and 198 are uniquely satisfied by the choice

$$\Delta_i'' = a^{c_i} \left[\frac{h}{c_s^2} f_\alpha c_{i\alpha} + \frac{h}{2c_s^4} \Sigma_{\alpha\beta} \left(c_{i\alpha} c_{i\beta} - c_s^2 \delta_{\alpha\beta} \right) \right], \tag{199}$$

where Δ_i'' only affects the modes $m_1, \ldots, m_9$. This result has been derived previously [118] within the context of the LBGK model; here we have presented the derivation in the more general MRT framework.

4
Coupling the LB fluid to soft matter

The fundamental algorithmic problem in soft matter simulations is the coupling between the solid and fluid phases. A key attraction of LB methods is the simplicity with which geometrically complex boundaries can be incorporated. The first correct implementation of a moving boundary condition was described in the proceedings

of a workshop on lattice-gas cellular automata [119]; a more accessible source is Ref. [120]. The idea was to modify the bounce-back rule for stationary surfaces such that the steady-state distribution was consistent with the local surface velocity. By constructing the boundary-node interactions along the individual links, the viscous stress remains unchanged. Subsequently, we showed numerically that this algorithm gives accurate hydrodynamic interactions between spherical particles suspended in a lattice-gas fluid [120]. Nevertheless, it quickly became clear that the fluctuating LB model was a more useful computational tool, for the reasons outlined in Sec. 3. The LG algorithm for the moving boundary condition carries over in a simple and direct way to the LB method [98]. A number of improvements to the bounce-back boundary condition have been proposed over the years, and we will summarize some of the more practical approaches in Sec. 4.4.

More recently an entirely different approach has been proposed [121, 122] in which particles couple to the fluid through a frictional drag. This method has the advantage of greatly reducing the number of LB grid points in the simulation, at the cost of a representation that is only correct in the far field. The method has been applied to polymers [43, 122, 123] and to suspended solid particles [124–128]. In the latter case the surface is described by a number of sources distributed over the surface of the particle. The distributed forces resemble the Immersed Boundary (IB) methods [129], which are common in finite-difference and finite-element simulations; this connection has only been recognized recently [130]. We will summarize these developments and add some new ideas and interpretation of the force coupling methods. In a related development [131, 132], conventional immersed boundary methods are being used in conjunction with an LB fluid. However, the coupling in this case is implicit, solving for the velocity of the interface through a force balance, which corresponds to the high friction limit of Refs. [124–128]. Here, we will only consider inertial coupling, since the theory for thermal fluctuations has not been worked out for the implicit schemes.

4.1
Boundary conditions

To simulate the hydrodynamic interactions between solid particles in suspension, the lattice-Boltzmann model must be modified to incorporate the boundary conditions imposed on the fluid by the solid particles. The basic methodology is illustrated in Fig. 1. The solid particles are defined by a boundary surface, which can be of any size or shape; in Fig. 1 it is a circle. When placed on the lattice, the boundary surface cuts some of the links between lattice nodes. The fluid particles moving along these links interact with the solid surface at boundary nodes placed halfway along the links. Thus a discrete representation of the particle surface is obtained, which becomes more and more precise as the particle gets larger.

In early work, the lattice nodes on either side of the boundary surface were treated in an identical fashion [98, 120], so that fluid filled the whole volume of space, both inside and outside the solid particles. Although the fluid motion inside the particle closely follows that of a rigid solid body [99], at short times the inertial lag of the
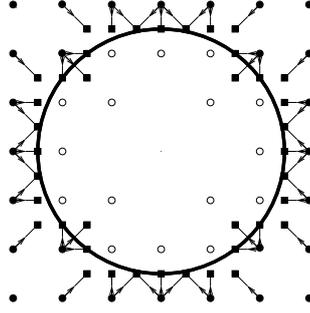
Fig. 1. Location of boundary nodes for a curved surface. The velocities along links cutting the boundary surface are indicated by arrows. The locations of the boundary nodes are shown by solid squares, and the fluid nodes by solid circles. The open circles indicate nodes in the solid adjacent to fluid nodes.

fluid is noticeable, and the contribution of the interior fluid to the particle force and torque reduces the stability of the particle velocity update. Today, most simulations exclude interior fluid, although the implementation is more difficult when the particles move. The moving boundary condition [98] without interior fluid [133] is then implemented as follows. We take the set of fluid nodes $\mathbf{r}$ just outside the particle surface, and for each node all the velocities $\mathbf{c}_b$ such that $\mathbf{r} + \mathbf{c}_b h$ lies inside the particle surface. An example of a set of boundary node velocities is shown by the arrows in Fig. 1. Each of the corresponding population densities is then updated according to a simple rule which takes into account the motion of the particle surface [98];

$$n_{b'}(\mathbf{r}, t + h) = n_b^*(\mathbf{r}, t) - \frac{2a^{c_b}\rho\mathbf{u}_b \cdot \mathbf{c}_b}{c_s^2}, \tag{200}$$

where $n_b^*(\mathbf{r}, t)$ is the post-collision distribution at $(\mathbf{r}, t)$ in the direction $\mathbf{c}_b$, and $\mathbf{c}_{b'} = -\mathbf{c}_b$. The local velocity of the particle surface,

$$\mathbf{u}_b = \mathbf{U} + \mathbf{\Omega} \times (\mathbf{r}_b - \mathbf{R}), \tag{201}$$

is determined by the particle velocity $\mathbf{U}$, angular velocity $\mathbf{\Omega}$, and center of mass $\mathbf{R}$; $\mathbf{r}_b = \mathbf{r} + \frac{1}{2}h\mathbf{c}_b$ is the location of the boundary node.

As a result of the boundary node updates, momentum is exchanged locally between the fluid and the solid particle, but the combined momentum of solid and fluid is conserved. The forces exerted at the boundary nodes can be calculated from the momentum transferred in Eq. 200, and the particle forces and torques are then obtained by summing over all the boundary nodes associated with a particular particle. It can be shown analytically that the force on a planar wall in a linear shear flow is exact [98], and several numerical examples of lattice-Boltzmann simulations of hydrodynamic interactions are given in Ref. [99]. Figure 2 illustrates the accuracy that can be achieved with the MRT collision operator described in Sec. 3.4. Even with small particles, only $5b$ in diameter, the hydrodynamic interactions are within 1% of a precise numerical solution [21], down to separations between the particle surfaces $s = r - 2a \sim b$, corresponding to $s \sim 0.4a$, where a is the sphere radius. Periodic
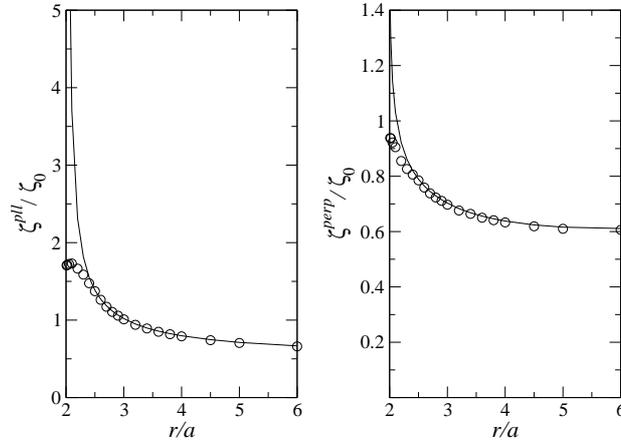
Fig. 2. Hydrodynamic interactions from LB simulations with particles of radius $a = 2.5b$. The solid symbols are the LB friction coefficients, ζ^{pll} and ζ^{perp}, for the relative motion of two spheres along the line of centers (left) and perpendicular to the line of centers (right). Results are compared with essentially exact results from a multipole code [21] in the same geometry (solid lines).

boundaries with a unit cell size $L = 12a$ were used, with the pair inclined at $30°$ to a symmetry axis; other geometries give a very similar level of agreement. We emphasize that there are no adjustable parameters in these comparisons. In particular, in contrast to previous work [99, 104], there is no need to calibrate the particle radius; the correct particle size arises automatically when the eigenvalues of the kinetic modes of the MRT model have the appropriate dependence on the shear viscosity [114].

To understand the physics of the moving boundary condition, one can imagine an ensemble of particles, moving at constant speed $\mathbf{c}_b$, impinging on a massive wall oriented perpendicular to the particle motion. The wall itself is moving with velocity $\mathbf{u}_b \ll \mathbf{c}_b$. The velocity of the particles after collision with the wall is $-\mathbf{c}_b + 2\mathbf{u}_b$ and the force exerted on the wall is proportional to $\mathbf{c}_b - \mathbf{u}_b$. Since the velocities in the lattice-Boltzmann model are discrete, the desired boundary condition cannot be implemented directly, but we can instead modify the density of returning particles so that the momentum transferred to the wall is the same as in the continuous velocity case. It can be seen that this implementation of the no-slip boundary condition leads to a small mass transfer across a moving solid-fluid interface. This is physically correct and arises from the discrete motion of the solid surface. Thus during a time step h the fluid is flowing continuously, while the solid particle is fixed in space. If the fluid cannot flow across the surface there will be large artificial pressure gra-

dients, arising from the compression and expansion of fluid near the surface. For a uniformly moving particle, it is straightforward to show that the mass transfer across the surface in a time step h (Eq. 200) is exactly recovered when the particle moves to its new position. For example, each fluid node adjacent to a planar wall has 5 links intersecting the wall. If the wall is advancing into the fluid with a velocity $\mathbf{U}$, then the mass flux across the interface (from Eq. 200) is $\rho\mathbf{U}$. Apart from small compressibility effects, this is exactly the rate at which fluid mass is absorbed by the moving wall. For sliding motion, Eq. 200 correctly predicts no net mass transfer across the interface.

4.2
Particle motion

An explicit update of the particle velocity

$$\mathbf{U}(t+h) = \mathbf{U}(t) + \frac{h}{m}\mathbf{F}(t) \tag{202}$$

has been found to be unstable [99] unless the particle radius is large or the particle mass density is much higher than the surrounding fluid. In previous work [99] the instability was reduced, but not eliminated, by averaging the forces and torques over two successive time steps. Subsequently, an implicit update of the particle velocity was proposed [134] as a means of ensuring stability. A generalized version of that idea, which can be adapted to situations where two particles are in near contact, was developed in Ref. [104]. Here we sketch an elaboration of this idea, which is consistent with a Trotter decomposition of the Liouville operator [135–139]. We will only consider the update of the position and linear velocity explicitly; the extension to rotational motion is straightforward [104].

The equations of motion for the suspended particles are written as

$$\dot{\mathbf{R}}_i = \mathbf{U}_i, \tag{203}$$

$$m\dot{\mathbf{U}}_i = \mathbf{F}_i^h(\mathbf{R}_i, \mathbf{U}_i) + \mathbf{F}_i^c(\mathbf{R}^N), \tag{204}$$

where we have separated the forces into a hydrodynamic component $\mathbf{F}_i^h$, which depends on the particle position and velocity, and a conservative force $\mathbf{F}_i^c$, which depends on the positions of all particles. The hydrodynamic force depends on the fluid degrees of freedom as well, but these remain unchanged during the particle update and need not be considered as dynamical variables here.

A second-order Trotter decomposition [135–139] breaks the update of a single time step into three independent components: a half time step update of the positions at constant velocity, a full time step update of the velocities with fixed positions, and a further half time step update of the positions using the new velocities:

$$\mathbf{R}_i(t + \tfrac{1}{2}h) = \mathbf{R}_i(t) + \frac{h}{2}\mathbf{U}_i(t), \tag{205}$$

$$\dot{\mathbf{U}}_i = \frac{1}{m}\left[\mathbf{F}_i^h(\mathbf{R}_i(t + \tfrac{1}{2}h), \mathbf{U}_i) + \mathbf{F}_i^c(\mathbf{R}^N(t + \tfrac{1}{2}h))\right], \tag{206}$$

$$\mathbf{R}_i(t + h) = \mathbf{R}_i(t + \tfrac{1}{2}h) + \frac{h}{2}\mathbf{U}_i(t + h). \tag{207}$$

In the absence of velocity-dependent forces this is just the Verlet scheme, but the solid-fluid boundary conditions (Eq. 200) introduce a hydrodynamic force that depends linearly on the particle velocity [104, 134],

$$\mathbf{F}_i^h(\mathbf{R}_i, \mathbf{U}_i) = \mathbf{F}_0^h(\mathbf{R}_i) - \boldsymbol{\zeta}(\mathbf{R}_i) \cdot \mathbf{U}_i. \tag{208}$$

The velocity independent force is calculated at the half-time step

$$\mathbf{F}_0^h(\mathbf{R}_i(t + \tfrac{1}{2}h)) = \frac{b^3}{h} \sum_b 2n_b^*(\mathbf{r}, t)\mathbf{c}_b, \tag{209}$$

where the sum is over all the boundary nodes, b, describing the particle surface and $\mathbf{c}_b$ points towards the particle center. The location of the boundary nodes is determined by the particle coordinates $\mathbf{R}_i(t + \tfrac{1}{2}h)$, which should be evaluated at the half time step as indicated. The post-collision populations, $n_b^\star$, are calculated at time t but arrive at the boundary nodes at the half time step also. The components of the matrix

$$\boldsymbol{\zeta}(\mathbf{R}_i(t + \tfrac{1}{2}h)) = \frac{2\rho b^3}{c_s^2 h} \sum_b a^{c_b} \mathbf{c}_b \mathbf{c}_b \tag{210}$$

are high-frequency friction coefficients, which describe the instantaneous force on a particle in response to a sudden change in velocity. Complete expressions, including rotation, are given in Ref. [104].

The LB fluid and the solid particles are coupled by an instantaneous momentum transfer at the half time step, which is therefore presumed to be conservative:

$$\mathbf{U}_i(t + \tfrac{1}{2}h) = \mathbf{U}_i(t) + \frac{h}{2m}\mathbf{F}_i^c(\mathbf{R}^N(t + \tfrac{1}{2}h)), \tag{211}$$

$$\mathbf{U}_i^\star(t + \tfrac{1}{2}h) = \mathbf{U}_i(t + \tfrac{1}{2}h) + \frac{h}{m}\mathbf{F}_i^h(\mathbf{R}_i(t + \tfrac{1}{2}h), \tilde{\mathbf{U}}_i(t + \tfrac{1}{2}h)), \tag{212}$$

$$\mathbf{U}_i(t + h) = \mathbf{U}_i^\star(t + \tfrac{1}{2}h) + \frac{h}{2m}\mathbf{F}_i^c(\mathbf{R}^N(t + \tfrac{1}{2}h)). \tag{213}$$

However it is not entirely clear what velocity should be used in Eq. 212: among the possibilities discussed in Ref. [104] are an explicit update $\tilde{\mathbf{U}}_i(t + \tfrac{1}{2}h) = \mathbf{U}_i(t + \tfrac{1}{2}h)$, an implicit update $\tilde{\mathbf{U}}_i(t + \tfrac{1}{2}h) = \mathbf{U}_i^\star(t + \tfrac{1}{2}h)$, and a semi-implicit update $\tilde{\mathbf{U}}_i(t + \tfrac{1}{2}h) = [\mathbf{U}_i(t + \tfrac{1}{2}h) + \mathbf{U}_i^\star(t + \tfrac{1}{2}h)]/2$. It has been pointed out [140] that, even for a Langevin equation with constant friction, there are deviations in the temperature for finite values of h. However the semi-implicit scheme satisfies the FDT exactly for constant friction. Here we will consider a different model for the velocity, assuming that the hydrodynamic force is distributed over the time step. For simplicity we consider a single component of the velocity,

$$m\dot{U} = -\zeta U + F_0^h + F^c, \tag{214}$$

where ζ, F_0^h and F^c are constant in this context. The solution of Eq. 214 over a time interval h is

$$U(t + h) = U(t) \exp(-\alpha) + \frac{F_0^h + F^c}{\zeta} \left[1 - \exp(-\alpha)\right], \tag{215}$$

where $\alpha = \zeta h/m$ is the dimensionless time step. Equation 215 is stable for all values of α, satisfies the FDT exactly, and, when there is no conservative force, encompasses previous algorithms as limiting cases. Both explicit [98] and implicit [104, 134] schemes are consistent with an expansion of Eq. 215 to linear order in α, while the semi-implicit method [104] can be derived from a second order expansion in α. The steady-state velocity $U(t + h) = U(t)$ satisfies the force balance $F^h + F^c = 0$ exactly. This new result may lead to more accurate integration of the particle positions and velocities in the large α limit.

To complete the update, the velocity $\tilde{U}_i(t + \frac{1}{2}h)$ is needed to calculate the momentum transfer to the fluid (Eq. 200). An explicit update [98] can be done in a single pass since $\tilde{U}_i(t + \frac{1}{2}h) = U_i(t)$ is already known, but an implicit or semi-implicit update requires two passes through the boundary nodes. The first pass is used to calculate F_0^h so that Eq. 212 can be solved for $\tilde{U}_i(t + \frac{1}{2}h)$ [104]. This velocity is used to update the population densities in a second sweep through the boundary nodes. In the present case we calculate $\tilde{U}_i(t + \frac{1}{2}h)$ by enforcing consistency between the sequential update Eqs. 211–213 and Eq. 215:

$$\alpha\tilde{U}_i(t+\tfrac{1}{2}h) = U_i(t)\left[1 - \exp(-\alpha)\right] + \left(F_0^h + F^c\right)\left(\frac{\alpha}{\zeta} - \frac{1 - \exp(-\alpha)}{\zeta}\right). \quad (216)$$

This ensures overall momentum conservation as before.

When there are short-range conservative forces between the particles, the LB time step is frequently too large for accurate integration of the interparticle forces. The LB time step can be divided into an integer number of substeps, but the question then arises as to how to best incorporate the hydrodynamic forces, since F^h should, in principle, be calculated at $t + \frac{1}{2}h$. One possibility is to use the fact that ζ varies slowly with particle position and accept the small error associated with using $R(t)$ rather than $R(t + \frac{1}{2}h)$. Or this solution could be used as a predictor step for calculating $R(t + \frac{1}{2}h)$, which could then be followed by one or more corrector cycles with increasingly more accurate calculations of $\zeta(t + \frac{1}{2}h)$. The corrector cycles should not involve a significant overhead since the boundary nodes would be largely the same from one cycle to the next, and the time-consuming lookup of LB population densities could be avoided.

Although the momentum exchange between fluid and solid occurs instantaneously at the half time step, in calculating $\tilde{U}_i(t+\frac{1}{2}h)$ we have made the assumption that the hydrodynamic force is distributed over the time step. We actually attempted to derive an update for the velocity assuming that the hydrodynamic force acts over a very small fraction of the time step, but this has not lead to a sensible result as yet. It is not entirely clear if the assumption that the hydrodynamic force acts over the whole time step is valid, and does not, for example, produce an artificial dissipation. To resolve this question will require a detailed analysis of the fully coupled system, along the lines given in Sec. 4.5 for the simpler case of frictional coupling. A similar analysis for solid-fluid boundary conditions is an open area for further research.

4.3
Surfaces near contact

When two particle surfaces come within one grid spacing, fluid nodes are excluded
from regions between the solid surfaces, leading to a loss of mass conservation. This
happens because boundary updates at each link cause mass transfer across the solid-
fluid interface, which is necessary to accommodate the discrete motion of the particle
surface (see Sec. 4.1). The total mass transfer in or out of an isolated particle is

$$\Delta M = -\frac{2h^3\rho}{c_s^2}\left[\mathbf{U}\cdot\sum_b a^{c_b}\mathbf{c}_b\right] = 0, \tag{217}$$

regardless of the particle's size or shape.

Although the sum $\sum_b a^{c_b}\mathbf{c}_b$ is zero for any closed surface [104], when two parti-
cles are close to contact some of the boundary nodes are missing and the surfaces are
no longer closed. In this case $\Delta M \neq 0$ and mass conservation is no longer ensured.
Two particles that remain in close proximity never reach a steady state, no matter
how slowly they move, since fluid is constantly being added or removed, depending
on the particle positions and velocities. If the two particles move as a rigid body mass
conservation is restored, but in general this is not the case. The accumulation or loss
of mass occurs slowly, and in many dynamical simulations it fluctuates with changing
particle configuration but shows no long-term drift. However, we typically enforce
mass conservation, particle-by-particle, by redistributing the excess mass among the
boundary nodes [104]. An alternative idea is to ensure that there is always at least
one fluid node in the gap between the particle surfaces. In dense suspensions it would
be quite inaccurate to insert an artificial excluded volume around the particles, but a
more promising idea is to cut back the particle surfaces along planes perpendicular to
the line of centers [141, 142]. It remains to be seen if the hydrodynamic interactions
retain the level of accuracy shown in Fig. 2.

When two particles are in near contact, the fluid flow in the gap cannot be re-
solved. For particle sizes that are typically used in multiparticle simulations ($a < 5b$),
the lubrication breakdown in the calculation of the hydrodynamic interaction occurs
at gaps of the order of $0.1a$. However, in some flows, notably the shearing of a dense
suspension, qualitatively important physics occurs at smaller separations, typically
down to $0.01a$. Here we outline a method to implement lubrication corrections into
a lattice-Boltzmann simulation.

For particles close to contact, the lubrication force, torque, and stresslet can be
calculated from a sum of pairwise-additive contributions [29], and if we consider
only singular terms, they can be calculated from the particle velocities alone [143].
In lattice-Boltzmann simulations [100, 144] the calculated forces follow the Stokes
flow results down to a fixed separation, approximately equal to the grid spacing b, and
remain roughly constant thereafter (see Fig. 2). The simplest lubrication correction
is to take the difference between the lubrication force at a gap s and the force at some
cut off distance s_c; *i.e.*

$$\mathbf{F}^l = -6\pi\eta\frac{a_1^2 a_2^2}{(a_1+a_2)^2}\left(\frac{1}{s}-\frac{1}{s_c}\right)\mathbf{U}_{12}\cdot\hat{\mathbf{R}}_{12}\hat{\mathbf{R}}_{12} \quad s < s_c \tag{218}$$

$$\mathbf{F}^l = 0 \quad s > s_c, \tag{219}$$

where $\mathbf{U}_{12} = \mathbf{U}_1 - \mathbf{U}_2$, $s = |\mathbf{R}_{12}| - a_1 - a_2$ is the gap between the two surfaces, and the unit vector $\hat{\mathbf{R}}_{12} = \mathbf{R}_{12}/|\mathbf{R}_{12}|$. Numerical tests of this procedure for the older 10-moment LB model are reported in Ref. [104]. Results for the MRT model are shown in Fig. 3, using a cutoff distance $s_c = 1.1b$ for the parallel component and $s_c = 0.7b$ for the perpendicular component. Even this simple form for the correction gives an accurate description of the lubrication regime, with the largest deviations occurring near the patch points. A more accurate correction can be obtained by calibrating each distance separately as in Stokesian dynamics and related methods [21, 145].
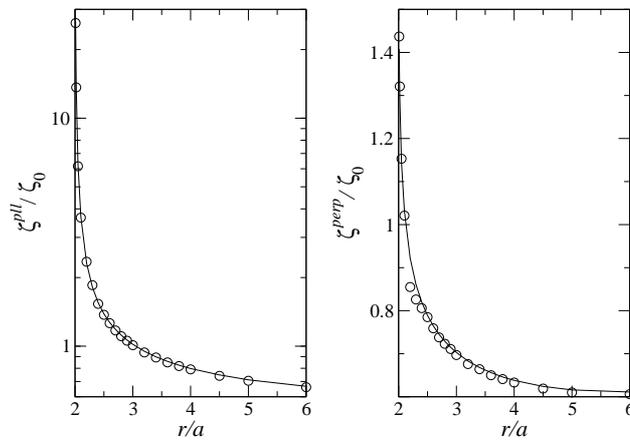
Fig. 3. Hydrodynamic interactions including lubrication, with particles of radius $a = 2.5b$. The solid symbols are the LB friction coefficients, ζ^{pll} and ζ^{perp}, for the relative motion of two spheres along the line of centers (left) and perpendicular to the line of centers (right). Results are compared with essentially exact results from a multipole code [21] in the same geometry (solid lines).

4.4
Improvements to the bounce-back boundary condition

The bounce-back boundary condition remains the most popular choice for simulations of suspensions, because of its robustness and simplicity. The results in Figs. 2 and 3 show that accurate hydrodynamic interactions, within 1–2%, can be achieved with quite small particles, particularly when combined with the MRT model. The reason that bounce-back works so well, despite being only first-order accurate, is

that the errors in the momentum transfer tend to cancel when averaged over a random sampling of boundary node positions [114]. In fact bounce-back can sometimes be more accurate than interpolation, where the errors, though locally smaller, do not cancel.
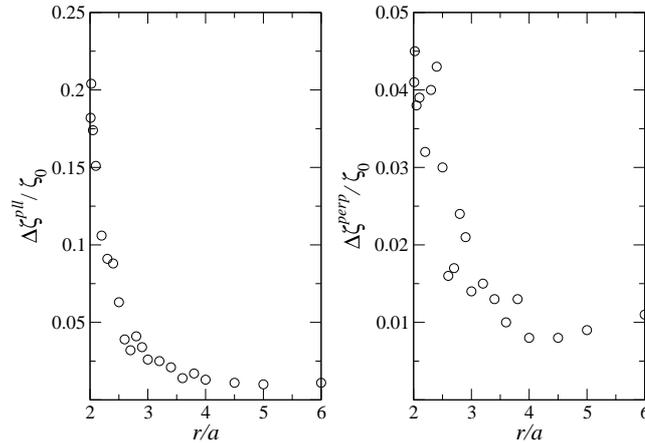

Fig. 4. Variation in friction coefficients with grid location for particles of radius $a = 2.5b$. The solid symbols are the variance in the LB friction coefficients, $\Delta\zeta^{pll}$ and $\Delta\zeta^{perp}$ for the relative motion of two spheres along the line of centers (left) and perpendicular to the line of centers (right). Results are a single standard deviation in the friction coefficients, calculated from 100 independent positions with respect to the grid.

The most important deficiency of the bounce-back algorithm is the dependence of the force on the position of the nodes with respect to the grid. The results in Figs. 2 and 3 are averages over 100 independent configurations, in which the relative positions of the particles are the same but the pair is displaced randomly with respect to the underlying lattice. However, the variance in the friction for randomly sampled grid locations is small, typically of the order of 1%, as can be seen in Fig. 4. Nevertheless there is a much larger fluctuation in the force around the particle surface, which is particularly problematic if the particles are deformable [146, 147]. Thus while the bounce-back method is quite accurate on average, locally the errors can be large. A detailed analytical and numerical critique of the bounce-back algorithm can be found in Ref. [148], together with an analysis of several of the modifications mentioned below. The most practical higher-order boundary conditions are adapted from the link bounce-back algorithm outlined in Sec. 4.1.

More sophisticated boundary conditions have been developed using finite-volume methods [149, 150] and interpolation [151–153]. A simple, physically motivated in-

terpolation scheme has been proposed [151, 154], which both improves the accuracy of the bounce-back rule and is unconditionally stable for all boundary positions; the scheme has both linear and quadratic versions. A more general framework for this class of interpolation schemes has been extensively analyzed in a comprehensive and seminal paper [113]; the Multi-Reflection Rule proposed in Ref. [113] is the most accurate boundary condition yet discovered for lattice-Boltzmann methods. However interpolation requires additional fluid nodes in the gap between adjacent particle surfaces. The bounce-back rule requires only one grid point between the surfaces but linear interpolation requires at least two grid points, while quadratic interpolation and multi-reflection require three. Recently, it was proposed that only the equilibrium distribution needs to be interpolated [114]. Although this is more complex to implement than linear interpolation, it has the advantage that the velocity distribution at the boundary surface may be used to provide an additional interpolation point. In this way the span of fluid nodes can be reduced to that of the bounce-back rule, while obtaining second-order accuracy in the flow field. In conjunction with an appropriate choice of collision operator [113], the location of the hydrodynamic boundary remains independent of fluid viscosity, unlike the linear and quadratic interpolations [151]. For viscous fluids, where $\gamma_s > 0$, the equilibrium interpolation rule is more accurate than either linear or quadratic interpolation [114].

4.5
Force coupling

The force-coupling algorithm [121, 122] starts from a system of mass points which are coupled *dissipatively* to the hydrodynamic continuum. The particles are specified by positions $\mathbf{r}_i$, momenta $\mathbf{p}_i$, masses m_i, and phenomenological friction coefficients Γ_i. They interact via a potential $V\left(\mathbf{r}^N\right)$, giving rise to conservative forces $\mathbf{F}_i^c = -\partial V/\partial \mathbf{r}_i$. The fluid exerts a drag force on each particle based on the difference between the particle velocity and the fluid velocity $\mathbf{u}_i = \mathbf{u}(\mathbf{r}_i)$,

$$\mathbf{F}_i^d = -\Gamma_i \left(\frac{\mathbf{p}_i}{m_i} - \mathbf{u}_i \right). \tag{220}$$

Momentum conservation requires that an equal and opposite force be applied to the fluid. Both discrete and continuous degrees of freedom are subject to Langevin noise in order to balance the frictional and viscous losses, and thereby keep the temperature constant. The algorithm can be applied to any Navier–Stokes solver, not just to LB models. For this reason, we will discuss the coupling within a (continuum) Navier–Stokes framework, with a general equation of state $p(\rho)$. We use the abbreviations $\eta_{\alpha\beta\gamma\delta}$ for the viscosity tensor (Eq. 46), and

$$\pi_{\alpha\beta}^E = p\delta_{\alpha\beta} + \rho u_\alpha u_\beta \tag{221}$$

for the inviscid momentum flux or Euler stress (Eq. 79). Since the fluid equations are solved on a grid, whereas the particles move continuously, it will be necessary to *interpolate* the flow field from nearby lattice sites to the particle positions [122].

The addition of a point force into the continuum fluid equations introduces a singularity into the flow field, which causes both mathematical and numerical difficulties. On the other hand, the flow field around a finite-sized particle can be generated by a distributed force located entirely inside the particle [155, 156]. This flow field is everywhere finite, and the force density appearing in Eq. 17 can be written as

$$\mathbf{f}(\mathbf{r}) = -\sum_i \mathbf{F}_i^d \Delta(\mathbf{r}, \mathbf{r}_i), \tag{222}$$

where $\Delta(\mathbf{r})$ is a weight function with compact support and normalization

$$\int d^3\mathbf{r}\,\Delta(\mathbf{r}, \mathbf{r}_i) = 1. \tag{223}$$

Compact support limits the set of nodes $\mathbf{r}$ to those in the vicinity of $\mathbf{r}_i$ and ensures that the interactions remain local. Away from solid boundaries, translational invariance requires that

$$\Delta(\mathbf{r}, \mathbf{r}_i) = \Delta(\mathbf{r} - \mathbf{r}_i). \tag{224}$$

The function $\Delta(\mathbf{r}, \mathbf{r}_i)$ plays a dual role, both interpolating the fluid velocity field to the particle position,

$$\mathbf{u}(\mathbf{r}_i) = \int d^3\mathbf{r}\,\Delta(\mathbf{r}, \mathbf{r}_i)\mathbf{u}(\mathbf{r}), \tag{225}$$

and then redistributing the reactive force to the fluid, according to Eq. 222. Within the context of polymer simulations, Δ has been regarded as an interpolating function for point forces, but it can equally well be regarded as a model for a specific distributed force, contained within an envelope described by $\Delta(\mathbf{r} - \mathbf{r}_i)$. The flow fields from a point force and a distributed force are similar at large distances from the source, but the distributed source has the advantage that the near field also corresponds to a physical system, namely finite-size particles. We will adopt the distributed source interpretation both here and in Sec. 4.6.

The Langevin equations of motion for the coupled fluid–particle system are:

$$\frac{d}{dt}\mathbf{r}_i = \frac{1}{m_i}\mathbf{p}_i, \tag{226}$$

$$\frac{d}{dt}\mathbf{p}_i = \mathbf{F}_i^c + \mathbf{F}_i^d + \mathbf{F}_i^f, \tag{227}$$

$$\partial_t \rho + \partial_\alpha j_\alpha = 0, \tag{228}$$

$$\partial_t j_\alpha + \partial_\beta \pi_{\alpha\beta}^E = \partial_\beta \eta_{\alpha\beta\gamma\delta} \partial_\gamma u_\delta + f_\alpha^h + \partial_\beta \sigma_{\alpha\beta}^f, \tag{229}$$

where the force density applied to the fluid includes both dissipative and random forces,

$$\mathbf{f}^h(\mathbf{r}) = -\sum_i \left(\mathbf{F}_i^d + \mathbf{F}_i^f \right) \Delta(\mathbf{r}, \mathbf{r}_i). \tag{230}$$

The Langevin noises for the particles and fluid, $\mathbf{F}_i^f$ and $\sigma_{\alpha\beta}^f$, satisfy the usual moment conditions:

$$\left\langle F_{i\alpha}^{f} \right\rangle = 0, \tag{231}$$

$$\left\langle \sigma_{\alpha\beta}^{f} \right\rangle = 0, \tag{232}$$

$$\left\langle F_{i\alpha}^{f}(t) F_{j\beta}^{f}(t') \right\rangle = 2k_B T \Gamma_i \delta_{ij} \delta_{\alpha\beta} \delta(t - t'), \tag{233}$$

$$\left\langle \sigma_{\alpha\beta}^{f}(\mathbf{r}, t) \sigma_{\gamma\delta}^{f}(\mathbf{r}', t') \right\rangle = 2k_B T \eta_{\alpha\beta\gamma\delta} \delta(\mathbf{r} - \mathbf{r}') \delta(t - t'). \tag{234}$$

By construction, this coupling is local, and conserves both the total mass

$$M = \sum_i m_i + \int d^3\mathbf{r} \rho \tag{235}$$

and the total momentum

$$\mathbf{P} = \sum_i \mathbf{p}_i + \int d^3\mathbf{r} \rho \mathbf{u}. \tag{236}$$

Galilean invariance is ensured by using velocity differences in the coupling between particles and fluid (Eq. 220). A finer point is that the interpolation uses $\mathbf{u}$ (and not $\mathbf{j}$), so that the velocity field enters strictly linearly. We will prove that the fluctuation–dissipation theorem (FDT) holds for this coupled system, proceeding in three steps that successively take more terms into account.

Let us look first at the conservative system where the particles and fluid are completely decoupled:

$$\frac{d}{dt}\mathbf{r}_i = \frac{1}{m_i}\mathbf{p}_i, \tag{237}$$

$$\frac{d}{dt}\mathbf{p}_i = \mathbf{F}_i^c, \tag{238}$$

$$\partial_t \rho + \partial_\alpha j_\alpha = 0, \tag{239}$$

$$\partial_t j_\alpha + \partial_\beta \pi_{\alpha\beta}^E = 0. \tag{240}$$

The dynamics of the particles *and* the Euler fluid can be described within the framework of Hamiltonian mechanics [157]. The Hamiltonians for the particles

$$\mathcal{H}_p = \sum_i \frac{\mathbf{p}_i^2}{2m_i} + V, \tag{241}$$

and fluid,

$$\mathcal{H}_f = \int d^3\mathbf{r} \left(\frac{1}{2}\rho\mathbf{u}^2 + \epsilon(\rho) \right), \tag{242}$$

are conserved quantities, with $\epsilon(\rho)$ the internal energy density of the fluid.

As a second step, we consider a system where particles and fluid are still decoupled, but are subject to dissipation and noise:

$$\frac{d}{dt}\mathbf{r}_i = \frac{1}{m_i}\mathbf{p}_i, \tag{243}$$

$$\frac{d}{dt}\mathbf{p}_i = \mathbf{F}_i^c - \frac{\Gamma_i}{m_i}\mathbf{p}_i + \mathbf{F}_i^f, \tag{244}$$

$$\partial_t \rho + \partial_\alpha j_\alpha = 0, \tag{245}$$

$$\partial_t j_\alpha + \partial_\beta \pi_{\alpha\beta}^E = \partial_\beta \eta_{\alpha\beta\gamma\delta}\partial_\gamma u_\delta + \partial_\beta \sigma_{\alpha\beta}^f. \tag{246}$$

These Langevin equations are known to satisfy the FDT [15, 42, 158–160]. We briefly sketch the formalism used for the proof, since this will be needed for the final step in which we consider the fully coupled system.

Instead of describing the stochastic dynamics via a Langevin equation, we use the Fokker–Planck equation, which is the evolution equation for the probability density in phase space. For an N-particle system,

$$\partial_t P\left(\mathbf{r}^N, \mathbf{p}^N\right) = (\mathcal{L}_1 + \mathcal{L}_2 + \mathcal{L}_3) P\left(\mathbf{r}^N, \mathbf{p}^N\right), \tag{247}$$

where $\mathbf{r}^N, \mathbf{p}^N$ denote the positions and momenta of all N particles. The three operators $\mathcal{L}_1$, $\mathcal{L}_2$, and $\mathcal{L}_3$ describe the Hamiltonian, frictional, and stochastic part of the dynamics; they can be found via the Kramers–Moyal expansion [15, 159]:

$$\mathcal{L}_1 = -\sum_i \left(\frac{\partial}{\partial \mathbf{r}_i} \cdot \frac{\mathbf{p}_i}{m_i} + \frac{\partial}{\partial \mathbf{p}_i} \cdot \mathbf{F}_i^c\right), \tag{248}$$

$$\mathcal{L}_2 = \sum_i \frac{\Gamma_i}{m_i}\frac{\partial}{\partial \mathbf{p}_i} \cdot \mathbf{p}_i, \tag{249}$$

$$\mathcal{L}_3 = k_B T \sum_i \Gamma_i \frac{\partial^2}{\partial \mathbf{p}_i^2}. \tag{250}$$

The FDT holds if the Boltzmann factor, $\exp\left(-\mathcal{H}_p/k_B T\right)$, is a stationary solution of the Fokker–Planck equation. Using $\beta = (k_B T)^{-1}$ to define the inverse temperature, we have

$$\mathcal{L}_1 \exp\left(-\beta \mathcal{H}_p\right) = 0 \tag{251}$$

as a direct consequence of energy conservation in Hamiltonian systems. Furthermore, the relation

$$(\mathcal{L}_2 + \mathcal{L}_3)\exp\left(-\beta \mathcal{H}_p\right) = 0 \tag{252}$$

can be shown by direct differentiation.

For the fluid system, the phase space comprises all possible configurations of the fields $\rho(\mathbf{r})$, $\mathbf{j}(\mathbf{r})$, which we denote as $[\rho]$, $[\mathbf{j}]$. The Fokker-Planck equation for the fluid degrees of freedom can be written as

$$\partial_t P\left([\rho], [\mathbf{j}]\right) = (\mathcal{L}_4 + \mathcal{L}_5 + \mathcal{L}_6) P\left([\rho], [\mathbf{j}]\right), \tag{253}$$

where $\mathcal{L}_4$, $\mathcal{L}_5$, and $\mathcal{L}_6$ describe the Hamiltonian, viscous, and stochastic components,

$$\mathcal{L}_4 = \int d^3\mathbf{r}\left(\frac{\delta}{\delta\rho}\partial_\alpha j_\alpha + \frac{\delta}{\delta j_\alpha}\partial_\beta \pi_{\alpha\beta}^E\right), \tag{254}$$

$$\mathcal{L}_5 = -\eta_{\alpha\beta\gamma\delta}\int d^3\mathbf{r}\frac{\delta}{\delta j_\alpha}\partial_\beta\partial_\gamma u_\delta, \tag{255}$$

$$\mathcal{L}_6 = k_B T \eta_{\alpha\beta\gamma\delta}\int d^3\mathbf{r}\int d^3\mathbf{r}'\frac{\delta}{\delta j_\alpha(\mathbf{r})}\frac{\delta}{\delta j_\gamma(\mathbf{r}')}\left[\frac{\partial}{\partial r_\beta}\frac{\partial}{\partial r_\delta'}\delta\left(\mathbf{r} - \mathbf{r}'\right)\right], \tag{256}$$

and $\delta\dots/\delta\dots$ represents a functional derivative [161]. Replacing $\partial/\partial r_\delta'$ in the last equation with $-\partial/\partial r_\delta$ enables integration over $\mathbf{r}'$:

$$\mathcal{L}_6 = -k_B T \eta_{\alpha\beta\gamma\delta} \int d^3\mathbf{r} \frac{\delta}{\delta j_\alpha} \partial_\beta \partial_\gamma \frac{\delta}{\delta j_\delta}, \tag{257}$$

where we have exploited the symmetry of the viscosity tensor with respect to the indexes γ and δ. Functional differentiation of the Boltzmann factor with respect to $\mathbf{j}$,

$$\frac{\delta}{\delta j_\delta} \exp\left(-\beta\mathcal{H}_f\right) = -\beta u_\delta \exp\left(-\beta\mathcal{H}_f\right), \tag{258}$$

then shows that

$$(\mathcal{L}_5 + \mathcal{L}_6) \exp\left(-\beta\mathcal{H}_f\right) = 0. \tag{259}$$

Finally, the relation

$$\mathcal{L}_4 \exp\left(-\beta\mathcal{H}_f\right) = 0 \tag{260}$$

follows from energy conservation in Hamiltonian dynamics.

We now turn to the coupled system, with Hamiltonian $\mathcal{H} = \mathcal{H}_p + \mathcal{H}_f$. The Fokker–Planck equation in the full phase space reads

$$\partial_t P\left(\mathbf{r}^N, \mathbf{p}^N, [\rho], [\mathbf{j}]\right) = \left(\sum_{i=1}^{10} \mathcal{L}_i\right) P\left(\mathbf{r}^N, \mathbf{p}^N, [\rho], [\mathbf{j}]\right), \tag{261}$$

with the operators $\mathcal{L}_7 - \mathcal{L}_{10}$ to describe the coupling in the equations of motion:

$$\mathcal{L}_7 = -\sum_i \Gamma_i \frac{\partial}{\partial p_{i\alpha}} u_{i\alpha}, \tag{262}$$

$$\mathcal{L}_8 = -\sum_i \Gamma_i \int d^3\mathbf{r} \Delta\left(\mathbf{r}, \mathbf{r}_i\right) \frac{\delta}{\delta j_\alpha(\mathbf{r})} \left(\frac{1}{m_i} p_{i\alpha} - u_{i\alpha}\right), \tag{263}$$

$$\mathcal{L}_9 = k_B T \sum_i \Gamma_i \int d^3\mathbf{r} \Delta\left(\mathbf{r}, \mathbf{r}_i\right) \frac{\delta}{\delta j_\alpha(\mathbf{r})} \int d^3\mathbf{r}' \Delta\left(\mathbf{r}', \mathbf{r}_i\right) \frac{\delta}{\delta j_\alpha(\mathbf{r}')}, \tag{264}$$

$$\mathcal{L}_{10} = -2k_B T \sum_i \Gamma_i \frac{\partial}{\partial p_{i\alpha}} \int d^3\mathbf{r} \Delta\left(\mathbf{r}, \mathbf{r}_i\right) \frac{\delta}{\delta j_\alpha(\mathbf{r})}. \tag{265}$$

The coupling of the fluid velocity to the particles is described by $\mathcal{L}_7$, while $\mathcal{L}_8$ describes the drag on the fluid. The stochastic contributions include fluid–fluid correlations via $\mathcal{L}_9$, and fluid–particle cross correlations via $\mathcal{L}_{10}$.

It should be noted that $\mathbf{u}_i$, being the result of the interpolation, depends on the fields $[\rho]$ and $[\mathbf{j}]$, so that $\delta u_i/\delta j_\alpha(\mathbf{r})$ is nonzero. Hence, the corresponding operators in $\mathcal{L}_8$ do not commute. Explicit functional differentiation shows that Eq. 258 holds in an analogous way for the interpolated velocity,

$$\int d^3\mathbf{r} \Delta\left(\mathbf{r}, \mathbf{r}_i\right) \frac{\delta}{\delta j_\alpha(\mathbf{r})} \exp\left(-\beta\mathcal{H}\right) = -\beta u_{i\alpha} \exp\left(-\beta\mathcal{H}\right). \tag{266}$$

Explicit calculations, as outlined for the uncoupled system, show that

$$(\mathcal{L}_7 + \mathcal{L}_8 + \mathcal{L}_9 + \mathcal{L}_{10}) \exp(-\beta\mathcal{H}) = 0, \tag{267}$$

which implies the exact FDT for the fully coupled system,

$$\left(\sum_{i=1}^{10} \mathcal{L}_i\right) \exp(-\beta\mathcal{H}) = 0. \tag{268}$$

An important consequence of this result is that a consistent simulation needs to thermalize *both* fluid and particle degrees of freedom; any other choice will violate the FDT.

The Langevin integrator for the particles is constructed in much the same way as the velocity Verlet algorithm for Molecular Dynamics. Although a Langevin analog to the Verlet algorithm has been known for some time [162], straightforward derivations have become available only recently, by applying operator–splitting techniques that were previously limited to Hamiltonian systems [163]. We employ a second–order integrator [135–137], which reduces to the velocity Verlet scheme in the limit of vanishing friction. Higher–order schemes are known [164], but they are considerably more complicated. Specifically, we approximately integrate the equations

$$\frac{d}{dt}\mathbf{r}_i = \frac{1}{m_i}\mathbf{p}_i, \tag{269}$$

$$\frac{d}{dt}\mathbf{p}_i = \mathbf{F}_i^c + \mathbf{F}_i^d + \mathbf{F}_i^f, \tag{270}$$

assuming that the fluid velocity $\mathbf{u}_i$ is constant over a time step h. This corresponds to the Fokker–Planck equation for the particles

$$\partial_t P\left(\mathbf{r}^N, \mathbf{p}^N, t\right) = (\mathcal{L}_r + \mathcal{L}_p) P\left(\mathbf{r}^N, \mathbf{p}^N, t\right) \tag{271}$$

with

$$\mathcal{L}_r = -\sum_i \frac{\partial}{\partial\mathbf{r}_i} \cdot \frac{\mathbf{p}_i}{m_i}, \tag{272}$$

$$\mathcal{L}_p = -\sum_i \frac{\partial}{\partial\mathbf{p}_i} \cdot \mathbf{F}_i^c + \sum_i \Gamma_i \frac{\partial}{\partial\mathbf{p}_i} \cdot \left(\frac{\mathbf{p}_i}{m_i} - \mathbf{u}_i\right) + k_B T \sum_i \Gamma_i \frac{\partial^2}{\partial\mathbf{p}_i^2}. \tag{273}$$

The formal solution

$$P\left(\mathbf{r}^N, \mathbf{p}^N, h\right) = \exp\left[(\mathcal{L}_r + \mathcal{L}_p) h\right] P\left(\mathbf{r}^N, \mathbf{p}^N, 0\right) \tag{274}$$

is approximated by a second-order Trotter decomposition,

$$\exp\left[(\mathcal{L}_r + \mathcal{L}_p) h\right] = \exp(\mathcal{L}_r h/2) \exp(\mathcal{L}_p h) \exp(\mathcal{L}_r h/2) + O(h^3). \tag{275}$$

The operator splitting implies the following algorithm: a half time step update of the coordinates with *constant momenta*,

$$\mathbf{r}_i(t + h/2) = \mathbf{r}_i(t) + \frac{h}{2}\frac{\mathbf{p}_i(t)}{m_i}, \tag{276}$$

followed by a full time step momentum update, with *constant coordinates*,

$$\mathbf{p}_i(t + h) = C_i^{(1)}(h)\mathbf{p}_i(t) + C_i^{(2)}(h)\left[\mathbf{F}_i^c + \Gamma_i\mathbf{u}_i\right] + C_i^{(3)}(h)\boldsymbol{\theta}_i, \tag{277}$$

and finally another half time step coordinate update, with *constant momenta*,

$$\mathbf{r}_i(t+h) = \mathbf{r}_i(t+h/2) + \frac{h}{2}\frac{\mathbf{p}_i(t+h)}{m_i}. \tag{278}$$

The coefficients in Eq. 277 are

$$C_i^{(1)}(h) = \exp\left(-\frac{\Gamma_i}{m_i}h\right), \tag{279}$$

$$C_i^{(2)}(h) = \frac{m_i}{\Gamma_i}\left[1 - \exp\left(-\frac{\Gamma_i}{m_i}h\right)\right], \tag{280}$$

$$C_i^{(3)}(h) = \sqrt{m_i k_B T\left[1 - \exp\left(-2\frac{\Gamma_i}{m_i}h\right)\right]}, \tag{281}$$

where $\theta_{i\alpha}$ are Gaussian random variables with zero mean and unit variance. Equation 277 is the *exact* solution of the momentum update, since Eq. 270 is a linear Langevin equation describing Brownian motion in a harmonic potential [158]. Thus the only source of error in integrating the particle motion is derived from the Trotter decomposition itself, Eq. 275. Nevertheless, it is important to limit the range of random numbers, to ensure that very large steps do not occasionally occur. It is therefore both desirable and more efficient to use distributions of random variates with finite range, which reproduce the Gaussian moments up to a certain order; in the present case, $O(h^2)$ accuracy requires that moments up to the fourth cumulant are correct. One possible choice is

$$P(\theta) = \frac{2}{3}\delta(\theta) + \frac{1}{6}\delta\left(\theta - \sqrt{3}\right) + \frac{1}{6}\delta\left(\theta + \sqrt{3}\right). \tag{282}$$

After the update of the particle momenta, the fluid force density, $\mathbf{f}^h(\mathbf{r})$ (Eq. 230), is distributed to the surrounding lattice sites. After one or more particle updates, the fluid variables are updated for a single LB time step, with the external forces being taken into account in the collision operator. This scheme is probably only first order accurate overall. It remains a challenge for the future to develop a unified framework to describe the fully coupled system and analyze its convergence properties; the algorithm could then perhaps be improved in a systematic fashion.

The input friction coefficient is *not* the same as the long–time friction coefficient, which is measured by the ratio of the particle velocity to the applied force [122]. Consider an isolated particle with "bare" (or input) friction coefficient Γ dragged through the fluid by a constant force $\mathbf{F}$, resulting in a steady particle velocity $\mathbf{U}$. The force balance requires that

$$\mathbf{F} = -\mathbf{F}^d = \Gamma(\mathbf{U} - \mathbf{u}_0), \tag{283}$$

where $\mathbf{u}_0$ is the fluid velocity at the particle center, $\mathbf{r}_0$,

$$\mathbf{u}_0 = \int d^3\mathbf{r}\,\Delta(\mathbf{r}, \mathbf{r}_0)\mathbf{u}(\mathbf{r}). \tag{284}$$

In the absence of thermal fluctuations, the deterministic fluid velocity field can be calculated in the Stokes flow approximation using the Green's function appropriate to the boundary conditions [22],

$$\mathbf{u}(\mathbf{r}) = \int d^3\mathbf{r}' \mathsf{T}(\mathbf{r}, \mathbf{r}') \cdot \mathbf{F}\Delta(\mathbf{r}', \mathbf{r}_0). \tag{285}$$

In an unbounded fluid, the Green's function reduces to the Oseen tensor [22], $\mathsf{T}(\mathbf{r}, \mathbf{r}') = \mathsf{O}(\mathbf{r} - \mathbf{r}')$, with

$$\mathsf{O}(\mathbf{r}) = \frac{1}{8\pi\eta r}\left(1 + \frac{\mathbf{rr}}{r^2}\right), \tag{286}$$

but Green's functions are also known for periodic boundary conditions [165] and planar boundaries [38, 39] as well. Combining Eqs. 283, 284 and 285,

$$\mathbf{u}_0 = \mathsf{T}^{av} \cdot \mathbf{F} = \Gamma \mathsf{T}^{av} \cdot (\mathbf{U} - \mathbf{u}_0), \tag{287}$$

where T^{av} is the Green's function averaged over the particle envelope,

$$\mathsf{T}^{av}(\mathbf{r}_0) = \int d^3\mathbf{r} \int d^3\mathbf{r}' \Delta(\mathbf{r}, \mathbf{r}_0)\Delta(\mathbf{r}', \mathbf{r}_0)\mathsf{T}(\mathbf{r}, \mathbf{r}'). \tag{288}$$

In a system with translational invariance, T^{av} is independent of $\mathbf{r}_0$ and proportional to the unit tensor by symmetry. Then from Eq. 287

$$\mathbf{F} = \frac{\Gamma}{1 + \mu_\infty \Gamma}\mathbf{U}, \tag{289}$$

where $\mu_\infty = T^{av}_{\alpha\alpha}/3$ accounts for the renormalization of Γ. If the size of the particle a is associated with the range of interaction of Δ, then dimensional analysis of Eq. 288 suggests that $\mu_\infty \sim (\eta a)^{-1}$. The effective friction coefficient, defined via $\mathbf{F} = \Gamma_{eff}\mathbf{U}$, is therefore diminished by the flow field induced by the applied force,

$$\frac{1}{\Gamma_{eff}} = \frac{1}{\Gamma} + \mu_\infty. \tag{290}$$

This relation has been verified numerically by extensive computer experiments [122, 140]. In the strong coupling limit, $\Gamma \to \infty$, the effective friction saturates to the limiting value $\Gamma_{eff} = \mu_\infty^{-1}$. This suggests assigning an effective radius to the interpolating function,

$$\frac{1}{a} = 6\pi\eta\mu_\infty. \tag{291}$$

However, for smaller values of the input friction, the effective particle size is given by

$$\frac{1}{a} = 6\pi\eta\left(\frac{1}{\Gamma} + \mu_\infty\right) = \frac{1}{a_0} + \frac{1}{gb}, \tag{292}$$

where $a_0 = \Gamma/6\pi\eta$ is the input particle radius and $gb = (6\pi\eta\mu_\infty)^{-1}$ depends on the interpolating function. The interesting physical parameter is Γ_{eff}, which describes the long–time behavior of the coupled system. Thus, to approach the continuum limit, one should keep Γ_{eff} constant as the lattice spacing is decreased, and change the bare coupling Γ as necessary.

It is not yet known how $\mathsf{T}^{av}(\mathbf{r}_0)$ behaves in the vicinity of a solid boundary, when translational invariance is broken. The compact support of the weighting function Δ suggests that T^{av} is a local correction and therefore largely independent of

macroscopic boundary conditions. Numerical simulations with periodic boundary conditions (Sec. 4.6) show that g is independent of system size and fluid viscosity. The weak system-size dependence reported in Ref. [140] is entirely accounted for by the difference between the periodic Green's function [165] and the Oseen tensor. Thus in a periodic unit cell of length L, Eq. 292 requires a correction of order $1/L$ [19],

$$\frac{1}{gb} = \frac{1}{a} + \frac{2.84}{L} - \frac{1}{a_0}. \tag{293}$$

4.6
Interpolating functions

In this section we consider translationally invariant interpolating functions, $\Delta(\mathbf{r}, \mathbf{r}_0) = \Delta(\mathbf{r} - \mathbf{r}_0)$ in more detail. For a discrete lattice, the interpolation procedure (*c.f.* Eq. 225) reads

$$\mathbf{u}(\mathbf{r}_0) = \sum_{\mathbf{r}} \Delta(\mathbf{r} - \mathbf{r}_0)\mathbf{u}(\mathbf{r}), \tag{294}$$

where $\mathbf{r}_0$ is the position of the particle, and $\mathbf{r}$ denotes the lattice sites. The normalization condition

$$\sum_{\mathbf{r}} \Delta(\mathbf{r} - \mathbf{r}_0) = 1 \tag{295}$$

must hold for all particle positions, $\mathbf{r}_0$, in order for the conservation laws to be satisfied exactly. We will assume the analysis of Sec. 4.5 carries over to the discrete system with no more than second-order discretization errors. Proof of this assumption remains for future work; here we numerically compare various choices of Δ.

Previous work, incorporating force coupling into spectral codes, used an isotropic Gaussian distribution for $\Delta(r)$ [155], but this is not commensurate with cubic lattice symmetry. Thus we take Δ as a product of one-dimensional functions [129]

$$\Delta(x, y, z) = \phi\left(\frac{x}{b}\right) \phi\left(\frac{y}{b}\right) \phi\left(\frac{z}{b}\right). \tag{296}$$

We first consider the two-point linear interpolating polynomial

$$\phi_2(u) = \begin{cases} 1 - |u| & |u| \leq 1, \\ 0 & |u| \geq 1, \end{cases} \tag{297}$$

which satisfies the following moment conditions for all real-valued u and integer j:

$$\sum_{j} \phi(u - j) = 1, \tag{298}$$

$$\sum_{j} j\phi(u - j) = u. \tag{299}$$

It exactly conserves momentum and angular momentum of the particle and fluid. However, ϕ_2 violates the condition

$$\sum_j \phi^2(u-j) = C, \tag{300}$$

where C is a constant, independent of u. The importance of this condition is explained in Ref. [129].

The conditions in Eqs. 298-300 can be satisfied by a three-point interpolation function,

$$\phi_3(u) = \begin{cases} \frac{1}{3}\left(1 + \sqrt{1-3u^2}\right) & 0 \le |u| \le \frac{1}{2} \\ \frac{1}{6}\left(5 - 3|u| - \sqrt{-2+6|u|-3u^2}\right) & \frac{1}{2} \le |u| \le \frac{3}{2} \\ 0 & \frac{3}{2} \le |u|. \end{cases} \tag{301}$$

An important property that emerges from ϕ_3 is that the first derivative, $\phi_3'(u)$, is continuous throughout the whole domain of u. This ensures that the velocity field varies smoothly across the grid, with a continuous spatial derivative $\nabla \mathbf{u}$. By contrast, linear interpolation leads to a continuous velocity but discontinuous derivatives.

In order to test the various interpolation schemes we have determined the settling velocity of a single particle in a periodic unit cell. A small force was applied to the particle and a compensating pressure gradient (or uniform force density) was added to the fluid, so that the net force on the system was zero. The steady-state particle velocity was determined, without allowing the particle to move on the grid [99]. This procedure is valid in Stokes flow, where an arbitrarily small velocity may be assumed, and gives a clean result for the variation in settling velocity with grid position. We used Eq. 293 to convert the measured mobility to a single parameter g, which does not depend on system size (L) or fluid viscosity (η). The mobility of the particle is reduced by the periodic images [165], but the correction in Eq. 293 accounts for the effects of the periodic boundaries quantitatively [99, 120, 166]. In simulations of polymer solutions an average of g over all grid positions is used.

The smoother velocity field derived from three-point interpolation means that the particle velocity is less dependent on the underlying grid than with linear interpolation, as can be seen in Fig. 5. Here we show the variation in effective particle size, as determined by the parameter g (Eq. 293), for linear (two point) interpolation (Eq. 297), three-point interpolation (Eq. 301), and the four-point interpolation,

$$\phi_4(u) = \begin{cases} \frac{1}{8}\left(3 - 2|u| + \sqrt{1+4|u|-4u^2}\right) & 0 \le |u| \le 1 \\ \frac{1}{8}\left(5 - 2|u| - \sqrt{-7+12|u|-4u^2}\right) & 1 \le |u| \le 2 \\ 0 & 2 \le |u|, \end{cases} \tag{302}$$

that is commonly used in immersed boundary methods [129]. As was recently noticed [130], the four-point interpolation leads to a much smaller variation in effective friction than linear interpolation. The parameter g varies with grid position by up to 20% in the case of linear interpolation, but by less than 1% with four-point interpolation. On the other hand, linear interpolation requires an envelope volume of 8 grid points, while the four-point scheme requires 64 grid points. Away from the strong-coupling limit, the grid dependence of the settling velocity is reduced since there is a non-negligible input mobility apart from the lattice contribution.
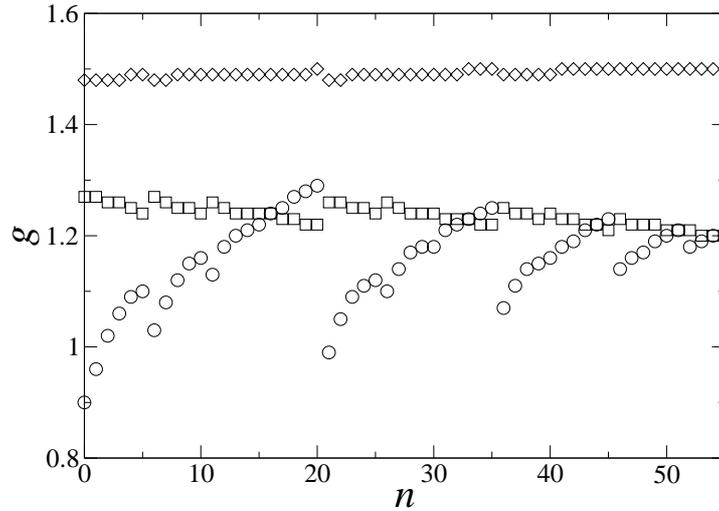
Fig. 5. Variation in settling velocity with grid location. The effective hydrodynamic radius was determined from $U = F/6\pi\eta a$ and converted to g using Eq. 293; g was found to be independent of η and L, as expected. Results are shown at 56 different grid positions (labeled by the index n), systematically varying the coordinates in steps of $0.1b$. Particles with input radius $a_0 = b$ were placed at coordinates $(ib/10, jb/10, kb/10)$, with $0 \leq i \leq j \leq k \leq 5$. Results are shown for the two-point (circles), three-point (squares) and four-point (diamonds) interpolation schemes.

Four-point interpolation is only necessary when using centered-difference approximations to the velocity and pressure fields [129], a situation that does not arise in LB simulations. We see that the three-point scheme is also much smoother than linear interpolation, with about a 3% variation in g. It is not as smooth as the four-point interpolation, but requires only 27 grid points. Furthermore, the smaller span of nodes means that the boundary surface is more tightly localized, and in fact the hydrodynamic interactions obtained with three-point interpolations are just as accurate as those obtained with four-point interpolation, as shown below.

An important test of the force coupling scheme is its ability to represent the hydrodynamic interactions between two spherical particles. As an example of the accuracy of the different interpolation schemes, in Fig. 6 we show the hydrodynamic interactions between two spheres moving along the line of centers. A small force is applied to sphere 1, in the direction of the vector between 1 and 2, and the velocity of sphere 2 is determined. From this we can calculate the hydrodynamic mobility μ_{12}^{pll}. The results are normalized by the mobility of the isolated sphere $\mu_0 = (6\pi\eta a)^{-1}$. Results were obtained for the two-point, three-point, and 4-point interpolation schemes, using a source particle placed on a grid point $(0, 0, 0)$ in one instance and in the center of the voxel $(b/2, b/2, b/2)$ in the other. The simulations were carried out in a periodic unit cell, with 20 grid points in each direction. Results are compared with a spectral solution of the Stokes equations in a periodic geom-

etry, assuming the force density on the particle surface is constant. For an isolated pair of particles this level of approximation includes the Oseen interaction and the Faxen correction; it corresponds to the Rotne-Prager (RP) interaction [23] used in most Brownian dynamics simulations of hydrodynamically interacting particles:

$$\mathbf{U}_2 = \left[\mathsf{T}(\mathbf{R}_{12}) + \frac{a^2}{12\pi\eta R_{12}^5} \left(R_{12}^2 \mathbf{1} - 3\mathbf{R}_{12}\mathbf{R}_{12} \right) \right] \cdot \mathbf{F}_1. \tag{303}$$

The periodic RP tensor can be calculated by Ewald summation [167] or by direct summation of Fourier components, which converges if used in conjunction with finite-volume sources [17, 168].

The results for the two-point interpolation show a significant dependence on the exact grid position when the particles are close to each other, $r < 4a$, but the results for the higher-order schemes are essentially independent of the grid. The three-point integration scheme is of comparable accuracy to the four-point scheme but requires less than half the number of grid points. It would seem to be the best choice for applications even though the particle motion is not quite as smooth. When the particles are widely separated, the simulations match almost perfectly with both the Oseen and RP solutions for the same periodic geometry; the typical errors are of the order of 0.1% of the Stokes velocity.

When the spheres are closer together, $r < 3a$, then the simulated hydrodynamic interactions match the Rotne-Prager interaction rather better than the Oseen interaction. This confirms that the weight function does make the particles behave as volume sources, rather than points. The best fit between simulation results and Stokes flow is obtained for an effective particle radius that is roughly $0.33w$, where w is the range of the weight function. So for two-point interpolation ($w = 2b$) the effective size is about $0.7b$, for three point interpolation ($w = 3b$) it is about $1.0b$ and for four-point interpolation ($w = 4b$) it is about $1.3b$. The actual values used in Fig. 6 are $0.8b$, $1.0b$ and $1.2b$ respectively. The optimal hydrodynamic radius is quite large, $a \sim b$, corresponding to strong coupling, $a_0 \sim 5b$. It remains an open question whether it is practical or desirable to run the fluctuating simulations with such large input friction.

5
Applications with hydrodynamic interactions

In this section we will discuss applications of the LB method to simulations of soft matter. We will briefly summarize some of our published work in this area, with the aim of indicating the breadth of possible applications of the method. Results will be summarized from simulations that cover a wide range of experimental length and time scales–from nanometers to millimeters and from nanoseconds to seconds.

5.1
Short-time diffusion of colloids

The first application of the fluctuating LB model was to the short-time diffusion of hard-sphere colloids. At the time, a new experimental technique–Diffusing Wave
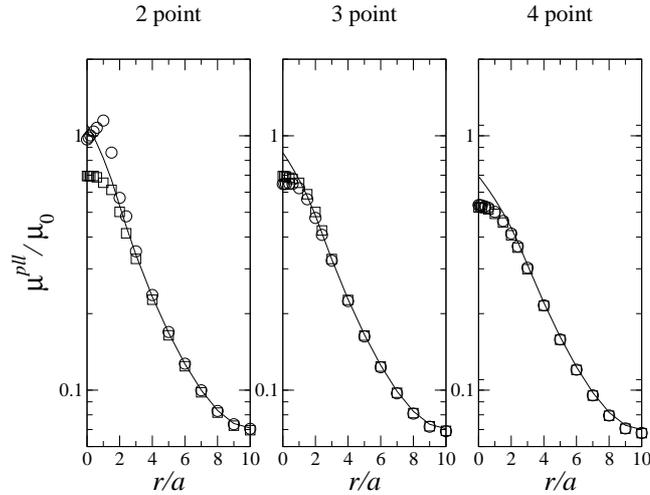
Fig. 6. Hydrodynamic interactions between a pair of spherical particles using the force-coupling method. The normalized mobility μ_{12}^{pll}/μ_0 is plotted at various separations r. We fit the effective hydrodynamic radius of each interpolating function to numerical solutions of the Stokes equations with a *uniform* force density on the sphere. These results correspond to a Rotne-Prager description of the hydrodynamic mobility and do not include lubrication. We show results at two different grid locations, $(0, 0, 0)$ (circles) and $(b/2, b/2, b/2)$ (squares), for two-point (left), three-point (center) and four-point (right) interpolation schemes.

Spectroscopy (DWS) [169]–enabled the study of the dynamics of colloids on time scales of a few nanoseconds. In general, the diffusion of a colloidal particle is a Markov process, but at such short times the developing hydrodynamic flow field gives rise to additional long-range correlations, analogous to the "long-time tails" in molecular dynamics [9]. Although the existence of long-time tails had been established theoretically [170, 171] and by molecular dynamics simulations [9], these experiments marked the first direct observation of correlated hydrodynamic fluctuations. Brownian and Stokesian dynamics both neglect long-range dynamic correlations, using instead the Stokes-flow approximation, which is typically only valid on time scales longer then one microsecond.

Long-time tails occur naturally in the dynamics of lattice-gas models of colloidal suspensions [173] and even of the lattice gases themselves [174]. It might be supposed that such correlations would be absent in a Boltzmann-level model, due to the Stosszahlansatz closure assumption. The fluctuating LB model described in Sec. 3 does not have any long-time tails in the stress autocorrelation functions, but mode coupling between the diffusion of fluid momentum and the diffusion of the colloidal particle does lead to an algebraic decay of the velocity correlation function of a suspended sphere [175]. In these simulations the particle-fluid coupling was implemented via the link-bounce-back (BB) algorithm [98, 120] described in
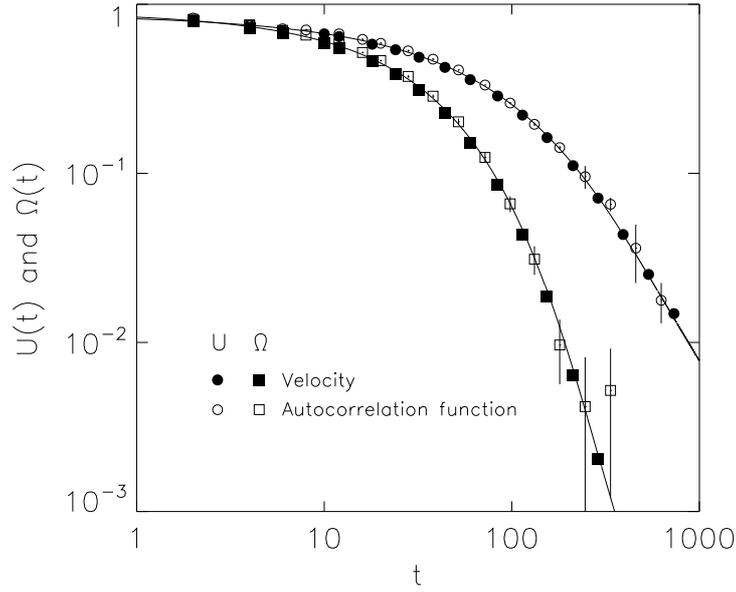
Fig. 7. Decay of translational (U) and rotational (Ω) velocity correlations of a suspended sphere. The time-dependent velocities of the sphere are shown as solid symbols; the relaxation of the corresponding velocity autocorrelation functions are shown as open symbols (with statistical error bars). A sufficiently large fluid volume was used so that the periodic boundary conditions had no effect on the numerical results for times up to $t = 1000$ in lattice units ($h = b = 1$). The solid lines are theoretical results, obtained by an inverse Laplace transform of the frequency dependent friction coefficients [172] of a sphere of appropriate size ($a = 2.6$) and mass ($\rho_s/\rho = 12$); the kinematic viscosity of the pure fluid $\eta_{kin} = 1/6$.

Sec. 4.1. Figure 7 shows the decay of translational and rotational velocity from two different types of computer experiment. In one case an initial velocity is imposed, which decays away due to viscous dissipation, and in the other the particle is set in motion by stress fluctuations in the fluid. Figure 7 shows that, within statistical errors, the normalized velocity correlation functions are identical to the steady decay of the translational and rotational velocities of the sphere; thus our simulations satisfy the fluctuation-dissipation theorem. Moreover the simulations agree almost perfectly with theoretical results derived from the frequency-dependent friction coefficients [172], even though there are no adjustable parameters in these comparisons; thus we see that the fluctuating lattice-Boltzmann equation can account for the hydrodynamic memory effects that lead to long-time tails [9].

The simulations were also used to measure self diffusion in dense colloidal suspensions, up to a solids volume fraction of 45%. The simulation data, shown in Fig. 8, exhibits the same scaling with amplitude and time found in the DWS experiments [176]. In Fig. 8 the amplitude of the mean-square displacement has been normalized by its limiting value $6D_s t$, where D_s is the short-time self-diffusion coefficient. $D_s(\phi)$ is a monotonically decreasing function of concentration, because
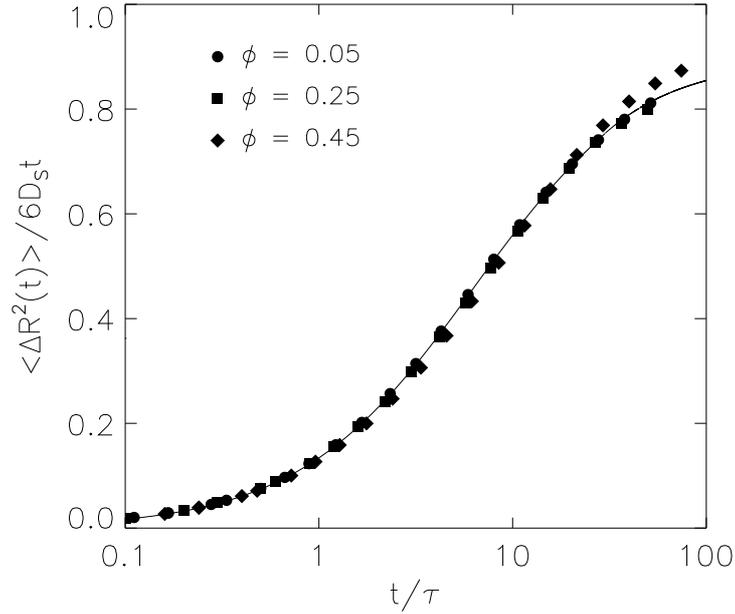
Fig. 8. Scaled mean-square displacement $\left\langle \Delta R^2(t) \right\rangle / 6D_s t$ at short times, *vs.* reduced time t/τ. Simulation results for 128 spheres (solid symbols) are shown at packing fractions ϕ of $5\%, 25\%$ and 45%; the solid line is the isolated sphere result. The suspension viscosity at these packing fractions is $1.14\eta_0$, $2.17\eta_0$, and $5.6\eta_0$ respectively, where η_0 is the viscosity of the pure fluid.

neighboring particles increasingly restrict the hydrodynamic flow field generated by the diffusing particle. Although the colloidal particles are freely moving in the fluid, the no-slip boundary condition induces stresslets and higher force multipoles on the particle surfaces; $D_s(\phi)$ is one average measure of these hydrodynamic interactions. The normalized mean-square displacement has a single relaxation time, so that when the time axis is scaled by τ all the data collapse onto a single curve, which is the same as for an isolated sphere. The relaxation time τ is the viscous diffusion time $\rho a^2/\eta$, of a single particle in a fluid of viscosity η, where $\eta(\phi)$ is numerically similar to the high-frequency viscosity of the suspension [19]. This observation, which is in line with experimental measurements [176, 177], suggests that the short-time diffusion is essentially mean field like.

5.2
Dynamic scaling in polymer solutions

The classical theory [6] of the equilibrium dynamics of polymer chains in solution is the Zimm model [178], which considers a single flexible chain in a good solvent, such that its conformations are given by a random coil with excluded volume segments:

$$R \sim bN^{\nu}. \tag{304}$$

Here, R is the size of the coil, measured in terms of the gyration radius or the end–to–end distance, while N denotes the number of monomers in the chain or the degree of polymerization, and b is the monomer size. Long–range interactions like electrostatics, or effects of poor solvent quality, are not considered. Furthermore, the solution is considered to be dilute, such that the chains do not overlap and a single–chain picture is sufficient. In other words, the standard Zimm model applies in the upper left corner of the generic phase diagram given in Fig. 9. Here the exponent ν takes the value $\nu \approx 0.59$ in three dimensions, because the excluded volume interaction leads to swelling of the chain when compared to an ideal random coil ($\nu = 1/2$). A polymer with excluded-volume is thus a self–similar random fractal with dimension $1/\nu$.

The Zimm model is based on the Rouse model [6, 179], but includes long-range hydrodynamic interactions between the segments. Both models predict self–similarity, not only with respect to space, but also with respect to time. Therefore the dynamics is conveniently described in terms of an exponent z, connecting the chain relaxation time τ_R with the size of the coil R:

$$\tau_R \propto R^z. \tag{305}$$

The internal degrees of freedom completely re–organize on a time scale τ_R, leading to statistically independent conformations. This is also the time that the chain needs to diffuse through a distance equal to its own size:

$$D_{cm}\tau_R \sim R^2, \tag{306}$$

where D_{cm} is the translational diffusion coefficient, describing the center–of–mass motion. These two relations can be combined to determine the scaling of D_{cm} with chain size:

$$D_{cm} \propto R^{2-z}. \tag{307}$$

In the *Zimm* model, the hydrodynamic interactions result in strongly correlated motions, such that the coil as a whole behaves like a Stokes sphere, $D_{cm} \propto R^{-1}$, or

$$z = 3. \tag{308}$$

The *Rouse* model neglects hydrodynamic interactions and the monomer friction coefficients add up to give a total friction coefficient that is linearly proportional to N. Since $D_{cm} \propto N^{-1} \propto R^{-1/\nu}$,

$$z = 2 + \frac{1}{\nu}, \tag{309}$$

corresponding to slower dynamics.

Self–similarity implies that the relaxation of the internal degrees of freedom also scales with the exponent z on time scales $\tau_b \ll t \ll \tau_R$, where τ_b is the relaxation time on the monomer scale b. In the space–time window $b \ll l \ll R$, $\tau_b \ll t \ll \tau_R$, there is a scaling of the mean square displacement of a monomer,
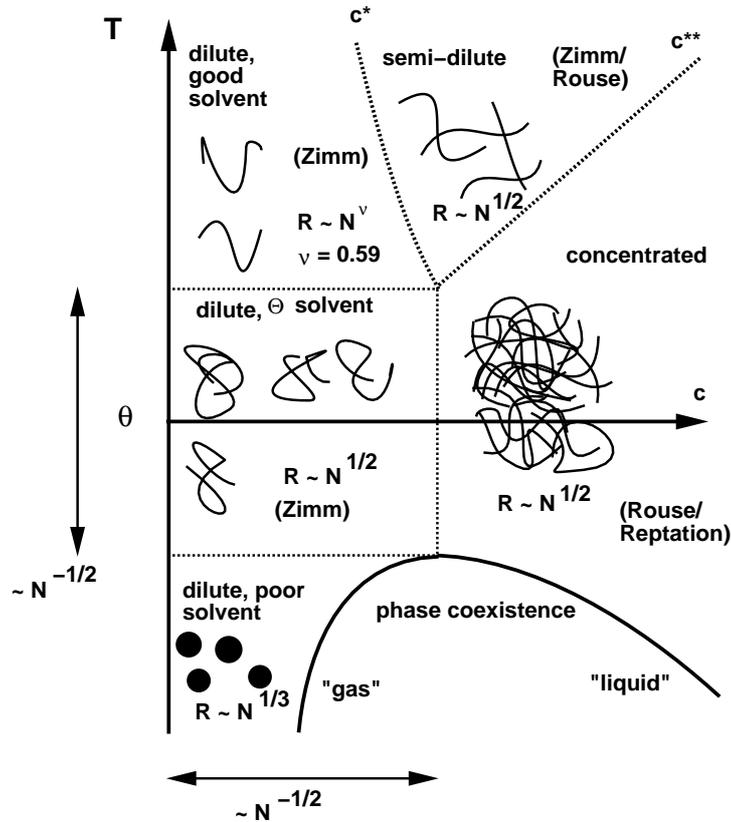
$$\langle \Delta r^2 \rangle \propto t^{2/z}, \tag{310}$$

Fig. 9. Phase diagram of a polymer solution, in the $c - T$ plane, where c is the monomer concentration and T is the temperature (parameterizing solvent quality). The static properties are characterized by scaling laws which describe the dependence of the chain size R (gyration radius or end–to–end–distance for example) on the degree of polymerization N. In the dilute limit ($c \to 0$) the so–called theta transition occurs, where at $T = \Theta$, single isolated chains collapse from a swollen random coil to a compact globule. For finite chain length N, this transition is "smeared out" over a temperature region $\Delta T \propto N^{-1/2}$, in which the chain conformations are Gaussian. Below Θ, there is phase coexistence between a "gas" of globules and a "liquid" of strongly interpenetrating Gaussian chains. The corresponding critical point occurs at a very low concentration, $c_c \propto N^{-1/2}$, and in the vicinity of Θ, $\Theta - T_c \propto N^{-1/2}$. The crossover region, which connects the regime of swollen isolated coils with that of the concentrated (Gaussian) solution at high temperatures, is called the semidilute regime. The dynamics is characterized by the Zimm model in the dilute limit where hydrodynamic interactions are important, and by the Rouse model for dense systems where they are screened. For very dense systems or sufficiently long chains, where curvilinear motion dominates, the Rouse model must be replaced by the reptation model (or the crossover behavior between these two cases). The Rouse and Zimm models are briefly described in the text.

while the dynamic structure factor of a single chain of N monomers

$$S(k,t) = \frac{1}{N} \left\langle \sum_{ij=1}^{N} \exp\left(i\mathbf{k} \cdot (\mathbf{r}_i(t) - \mathbf{r}_j(0))\right) \right\rangle \tag{311}$$

scales as

$$S(k,t) = k^{-1/\nu} f\left(k^2 t^{2/z}\right). \tag{312}$$

The Zimm model applies to dilute solutions, and, therefore, to the dynamics of a single solvated chain. It has become a benchmark system, used to test the validity of mesoscopic simulation methods. A single chain, modeled by bead–spring interactions, coupled to a surrounding solvent to account for hydrodynamic interactions, has been successfully simulated via (i) Molecular Dynamics [180–182], (ii) Dissipative Particle Dynamics [183, 184], Multi–Particle Collision Dynamics [185, 186], and by Lattice Boltzmann [122], applying the dissipative coupling described in Sec. 4.5. These studies are nowadays all sufficiently accurate to be able to clearly distinguish between Rouse and Zimm scaling. However, a more demanding goal is to verify not only the exponent, but also the prefactor of the dynamic scaling law.

The Kirkwood approximation to the diffusion constant,

$$D^{(K)} = \frac{k_B T}{\Gamma N} + \frac{k_B T}{6\pi\eta} \left\langle \frac{1}{R_H} \right\rangle, \tag{313}$$

(Γ is the monomer friction coefficient) can be calculated from a conformational average of the hydrodynamic radius R_H,

$$\left\langle \frac{1}{R_H} \right\rangle = \frac{1}{N^2} \sum_{i \neq j} \left\langle \frac{1}{r_{ij}} \right\rangle. \tag{314}$$

Highly accurate results for a single chain in a structureless solvent have been obtained by Monte Carlo methods [187, 188]. However, a naive comparison will fail badly. The expression for R_H (Eq. 314) assumes an infinite system, but in a simulation the system is confined to a periodic unit cell, which is typically not substantially larger than the size of the coil. The effects of periodic boundaries can be accounted for quantitatively, by replacing the Oseen tensor with an Ewald sum that includes the hydrodynamic interactions with the periodic images [167]. The consequences of this have been worked out in detail for polymers [182] and colloids [19]. The main result is that the hydrodynamic radius must be replaced by a system–size dependent effective hydrodynamic radius; the leading–order correction is proportional to R/L, where L is the linear dimension of the periodic simulation cell. Interestingly, *internal* modes, such as Rouse modes [6], where the motion of the center of mass has been subtracted, have a much weaker finite–size effect, which scales as L^{-3}, corresponding to a dipolar hydrodynamic interaction with the periodic images [122]. Taking the finite–size effects into account, the predictions of the Zimm model are nicely confirmed.

However, the Zimm model is no longer valid as soon as the chains start to overlap. Here a double screening mechanism sets in: (i) Screening of excluded volume
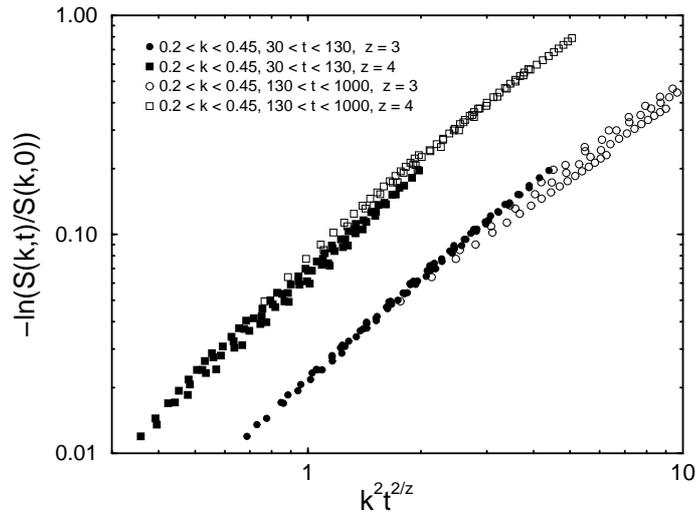
Fig. 10. Scaling of the single–chain dynamic structure factor data, showing both Rouse and Zimm scaling [43]. The wave number k has been restricted such that only length scales above the blob size are probed ($k\xi < 1$), while the size of the polymer chain as a whole does not yet matter ($kR_G > 1$). The data are labeled according to the time regimes; solid symbols refer to the short–time regime below the blob relaxation time, $t < \tau_\xi$, while open symbols are for later times $t > \tau_\xi$. The upper curve is for Rouse scaling ($z = 4$) and the lower curve for Zimm scaling ($z = 3$). One sees that Zimm scaling works better in the short–time regime, while Rouse scaling holds for later times.

interactions (Flory screening). In a dense melt, the chain conformations are not those of a self–avoiding walk, but rather those of a random walk ($\nu = 1/2$). Essentially, this is an entropic packing effect: A swollen coil would take too much configuration space from the surrounding chains. This effect can be understood in terms of a self–consistent mean–field theory, which is expected to work well for dense systems where density fluctuations are suppressed [7]. (ii) Screening of hydrodynamic interactions. In dense melts, the dynamics is not Zimm–like, but rather Rouse–like, or governed by reptation [6]. Reptation occurs for long chains in dense systems, where topological constraints enforce an essentially curvilinear motion. We will not be concerned with these latter effects, but rather with the mechanism which leads to the suppression of hydrodynamic interactions. Based upon the results of computer simulations [43], we were able to develop a simple picture, which essentially confirmed the previous work by de Gennes [189], and completed it. The basic mechanism is chain–chain collisions. A monomer encountering another chain will deform it elastically, inducing a stress along the polymer backbone instead of propagating the signal into the surroundings. Since the chain arrangements are random, the fluid momentum is also randomized, such that momentum correlations (or hydrodynamic interactions) are destroyed.

The crossover region between dilute and dense systems is called the semidilute regime. A semidilute solution is characterized by strongly overlapping chains which are however so long and so dilute that the monomer concentration can still be considered as vanishingly small. Apart from b and R, there is now a third important length scale, the "blob size" ξ with $b \ll \xi \ll R$. Essentially, ξ is the length scale on which interactions with the surrounding chains become important; this length scale controls the crossover from dilute to dense behavior. The chain conformations are characterized by $\nu = 0.59$ on length scales much smaller than ξ, while on length scales substantially above ξ the exponent is $\nu = 1/2$. The challenge for computer simulations is that both behaviors need to be resolved simultaneously, which is only possible for $N > 10^3$. Roughly 30 monomers are needed to resolve the random fractal structure within the blob, while another 30 blobs per chain are needed to observe the random walk regime. Furthermore, a many–chain system should be run without self–overlaps, and this leads to the conclusion [43] that the smallest system to simulate semidilute dynamics contains roughly 5×10^4 monomers and 5×10^5 LB lattice sites.

The picture which emerges from these simulations [43] can be summarized as follows. Initially, the dynamics is Zimm–like, even for length scales beyond the blob size. The reason is that hydrodynamic signals can spread easily throughout the system, and just drag the chains with them. This continues until chain–chain collisions start to play a role. The relevant time scale is the blob relaxation time $\tau_\xi \propto \xi^3$, *i.e.* the time a blob needs to move its own size. From then on, the screening mechanism described above becomes important, and the dynamics is Rouse–like. This is only observable on length scales beyond the blob size, since on smaller scales all dynamic correlations have decayed already. This is nicely borne out by single–chain dynamic structure factor data (see Fig. 10), and explains the previous observation of "incomplete screening" [190] in a straightforward and natural way.

5.3
Polymer migration in confined geometries

Flexible polymers in a pressure-driven flow field migrate towards the center of the channel, because of hydrodynamic interactions. The local shear rate stretches the polymer and the resulting tension in the chain generates an additional flow field around the polymer. This flow field becomes asymmetric near a no-slip boundary and results in a net drift towards the center of the channel [191–193]. Recent simulations [193, 194] show that hydrodynamic lift is the dominant migration mechanism in pressure-driven flow, rather than spatial gradients in shear rate. Recently, we used numerical simulations to investigate a flexible polymer driven by a combination of fluid flow and external body force [195], but ignoring the complications arising from counterion screening in electrophoretic flows. We used the fluctuating LB model (Sec. 3) in conjunction with the point-force coupling scheme described in Sec. 4.5.

We were surprised to find that the polymer migrates towards the channel center under the action of a body-force alone, while in combination with a pressure-driven flow the polymer can move either towards the channel wall or towards the channel
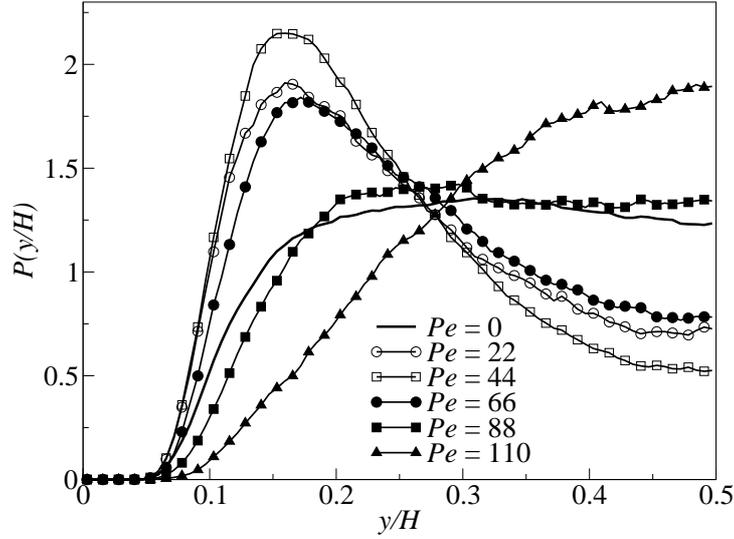
Fig. 11. Center of mass distributions for countercurrent application of an external body force and pressure-driven flow in a channel of width H. The solid curve shows the level of migration under the pressure-driven flow only. The flow Peclet number in all cases is $Pe_f = 12.5$. The boundary is at $y/H = 0$ and the center of the channel is at $y/H = 0.5$; $H = 8R_g$.

center. The external field and pressure gradient result in two different Peclet numbers: $Pe = \overline{U}R_g/D$ and $Pe_f = \overline{\gamma}R_g{}^2/D$. Here $\overline{U}$ is the average polymer velocity with respect to the fluid, and $\overline{\gamma}$ is the average shear rate. The interplay between force and flow can lead to a wide variety of steady-state distributions of the polymer center of mass across the channel [195]. For example, in a countercurrent application of the two fields, the polymer tends to orient in different quadrants depending on the relative magnitude of the two driving forces. The polymer then drifts either towards the walls or towards the center depending on its mean orientation. The results in Fig. 11 show migration towards the boundaries when the external force is small ($Pe < 30$), but increasing the force eventually reverses the orientation of the polymer and the polymer again migrates towards the center ($Pe > 100$).

The simulations mimic recent experimental observations of the migration of DNA in combined electric and pressure-driven flow fields [196, 197]. The similarities between these results suggest that hydrodynamic interactions in polyelectrolyte solutions are only partially screened. In fact, within the Debye-Hückel approximation, there is a residual dipolar flow field [198]. Although this flow is weak in comparison to the electrophoretic velocity, its dipolar orientation enables it to drive a transverse migration of the polymer. A recent kinetic theory calculation [199] supports these qualitative observations.

5.4
Sedimentation

The previous examples have focused on sub-micron sized particles, colloids and polymers, where Brownian motion is an essential component of the dynamics. For particles larger than a few microns, Brownian motion is negligible under normal laboratory conditions and a suspension of such particles can be simulated using the deterministic version of the LB equation (see Sec. 3). There is an interesting regime of particle sizes, from 1–100 micron depending on solvent, where Brownian motion is negligible, yet inertial effects are still unimportant. This corresponds to the region of low Reynolds number ($Re = Ud/\eta_{kin}$) but high Peclet number ($Pe = Ud/D$). Here U is the characteristic particle velocity, d is the diameter, and D is the particle diffusion coefficient. Because of the large difference in time scale between diffusion of momentum and particle diffusion, it is quite feasible for Pe to be $6 - 10$ orders of magnitude larger than Re. We have carried out a number of simulations in this regime, with the aim of elucidating the role of suspension microstructure in controlling the amplitude of the velocity fluctuations as the suspension settles.

In a sedimenting suspension, spatial and temporal variations in particle concentration drive large fluctuations in the particle velocities, of the same order of magnitude as the mean settling velocity. For particles larger than a few microns, this hydrodynamic diffusion dominates the thermal Brownian motion, and in the absence of inertia ($Re \ll 1$), the particle velocities are determined entirely by the instantaneous particle positions. If the particles are randomly distributed, then the velocity fluctuations will diverge with increasing container size [200], although the density fluctuations may eventually drain out of the system by convection [201]. However, experimental measurements indicate that the velocity fluctuations converge to a finite value as the container dimensions are increased [202, 203], but the mechanism by which the velocity fluctuations saturate is not yet clear. Some time ago, Koch and Shaqfeh suggested that the distribution of pairs of particles could be modified by shearing forces induced by the motion of a third particle, and that these changes in microstructure could in turn lead to a screening of the long-range hydrodynamic interactions driving the velocity fluctuations [204]. However, detailed numerical simulations found no evidence of the predicted microstructural changes [205]. Instead the velocity fluctuations in homogeneous suspensions (with periodic boundary conditions) were found to diverge with increasing cell size. More recently, it has been proposed that long wavelength density fluctuations can be suppressed by a convection diffusion mechanism [206, 207], but a bulk screening mechanism cannot be reconciled with the results of computer simulations [144, 205]. Alternatively, it has been suggested that the vertical walls of the container may modify, although not eliminate, the divergence of the velocity fluctuations [208]. Most recently, it has been shown [209, 210] that a small vertical density gradient can damp out diverging velocity fluctuations.

Lattice-Boltzmann simulations were used to test these theoretical ideas, comparing the behavior of the velocity fluctuations in three different geometries [211]. We found striking differences in the level of velocity fluctuations, depending on the
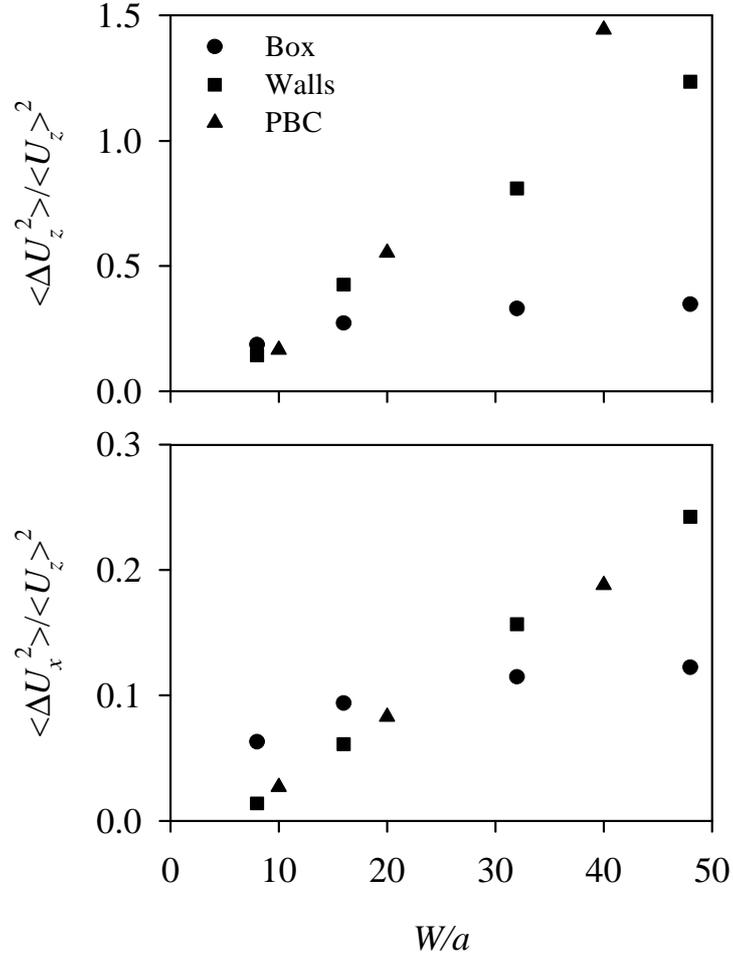
Fig. 12. Relative velocity fluctuations $\left\langle \Delta U_\alpha^2 \right\rangle / \left\langle U_z \right\rangle^2$ as a function of container width. The vertical ($\left\langle \Delta U_z^2 \right\rangle$) and horizontal ($\left\langle \Delta U_x^2 \right\rangle$) fluctuations are shown for three different boundary conditions: a cell bounded in all three directions by no-slip walls (Box), a cell bounded by vertical walls (Walls), and a cell that is periodic in all three directions (PBC) [144, 205]. The statistical errors are comparable to the size of the symbols.

macroscopic boundary conditions. In a geometry similar to those used in laboratory experiments [202, 203], namely a rigid container bounded in all three directions, we found that the calculated velocity fluctuations saturate with increasing container dimensions, as observed experimentally, but contrary to earlier simulations with periodic boundary conditions [144, 205]. The main result is illustrated in Fig. 12, and suggests that the velocity fluctuations in a bounded container are independent of container width for sufficiently large containers. On the other hand, in vertically homogeneous suspensions velocity fluctuations are proportional to the container width,

regardless of the boundary conditions in the horizontal plane. The significance of this result is that it establishes that velocity fluctuations in a sedimenting suspension depend on the macroscopic boundary conditions and that laboratory measurements [202, 203, 212] are not necessarily characteristic of a uniform suspension, as had been supposed. Instead, the simulations show that vertical variations in particle concentration are responsible for suppressing the velocity fluctuations, which otherwise diverge with increasing container size, in agreement with theory [200] and earlier simulations [144, 205]. The upper and lower boundaries apparently act as sinks for the fluctuation energy [201], while in homogeneous suspensions velocity fluctuations remain proportional to the system size [200].

5.5
Inertial migration in pressure-driven flow

At still larger particle sizes, typically in excess of 100 microns, the inertia of the fluid can no longer be ignored. For suspended particles in a gravitational field, the Reynolds number grows in proportion to the cube of the particle size. Inertia breaks the symmetry inherent in Stokes flow and leads to new phenomena, and in particular the possibility of lateral migration of particles. A particle in a shear flow experiences a transverse force at non-zero Re, with a direction that depends on the velocity of the particle with respect to the fluid velocity at its center. Thus if the particle is moving slightly faster than the fluid it moves crosswise to the flow in the direction of lower fluid velocity and vice-versa [213]; if it is moving with the local stream velocity then it does not migrate in the lateral direction at all. Now in Poiseuille flow, a spherical particle moves faster than the surrounding fluid because of the Faxen force, proportional to the curvature in the fluid velocity field. Thus particles tend to migrate towards the channel walls [214]. However, near the wall the particle is slowed down by the additional drag with the wall and so eventually migrates the other way. At small Reynolds numbers ($Re < 100$), these forces balance when the particle is at a radial position of roughly $0.6R$, where R is the radius of the pipe. In a cylindrical pipe, a uniformly distributed suspension of particles rearranges to form a stable ring located at approximately $0.6R$ [215]. Theoretical calculations for small particles in plane Poiseuille flow give similar equilibrium positions to those observed experimentally [216, 217]. The profile of the lateral force across the channel shows only one equilibrium position, which shifts closer to the boundary wall as the Reynolds number increases. Our interest in this problem was sparked by two recent experimental observations: first that particles tend to align near the walls to make linear chains of more or less equally-spaced particles [215, 218], and second that at high Reynolds numbers ($Re \sim 1000$) an additional inner ring of particles was observed when the ratio of particle diameter d to cylinder diameter D was of the order of 1:10 [219]. Large particles introduce an additional Reynolds number, $Re_p = Re \cdot (d/D)^2$, which may not be small, as assumed theoretically [216, 217]. We used the LB method to investigate inertial migration of neutrally buoyant particles in the range of Reynolds numbers from 100 to 1000 [220]. Individual particles in a channel with a square cross section migrate to one of a small number of equilibrium positions in the cross-

sectional plane, located near an edge or at the center of a face; we could not identify any stable postions for single particles near the center of the channel.
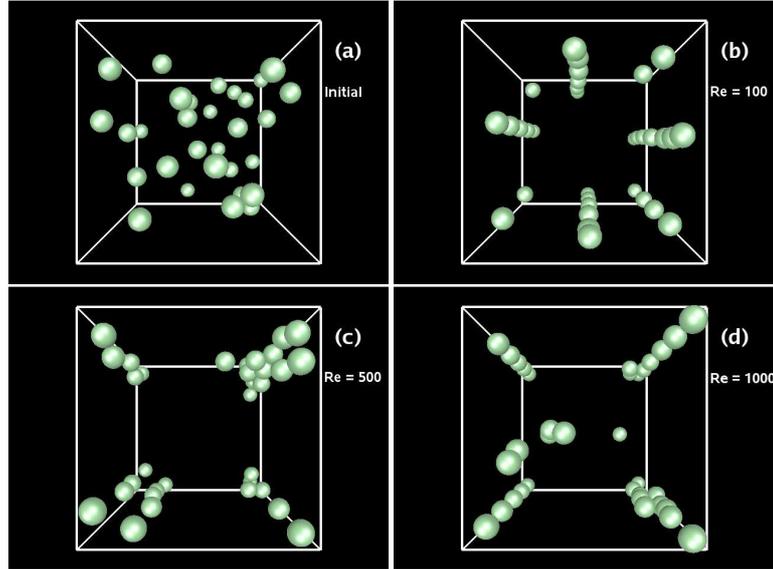

Fig. 13. Snapshots of particle configurations in a duct flow at different Reynolds numbers; the flow is into the plane of the paper: (a) Initial configuration (b) $Re = 100$ (c) $Re = 500$ (d) $Re = 1000$. The ratio $H/d = 9.1$, the number of particles $N = 32$ and the volume fraction $\phi = 1\%$.

To investigate multiparticle suspensions, random configurations of particles were prepared at a volume fraction $\phi = 1\%$ and size ratio $H/d = 9.1$. The Reynolds number in the simulations varied between 100 and 1000. An initially uniform distribution, shown in Fig. 13a, evolves into three different steady-state distributions depending on Re. At $Re = 100$ (Fig. 13b) particles are gathered around the eight equilibrium positions and strongly aligned in the direction of the flow, making linear chains of more or less uniformly spaced particles. Similar trains of particles were observed in laboratory experiments [218]. At $Re = 500$ (Fig. 13c) the particles are gathered in one of the four most stable positions, near each corner. By a Reynolds number of 500, the trains are unstable and the spacing between the particles is no longer uniform. Instead transient aggregates of closely-spaced particles are formed, again near the corners of the duct. However at still higher Reynolds number, $Re = 1000$, there is another change in particle configuration (Fig. 13d), and particles appear in the center of the duct. A central band was first observed in experiments in a cylindrical pipe [219], but its origin remains unclear. We observe that the central particles have a substantial diffusive motion in the velocity-gradient plane, whereas the particle trains exhibit little transverse diffusion. Since there are no single-particle equilibrium positions at the duct center, the presence of particles in the inner region is clearly due

to multi-body interactions. Nevertheless this migration cannot be a shear-induced migration of the kind that occurs in low-Reynolds number flows [221].

Our simulations suggest that the inner band of particles is the result of the formation of transient clusters of particles. We proposed [220] that at higher Reynolds numbers ($Re > 500$) the trains become unstable and clusters of closely-spaced particles arise, as can be seen in Fig. 13c. Simulations of tethered pairs of particles have shown that additional equilibrium positions arise for pairs of particles at Reynolds numbers in excess of 750 [220]. Thus transient clusters are formed at higher Reynolds numbers, which drift towards the center of the channel making the additional ring observed in experiments [219] and simulations (Fig. 13d). Eventually, the cluster disintegrates from hydrodynamic dispersion and the particles return to the walls. At steady state, there is a flux of pairs and triplets of particles moving towards the center, balanced by individual particles moving towards the walls. This also explains why the particles in the inner region are highly mobile, while those near the walls have a very small diffusivity.

Acknowledgements

References

[1] Chaikin PM, Lubensky TC (1997) Principles of Condensed Matter Physics. Cambridge University Press, Cambridge

[2] Russel WB, Saville DA, Schowalter WR (1995) Colloidal Dispersions. Cambridge University Press, Cambridge

[3] Lyklema J (1991) Fundamentals of Interface and Colloid Science. Academic Press, London

[4] Evans DF, Wennerström H (1999) The Colloidal Domain. Wiley-VCH, New York, 2nd edn.

[5] de Gennes PG (1979) Scaling Concepts in Polymer Physics. Cornell University Press, Ithaca

[6] Doi M, Edwards SF (1986) The Theory of Polymer Dynamics. Oxford University Press, Oxford

[7] Grosberg AY, Khokhlov AR (1994) Statistical Physics of Macromolecules. AIP Press, New York

[8] Nelson P (2007) Biological Physics. W. H. Freeman, New York

[9] Alder BJ, Wainwright TE (1970) Phys Rev A 1:18

[10] Montfrooij W, de Schepper I (1989) Phys Rev A 39:2731

[11] Bird RB, Curtiss CF, Armstrong RC, Hassager O (1987) Dynamics of Polymeric Liquids. Wiley, New York

[12] Grest GS, Kremer K (1986) Phys Rev A 33:3628
[13] Weeks JD, Chandler D, Andersen HC (1971) J Chem Phys 54:5237
[14] Hansen JP, McDonald IR (1986) Theory of Simple Liquids. Academic Press, London
[15] Risken H (1984) The Fokker–Planck Equation. Springer–Verlag, Berlin
[16] Gardiner CW (1985) Handbook of Stochastic Methods for Physics, Chemistry, and the Natural Sciences. Springer-Verlag, Berlin
[17] Mazur P, Saarloos WV (1982) Physica A 115:21
[18] Cichocki B, Felderhof BU (1988) J Chem Phys 89:3705
[19] Ladd AJC (1990) J Chem Phys 93:3484
[20] Sangani AS, Mo G (1996) Phys Fluids 8:1990
[21] Cichocki B, Jones RB, Kutteh R, Wajnryb E (2000) J Chem Phys 112:2548
[22] Happel J, Brenner H (1986) Low-Reynolds Number Hydrodynamics. Martinus Nijhoff, Dordrecht
[23] Rotne J, Prager S (1969) J Chem Phys 50:4831
[24] Wajnryb E, Szymczak P, Cichocki B (2004) Physica A 335:339
[25] Öttinger HC (1996) Stochastic Processes in Polymeric Fluids. Springer-Verlag, Berlin
[26] Kröger M (2004) Phys Rep 390:453
[27] Ermak DL, McCammon JA (1978) J Chem Phys 69:1352
[28] Liu B, Dünweg B (2003) J Chem Phys 118:8061
[29] Brady JF, Bossis G (1988) Ann Rev Fluid Mech 20:111
[30] Fixman M (1986) Macromolecules 19:1204
[31] Jendrejack RM, Graham MD, dePablo JJ (2000) J Chem Phys 113:2894
[32] Sierou A, Brady JF (2001) J Fluid Mech 448:115
[33] Banchio AJ, Brady JF (2003) J Chem Phys 118:10323
[34] Saintillan D, Darve E, Shaqfeh ESG (2005) Macromolecules 17:33301
[35] Hernandez-Ortiz JP, de Pablo JJ, Graham MD (2007) Phys Rev Lett 98:140602
[36] Meng Q, Higdon JJL (2008) J Rheol 52:1
[37] Meng Q, Higdon JJL (2008) J Rheol 52:37
[38] Blake JR (1971) Proc Camb Phil Soc 70:303
[39] Liron N, Mochon S (1976) J Eng Math 10:287
[40] Cichocki B, Jones RB (1998) Physica A 258:273
[41] Jendrejack RM, Graham MD, dePablo JJ (2003) J Chem Phys 119:1165
[42] Landau LD, Lifshitz EM (1959) Fluid Mechanics. Addison-Wesley, London
[43] Ahlrichs P, Everaers R, Dünweg B (2001) Phys Rev E 64:040501 (R)
[44] Hoogerbrugge PJ, Koelman JMVA (1992) Europhys Lett 19:155
[45] Koelman JMVA, Hoogerbrugge PJ (1993) Europhys Lett 21:369
[46] Español P, Warren P (1995) Europhys Lett 30:191
[47] Español P (1995) Phys Rev E 52:1734
[48] Groot R, Warren P (1997) J Chem Phys 107:4423
[49] Español P (1998) Phys Rev E 57:2930
[50] Pagonabarraga I, Hagen MJH, Frenkel D (1998) Europhys Lett 42:377
[51] Gibson JB, Chen K, Chynoweth S (1999) Int J Mod Phys C 10:241

[52] Besold G, Vattulainen I, Karttunen M, Polson JM (2000) Phys Rev E 62:R7611
[53] Vattulainen I, Karttunen M, Besold G, Polson JM (2002) J Chem Phys 116:3967
[54] Nikunen P, Karttunen M, Vattulainen I (2003) Comp Phys Comm 153:407
[55] Shardlow T (2003) SIAM J Sci Comp 24:1267
[56] Soddemann T, Dünweg B, Kremer K (2003) Phys Rev E 68:046702
[57] Junghans C, Praprotnik M, Kremer K (2008) Soft Matter 4:156
[58] Malevanets A, Kapral R (1999) J Chem Phys 110:8605
[59] Ihle T, Kroll DM (2003) Phys Rev E 67:066705
[60] Ihle T, Kroll DM (2003) Phys Rev E 67:066706
[61] Kikuchi N, Pooley CM, Ryder JF, Yeomans JM (2003) J Chem Phys 119:6388
[62] Ihle T, Tüzel E, Kroll DM (2004) Phys Rev E 70:035701(R)
[63] Sharma N, Patankar NA (2004) J Comp Phys 201:466
[64] Car R, Parrinello M (1985) Phys Rev Lett 55:2471
[65] Höfler K, Schwarzer S (2000) Phys Rev E 61:7146
[66] Schwarzer S (1995) Phys Rev E 52:6461
[67] Kalthoff W, Schwarzer S, Herrmann HJ (1997) Phys Rev E 56:2234
[68] Wachmann B, Kalthoff W, Schwarzer S, Herrmann HJ (1998) Granular Matter 1:75
[69] Delgado-Buscalioni R, Coveney PV (2003) Phys Rev E 67:046704
[70] Delgado-Buscalioni R, Flekkoy EG, Coveney PV (2005) Europhys Lett 69:959
[71] Delgado-Buscalioni R, Coveney PV, Riley GD, Ford RW (2005) Phil Trans: Math, Phys Eng Sci 363:1975
[72] Fabritiis GD, Serrano M, Delgado-Buscalioni R, Coveney PV (2007) Phys Rev E 75:026307
[73] Giupponi G, Fabritiis GD, Coveney PV (2007) J Chem Phys 126:154903
[74] Delgado-Buscalioni R, Fabritiis GD (2007) Phys Rev E 76:036709
[75] Frisch U, Hasslacher B, Pomeau Y (1986) Phys Rev Lett 56:1505
[76] Frisch U, d'Humières D, Hasslacher B, Lallemand P, Pomeau Y, Rivet JP (1987) Complex Systems 1:649
[77] Succi S (2001) The Lattice Boltzmann Equation for Fluid Dynamics and Beyond. Oxford University Press, Oxford
[78] McNamara GR, Zanetti G (1988) Phys Rev Lett 61:2332
[79] Higuera F, Succi S, Benzi R (1989) Europhys Lett 9:345
[80] Benzi R, Succi S, Vergassola M (1992) Phys Rep 222:145
[81] Alexander FJ, Chen S, Sterling JD (1993) Phys Rev E 47:R2249
[82] Ihle T, Kroll D (2000) Comp Phys Comm 129:1
[83] Lallemand P, Luo LS (2003) Phys Rev E 68:036706
[84] Guo Z, Zheng C, Shi B, Zhao TS (2007) Phys Rev E 75:036704
[85] Ansumali S, Karlin IV (2005) Phys Rev Lett 95:260605
[86] Prasianakis NI, Karlin IV (2007) Phys Rev E 76:016702
[87] Gunstensen AK, Rothman DH, Zaleski S, Zanetti G (1991) Phys Rev A 43:4320

[88] Shan X, Chen H (1993) Phys Rev E 47:1815

[89] Swift MR, Orlandini E, Osborn WR, Yeomans JM (1996) Phys Rev E 54:5041

[90] Gonnella G, Orlandini E, Yeomans JM (1999) Phys Rev E 59:R4741

[91] Luo LS (2000) Phys Rev E 62:4982

[92] Luo LS, Girimaji SS (2003) Phys Rev E 67:036302

[93] Guo Z, Zhao TS (2005) Phys Rev E 71:026701

[94] Arcidiacono S, Mantzaras J, Ansumali S, Karlin IV, Frouzakis C, Boulouchos KB (2006) Phys Rev E 74:056707

[95] Halliday I, Hollis AP, Care CM (2007) Phys Rev E 76:026708

[96] Li Q, Wagner AJ (2007) Phys Rev E 76:036701

[97] Qian YH, D'Humieres D, Lallemand P (1992) Europhys Lett 17:479

[98] Ladd AJC (1994) J Fluid Mech 271:285

[99] Ladd AJC (1994) J Fluid Mech 271:311

[100] Ladd AJC, Verberg R (2001) J Stat Phys 104:1191

[101] Adhikari R, Stratford K, Cates ME, Wagner AJ (2005) Europhys Lett 3:473

[102] Dünweg B, Schiller UD, Ladd AJC (2007) Phys Rev E 76:036704

[103] Hinch EJ (1991) Perturbation Methods. Cambridge University Press, Cambridge

[104] Nguyen NQ, Ladd AJC (2002) Phys Rev E 66:046708

[105] Chapman S, Cowling TG (1960) The Mathematical Theory of Non-Uniform Gases. Cambridge University Press, Cambridge

[106] McNamara GR, Alder BJ (1992) In: M Mareschal, BL Holian (eds.) Microscopic Simulations of Complex Hydrodynamic Phenomena. Plenum, New York

[107] Wagner AJ (1998) Europhys Lett 44:144

[108] Karlin IV, Ferrante A, Öttinger HC (1999) Europhys Lett 47:182

[109] Boghosian BM, Love PJ, Coveney PV, Karlin IV, Succi S, Yepez J (2003) Phys Rev E 68:025103(R)

[110] D'Humières D, Ginzburg I, Krafczyk M, Lallemand P, Luo LS (2002) Phil Trans Royal Soc London A 360:437

[111] Lallemand P, Luo LS (2000) Phys Rev E 61:6546

[112] D'Humières D (1992) Progress in Astronautics and Aeronautics 159:450

[113] Ginzburg I, d'Humières D (2003) Phys Rev E 68:066614

[114] Chun B, Ladd AJC (2007) Phys Rev E 75:066705

[115] McNamara GR, Alder BJ (1993) Physica A 194:218

[116] Landau DP, Binder K (2000) A Guide to Monte Carlo Simulations in Statistical Physics. Cambridge University Press, Cambridge

[117] Ginzburg I, Adler PM (1994) J Phys II France 4:191

[118] Guo Z, Zheng C, B Shi B (2002) Phys Rev E 65:046308

[119] Ladd AJC, Frenkel D (1989) In: P Manneville, N Boccara, GY Vichniac, R Bidaux (eds.) Cellular Automata and Modeling of Complex Physical Systems. Springer-Verlag, Berlin-Heidelberg, no. 46 in Springer Proceedings in Physics, pp. 242–245

[120] Ladd AJC, Frenkel D (1990) Physics of Fluids A 2:1921

[121] Ahlrichs P, Dünweg B (1998) Int J Mod Phys C 9:1429

[122] Ahlrichs P, Dünweg B (1999) J Chem Phys 111:8225
[123] Fyta MG, Melchionna S, Kaxiras E, Succi S (2006) Multiscale Model Simul 5:1156
[124] Lobaskin V, Dünweg B (2004) New J Phys 6:54
[125] Lobaskin V, Dünweg B, Holm C (2004) J Physics: Cond Matt 16:S4063
[126] Lobaskin V, Dünweg B, Medebach M, Palberg T, Holm C (2007) Phys Rev Lett 98:176105
[127] Chatterji A, Horbach J (2005) J Chem Phys 122:184903
[128] Chatterji A, Horbach J (2007) J Chem Phys 126:064907
[129] Peskin CS (2002) Acta Numerica 11:479
[130] Nash RW, Adhikari R, Cates ME (2008) Phys Rev E 77:026709
[131] Feng ZG, Michaelides E (2003) J Comp Phys 195:602
[132] Shi X, Phan-Thien N (2005) J Comp Phys 206:81
[133] Aidun CK, Lu YN, Ding E (1998) J Fluid Mech 373:287
[134] Lowe CP, Frenkel D, Masters AJ (1995) J Chem Phys 103:1582
[135] Ricci A, Ciccotti G (2003) Mol Phys 101:1927
[136] Bussi G, Parrinello M (2007) Phys Rev E 75:056707
[137] Thalmann F, Farago J (2007) J Chem Phys 127:124109
[138] Fabritiis GD, Serrano M, Español P, Coveney P (2006) Physica A 361:429
[139] Serrano M, Fabritiis GD, Español P, Coveney P (2006) Math Comput Simul 72:190
[140] Usta OB, Ladd AJC, Butler JE (2005) J Chem Phys 122:094902
[141] Ghadder CK (1995) Phys Fluids 7:2563
[142] Ding EJ, Aidun CK (2003) J Stat Phys 112:685
[143] Claeys IL, Brady JF (1989) PhysicoChem Hydrodyn II:261
[144] Ladd AJC (1997) Phys Fluids 9:491
[145] Brady JF, Durlofsky LJ (1988) Phys Fluids 31:717
[146] Buxton GA, Verberg R, Jasnow D, Balazs AC (2005) Phys Rev E 71:056707
[147] Alexeev A, Verberg R, Balazs AC (2006) Soft Matter 2:499
[148] Junk M, Yang Z (2005) J Stat Phys 121:3
[149] Chen HD (1998) Phys Rev E 58:3955
[150] Chen HD, Teixeira C, Molvig K (1998) Int J Mod Phys C 9:1281
[151] Bouzidi M, Firdaouss M, Lallemand P (2001) Phys Fluids 13:3452
[152] Filippova O, Hänel D (1998) J Comput Phys 147:219
[153] Mei RW, Luo LS, Shyy W (1999) J Comput Phys 155:307
[154] Lallemand P, Luo LS (2003) J Comp Phys 184:406
[155] Maxey MR, Patel BK (2001) Int J Multiphase Flow 27:1603
[156] Lomholt S, Stenum B, Maxey MR (2002) Int J Multiphase Flow 28:225
[157] Zakharov VE, Kuznetsov EA (1997) Physics–Uspekhi 40:1087
[158] Chandrasekhar S (1943) Rev Mod Phys 15:1
[159] Dünweg B (2003) In: B Dünweg, DP Landau, AI Milchev (eds.) Computer Simulations of Surfaces and Interfaces, Kluwer, Dordrecht
[160] Fox RF, Uhlenbeck GE (1970) Phys Fluids 18:1893
[161] See, e.g., http://en.wikipedia.org
[162] van Gunsteren W, Berendsen HJC (1988) Molec Simul 1:173

[163] McLachlan RI, Quispel GRW (2002) Acta Numer 11:341
[164] Forbert HA, Chin SA (2000) Phys Rev E 63:016703
[165] Hasimoto H (1959) J Fluid Mech 5:317
[166] Ladd AJC (2000) In: H van Beijeren, J Karkheck (eds.) Dynamics: Models and Kinetic Methods for Non-equilibrium Many Body Systems. Kluwer Academic Publishers, Dordrecht, pp. 17–30
[167] Beenakker CWJ (1986) J Chem Phys 85:1581
[168] Ladd AJC (1988) J Chem Phys 88:5051
[169] Weitz DA, Pine DJ, Pusey PN, Tough RJA (1989) Phys Rev Lett 63:1747
[170] Ernst MH, Hauge EH, van Leeuwen JMJ (1970) Phys Rev Lett 25:1254
[171] Dorfman JR, Cohen EGD (1975) Phys Rev A 12:292
[172] Hauge EH, Martin-Löf A (1973) J Stat Phys 7:259
[173] van der Hoef MA, Frenkel D, Ladd AJC (1991) Phys Rev Lett 67:3459
[174] van der Hoef MA, Frenkel D (1991) Phys Rev Lett 66:1591
[175] Ladd AJC (1993) Phys Rev Lett 70:1339
[176] Zhu JX, Durian DJ, Müller J, Weitz DA, Pine DJ (1992) Phys Rev Lett 68:2559
[177] Kao MH, Yodh AG, Pine DJ (1993) Phys Rev Lett 70:242
[178] Zimm BH (1956) J Chem Phys 24:269
[179] Rouse PE (1953) J Chem Phys 21:1272
[180] Pierleoni C, Ryckaert JP (1992) J Chem Phys 96:8539
[181] Smith W, Rapaport DC (1992) Mol Sim 9:25
[182] Dünweg B, Kremer K (1993) J Chem Phys 99:6983
[183] Schlijper AG, Hoogerbrugge PJ, Manke CW (1995) J Rheol 39:567
[184] Spenley NA (2000) Europhys Lett 49:534
[185] Malevanets A, Yeomans JM (2000) Europhys Lett 52:231
[186] Mussawisade K, Ripoll M, Winkler RG, Gompper G (2005) J Chem Phys 123:144905
[187] Ladd AJC, Frenkel D (1992) Macromolecules 25:3435
[188] Dünweg B, Reith D, Steinhauser M, Kremer K (2002) J Chem Phys 117:914
[189] de Gennes PG (1976) Macromolecules 9:594
[190] Richter D, Binder K, Ewen B, Stühn B (1984) J Phys Chem 88:6618
[191] Fang L, Hu H, Larson RG (2005) J Rheol 49:127
[192] Jendrejack RM, Schwartz DC, de Pablo JJ, Graham MD (2004) J Chem Phys 120:2513
[193] Ma H, Graham M (2005) Phys Fluids 17:083103
[194] Usta OB, Butler JE, Ladd AJC (2006) Phys Fluids 18:031703
[195] Usta OB, Butler JE, Ladd AJC (2007) Phys Rev Lett 98:090831
[196] Zheng J, Yeung ES (2002) Anal Chem 74:4536
[197] Zheng J, Yeung ES (2003) Anal Chem 75:3675
[198] Long D, Ajdari A (2001) Euro Phys J E 4:29
[199] Butler JE, Usta OB, Kekre R, Ladd AJC (2007) Phys Fluids 19:113101
[200] Caflisch RE, Luke JHC (1985) Phys Fluids 28:759
[201] Hinch EJ (1988) In: E Guyon, Y Pomeau, JP Nadal (eds.) Disorder and Mixing. Kluwer Academic, Dordrecht, pp. 153–161

[202] Nicolai H, Guazzelli E (1995) Phys Fluids 7:3
[203] Segré PN, Herbolzheimer E, Chaikin PM (1997) Phys Rev Lett 79:2574
[204] Koch DL, Shaqfeh ESG (1991) J Fluid Mech 224:275
[205] Ladd AJC (1996) Phys Rev Lett 76:1392
[206] Tong P, Ackerson BJ (1998) Phys Rev E 58:R6931
[207] Levine A, Ramaswamy S, Frey E, Bruinsma R (1998) Phys Rev Lett 81:5944
[208] Brenner MP (1999) Phys Fluids 11:754
[209] Luke JHC (2000) Phys Fluids 12:1619
[210] Mucha PJ, Brenner MP (2003) Phys of Fluids 15:1305
[211] Ladd AJC (2002) Phys Rev Lett 88:048301
[212] Guazzelli E (2001) Phys Fluids 13:1537
[213] Saffman PG (1965) J Fluid Mech 22:385
[214] Ho BP, Leal LG (1974) J Fluid Mech 65:365
[215] Segré G, Silberberg A (1962) J Fluid Mech 14:136
[216] Schonberg JA, Hinch EJ (1989) J Fluid Mech 203:517
[217] Asmolov ES (1999) J Fluid Mech 381:63
[218] Matas J, Glezer V, Guazzelli E, Morris J (2004) Phys Fluids 16:4192
[219] Matas JP, Morris JF, Guazzelli E (2004) J Fluid Mech 515:171
[220] Chun B, Ladd AJC (2006) Phys Fluids 18:031704
[221] Frank M, Anderson D, Weeks ER, Morris JF (2003) J Fluid Mech 493:363